The turning of kites
A quantification of known theories

M.R. van Reijen

TUDelft

The turning of kites

A quantification of known theories

by

M.R. van Reijen

to obtain the degree of Master of Science
at the Delft University of Technology,
to be defended publicly on Tuesday February 14, 2018 at 11:00 AM.

This thesis is confidential and cannot be made public until December 31, 2018.

An electronic version of this thesis is available at `http://repository.tudelft.nl/`.

TUDelft

Preface

It was probably during one of my first year classes that the concept of producing wind energy at a high altitude was introduced to me. This interested me very much since my passion for sustainable energy has been a huge part of my academic endeavors since starting high school. The now deceased Wubbo Ockels showed his idea for the "Ladder mill", an absolutely outrageous idea to put hundreds of kites on a line into the sky that produce immense amounts of energy.

Five years later I learned that the concept had changed somewhat and that now cross wind flight has become the main focus. The elegance of replacing brute heavy structures like the tower with intelligence and lightweight materials lured me into a new field of research. I was very fortunate that Kitepower was looking for people to investigate problems that they as a company are currently interested in.

After having spent 10 months in the USA deriving equations and proving 100 year old mathematics for my internship it was time for me to get practical. This led me to choose a research topic that meant producing a test setup and going into the field to actually fly and test a big kite up to 17 times. Off course I never exptected it to take this many tries but experimentation turned out to be harder than I imagined.

During my time at Kitepower I have had great help from the team and would especially like to thank Pietro for accompanying me on the endless quest to have a single succesfull experiment. The trips to the beach were interesting every single time and since most failed horribly it was nice to have someone around to say it was all going to be allright. Also Johannes Oehler helped me a lot with long conversations and discussions about what the measurements were actually saying.

Off course I would like to thank Joep breuer and Johannes Peschel to let me be part of Kitepower and Roland Schmehl for guiding me during the thesis.

M.R. van Reijen
Delft, January 2018

Contents

Nomenclature

(ξ, η, ζ) Location where the induced velocity is calculated in three dimensional space [m]

α Angle of attack [rad]

β Elevation angle [rad]

β_s The sideslip angle [rad]

$\beta_{\dot{\gamma}}$ The correction angle for rotation velocity of the windvane [rad]

χ Heading angle [rad]

$\ddot{\gamma}$ the rotational acceleration around the yawing axis [rad$\cdot s^{-2}$]

δ The steering input [arb]

δ_0 A constant steering command used for tests by Skysails [arb]

δ_g Geometric input for steering [m]

δ_u Control input for steering [m]

$\dot{\gamma}$ The yaw rate [rad$\cdot s^{-1}$]

Γ Vorticity [$m^2 \cdot s^{-1}$]

γ Yaw angle [rad]

Γ_0 Contant representing total amount of voriticity produced by a lifting object [-]

ν Warping angle of the kite [rad]

ϕ Azimuth angle [rad]

ψ Roll angle [rad]

ρ The density [$kg \cdot m^{-3}$]

$\vec{F}_{\text{centripetal}}$ Centripetal force [N]

$\vec{V}_{\text{localearthfixed}}$ A vector defined in the local earth fixed reference frame

$\vec{v}_k$ The velocity vector of a wing in an earth fixed reference frame [$m \cdot s^{-1}$]

$\vec{v}_{\dot{\gamma}}$ the induced velocity at the location of the sideslip windvane [$m \cdot s^{-1}$]

A Surface area [m^2]

b The span of a kite [m]

b_1, b_2 The lengths between the points of suspension [m]

C_D The drag coefficient [-]

C_L The lift coefficient [-]

C_P non dimensional ratio between power present in the wind stream and power available in the wind-stream for extraction [-]

D Drag force [N]

D_i Drag force of the ith part of the discretized wing [N]

E_{eq} The equivalent aerodynamic efficiency [-]

F_L Lift force [N]

F_T Tether force [N]

G The constant that relates the steering input and velocity to the yaw rate [-]

g The gravitational acceleration [$m \cdot s^{-2}$]

I the moment of inertia around the considered axis [Nm]

I_γ the mass moment of inertia around the yawing axis [$kg \cdot m^2$]

$K_{\dot{\gamma}}$ Current gain between turn rate and deflection [arb $\cdot m \cdot s^{-1}$]

L Lift force [N]

l_i Length of a discretized vortex filament [m]

M the applied moment around the yawing axis [Nm]

m The mass [kg]

M_{diffdrag} The moment caused by a difference in drag forces [Nm]

M_{top} The moment caused by the top of the kite [Nm]

M_{warp} Moment caused by warping of the kite [Nm]

P The power present in the windstream [W]

p_{static} Static pressure [Pa]

p_{total} The total pressure [Pa]

P_R Is the power available in the windstream for extraction [W]

r The distance between two points being considered [m]

R_{specific} Specific gas constant [$J \cdot K^{-1} \cdot \text{mol}^{-1}$]

S The lenght of two lines in a bifilar pendulum experiment [m]

S_i Side force on the one of the sides of the kite [N]

T Temperature in degrees Kelvin [^{o}]

T The period of an oscillation [s]

T_{bF} The transformation matrix from the local earth reference frame to the body fixed reference frame

$T_{\text{bF}''}$ The rotation matrix around the roll axis

$T_{\text{F}''\text{F}'}$ The rotation matrix around the pitch axis

$T_{\text{F}'\text{F}}$ The rotation matrix around the yaw axis

V The volume of a given object [m^3]

V_{b} A vector defined in the body reference frame

v_{local} The local apparent wind velocity [$m \cdot s^{-1}$]

v_a The apparent wind velocity [$m \cdot s^{-1}$]

v_i Induced velocity $[m \cdot s^{-1}]$

v_w The wind velocity $[m \cdot s^{-1}]$

w The downwash $[m \cdot s^{-1}]$

z Height of the current location on the streamline relative to a given reference plane $[m]$

VDC   Volts of direct current

List of Figures

List of Tables

Summary

Using kites as a means of producing energy is part of a growing field of research on creating new inexpensive ways to obtain renewable electricity. Airborne Wind Energy [AWE] uses lightweight flying structures on a tether to access higher more constant winds without the need for heavy towers. Kites in this sense are an easy pick as they are flexible, lightweight, and inexpensive to produce. One negative aspect however is the complex interaction that a flexible structure has with a flow environment. This study will experimentally determine some parts of the behaviour of a kite during different operations.

Kitepower is a company established in 2016 on a path to create a system that uses a single kite with a generator on the ground that is capable of producing 100 kW of power. In order for them to attain this goal knowledge on the deformations of their kitesystem can be very valuable and allow them to improve the performance of a system greatly. To the knowledge of the author a thorough quantitative experimental investigation into the deformations of a kite during actual flight has not yet been performed. This work attempts to quantify to a large extent the most important deformations during straight and turning flight while measuring the performance.

In order to do so a test setup is put together to measure several different parameters on the flying kite itself and on the ground. The tests are performed at the beach where a relatively clean airflow is available due to the absence of obstacles on the water. A sand bag is used to fixate a point on the ground and three force measurement devices are applied to the different lines connecting the kite to the ground. The pilot steers the kite using a standard kite surf steering bar. At the kite itself there are three positions where the local attitude, rotational velocities, and accelerations are measured and synchronized by means of a GPS connection. Then at the center of the kite the apparent wind velocity is measured by means of a pitot tube and the flow directions are measured using two wind vanes for the angle of attack and the sideslip angle.

The different points of operation that are tested are four static power setting positions to find the aerodynamic performance coefficient as a result of the angles of attack. Then several turns are performed at constant steering inputs to determine the turning rates and the corresponding deformations at the sides that are assumed responsible for the steering. Since it is found that the power setting changes the steering speeds the turns are performed at varying power settings. All of this should lead to an analysis where it is confirmed that the steering can be attributed to two distinct steering mechanisms.

One of the mechanisms is the lift force driven steering where an offset in the lift forces on both sides creates a moment that rotates the kite and the following change in angle of attack on both sides leads to a centripetal force sending the kite to move in the appropriate direction. The other manner in which a kite can be steered is an initial change in angle of attack on both sides, where one side will experience an increase drag and lift and the other side sees a decrease in both. This will result in a rotation due to the drag difference between the two sides and a centripetal force due to a net increase of lift force in the direction of the turn.

To compare the performance of kites the non-dimensional Aerodynamic Coefficient value C_R is defined which is a means to compare the amount of force a kite is able to produce irrespectable to its dimensions. In earlier experiments Python[30] determined this value in a somewhat controlled environment using a towing test and a test setup designed by Hummel[20] at the Technische Universität Berlin [TUB]. The values given by the current setup are comparable to the values found by Python. During his test however the angles of attack were not measured. The angle of attack at the center changes from lowest to highest power setting from 5 to 15° respectively. At the sides however the angles change from 10 to 35° which suggests that the sides of the kite are relatively more activated than the center during power up. Also from the distribution of forces between the front and back lines it seems that more lift force is produced at the sides than at the middle for higher power settings. The deformations show that the sides change angle of attack more than the middle but also the sides are seen to roll upwards which increases the projected area of the kite. This area is defined as the surface area that is seen when looked at from straight below. And it is this area that is able to produce

1

forces that contribute to power production.

The windvane sensor was found to give incorrect data due to induced velocities from the vorticity of the kite. The use of the attitude measurement however provided the angle since a straight horizontal flow is assumed. It is found however that using the force data a simple vorticity model provides the correction needed to find very similar angles of attack as were given by the attitude measurement device. This allows a test setup where the forces are measured to use this windvane in a situation where horizontal flow is not a viable assumption.

For the steering the test setup shows a good comparison with literature concerning a known turn rate law. This law is a means to determine the angular velocity around the yaw axis of the kite as a function of the steering input for a given apparent wind velocity. The kite starts off with a clear acceleration into a turn and then finds a more steady but still increasing yaw rate. The increase in yaw rate after the first acceleration is explained by the different flight paths as it goes from a steady hanging still in the air situation into a cross-wind flight path which increases the velocity of the kite. This increase in velocity in turn increases a difference in forces that exists between the different deformed parts of the kite which then deform even more.

The measured deformations show a clear warping of the kite. But at the tips the local angles of attack deform in an unexpected direction that goes against the moment force needed to turn the kite in the right direction. This leads to the conclusion that the means of turning for the kite is warping but that this warping does not add a significant lift force offset which in turn creates a moment force. The tips which are off set the most show a negative local angle of attack. Thus the part with the biggest arm shows a force that goes opposite to the rotation that the kite turns into. The warping however does increase the lift and drag forces at the right side and decreases them at the left side which create a centripetal force and a moment force. The added lift force on the right and decreased lift force on the left create a net force to the right which the kite accelerates towards. Also the added drag forces are pointed in the correct direction to support the turn in the right direction.

These means of rotating a flexible kite have been shown to be the cause of steering before by computational models created by Breukels[6]. This thesis now shows experimentally that the mechanism described by Breukels are indeed responsible for the turning but in a slightly different manner than his model shows. This difference is accounted for by a different type of kite described by the model than is used during this research.

The test setup shows great potential as a means of measuring in flight deformative behaviour of power producing kites. This will allow a design procedure to verify wether implemented designs deliver the expected behaviour and show where focus can be put to optimize for different types of kites. The quantification of said behaviour can now also be put into computational models that are then validated by experimental results. Both these implementations could contribute greatly to an increase in productivity of an AWE system.

1

Introduction

For several hundred years people have used wind energy to replace physical labour and improve the productivity of harvesting food, transport people and goods, or transport water. However with the exponential use of electricity in the everyday lives of billions of people around the world the use of wind energy for electricity generation has seen a steep rise in the last decades. Now with an exponentially increasing demand for clean energy new inexpensive ways to harness the power of the wind are being investigated. In that respect the airborne wind energy community has been showing great potential to provide such new ways leading to a leap foward in producing clean energy for the world.

Wind energy

Generally speaking, wind is simply air in movement [5]. The means of producing wind energy is by decreasing the velocity of the moving air and transforming the kinetic energy into electrical energy. Since people want to get as much energy as possible the amount of kinetic energy that is extracted needs to be as high as possible. To find the kinetic energy flux in the wind Archer [5] gives:

$$P = \frac{1}{2} \rho A v_w^3,$$ (1.1)

where P is the power present in the windstream, ρ is the density of the air, A is the cross section of a stream tube where the wind flows through, and v_w is the wind velocity. However not all energy is available for power extraction. Momentum theory provides the coefficient of performance. This is a ratio that shows which part of the energy is available for extraction by a circular propellor turbine in free air and is determined to have a maximum value of:

$$C_p = \frac{P_R}{P} = \frac{P_R}{\frac{1}{2} \rho A v_w^3} = \frac{16}{27} = 0.593,$$ (1.2)

where P_R is the power available in the windstream for extraction, C_P is the non dimensional ratio between power present in the wind stream and power available in the windstream for extraction. This limit to extracting the energy is also known as the Betz limit.

The amount of wind energy that is available in the earth atmosphere depends on five different effects [5]. These are:

1 Pressure Gradient. The air is blown from high pressures to low pressures.

2 Coriolis effect. The earth rotates thus moving air parcels experience an apparent acceleration to the right in the northern hemisphere and to the left in the southern hemisphere.

3 Gravity. Air is pulled towards earth.

4 Turbulence Flux Divergence. Eddies interact with each other and exchange heat and momentum affecting the momentum equation.

5 Viscous diffusion. Since the ground does not move the airflow loses energy blowing past the surface and any obstacle (like trees or buildings). This creates the atmospheric boundary layer.

Low vs high winds

Since the amount of power available for extraction in the wind is dependent on the density and the velocity it makes sense to look for places where the air moves with high velocity and has a high density since this means a high wind power density according to equation 1.1. Due to the five effects named in section 1.1 an obvious difference in the amount of energy is likely to occur at different altitudes. On the one hand the velocity will increase with altitude due to the reducing influence of friction with the surface of the earth. However the density will decrease since gravity increases the density the closer you get to the surface. Figure 1.1 shows the amount of energy that is available for different heights in the standard atmosphere. The two horizontal lines show where conventional (low) and airborne (high) wind energy would operate. Clearly the higher operating system could enjoy a more abundant amount of energy per square meter. Thus for any given system that means that the amount of energy it can generate will be more the higher it operates (when other parameters stay the same).
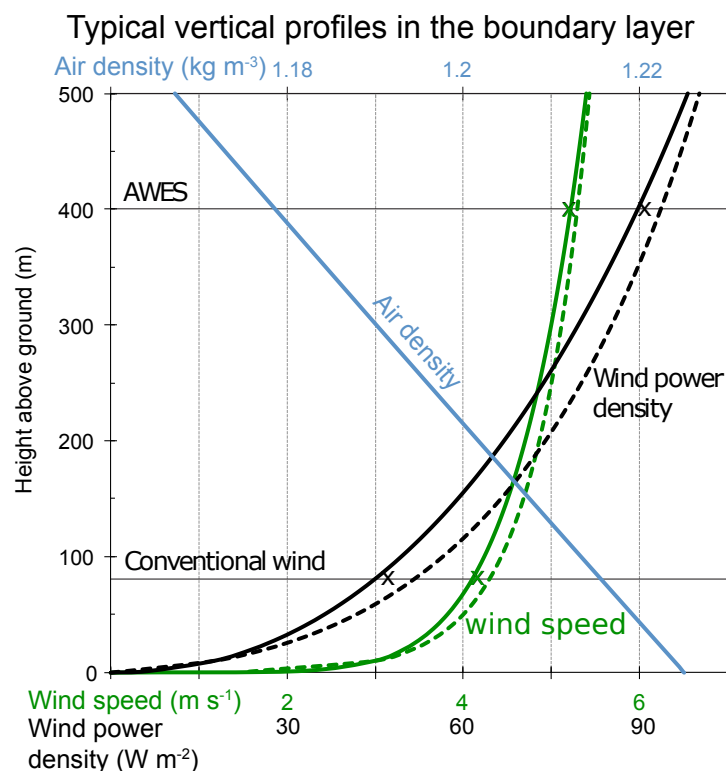
Figure 1.1: Vertical profiles of the air density ($kg\,m^{-3}$) in the standard atmosphere, wind speed (ms^{-1}) derived using the power law (green solid) and the log law (green dashed), and the wind power density ($W\,m^{-2}$) *source:* [5].

Airborne wind energy

"Tethered wings that fly fast in a crosswind direction have the ability to highly concentrate the abundant wind power resources in medium and high altitudes, and promise to make this resource available to human needs with low material investment" [32, p.3]. Airborne wind energy is generated using airborne devices. These devices could be flying in air with or without a connection to the ground surface, however all systems with significant power output are mechanically connected to the ground in order to use the relative velocity difference between the wind and the ground surface [32]. Loyd provided the theory needed for the assessment of potential energy harvesting capabilities of airborne wind energy systems in his paper "Crosswind Kite Power" [24] (further explained in section 1.5). Between 1980 and the early 2000s no significant developments have happened in the field of airborne wind energy. However the technological improvements in the computer industry allow for very inexpensive and high performing microprocessors that provide a means of controlling

these often highly dynamic devices. That together with the so called "square-cube-law" [29] has sparked a new interest in this form of wind energy generation from the early 2000s up till the current day.

There are several distinctions to make when looking at the different types of airborne wind energy systems that are under current investigation. Two different aspects are often key when discussing the different concepts. First there is the location of the generators which can be either on the ground which is called *ground-gen*, or attached to the flying device thus also airborne and called *sky-gen*[8]. Then there is the difference between static systems (systems that stay in place as a whole) and systems that move through the air while generating power.

Examples of airborne power generation devices are given in figure 1.2. All of these systems have generators on the airborne device and send the electrical energy down by means of a tether-conducting wire combination. The right one is a static system that stays in place and the left one flies maneuvers to generate power. One of the downsides of these type of systems is the fact that the generator mass is also needed up in the air which usually decreases performance of the flying object.
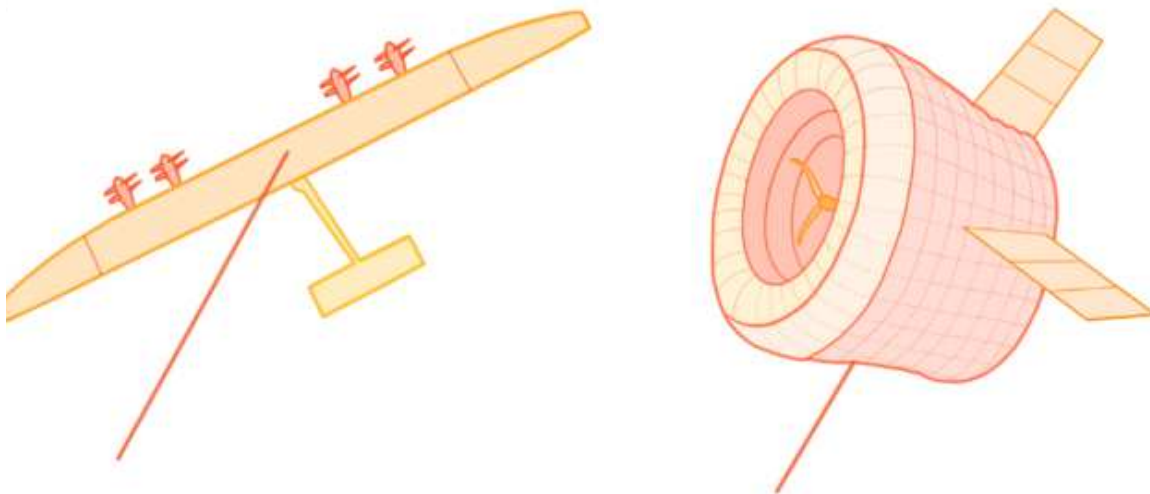
Figure 1.2: Examples of *Sky-gen* systems. Left: *Makani*, a rigid wing flying crosswind in circles, right: *Altaeros energy*: Toroidal lifting aerostat with a wind turbine in the center *adapted from:* [8]

Examples of ground generated power systems are shown in figure 1.3. In these cases the generator is on the ground and can have different implementations. The first possibility is to use a pumping motion where during a reel-out phase the device flies crosswind generating large forces which are used to generate power. The plane is turned in the wind at some point which generates low forces and allows for the device to be pulled down easily. Another possibility is to use a large wheel of some sort with several wings that create a centripetal force that forces a rotational motion. Other ways are of course possible but the main idea is that a wing high up in the sky transfers motion to a generator located on the ground.

A total overview of the current industry is given in figure 1.4.

Kite power

The company Kite power utilizes a ground-gen system with a flexible kite in a pumping motion flying crosswind figures of eight as shown in figure 1.5. While the kite flies figures of eight it transfers large forces to the generator on the ground. When a certain threshold has been reached the steering module just beneath the kite steers the kite into the wind and depowers by lowering the angle of attack. Then the generator pulls the kite down with little effort. Although the pulling down of the kite costs energy the sum of the pumping motion is a positive energy output.
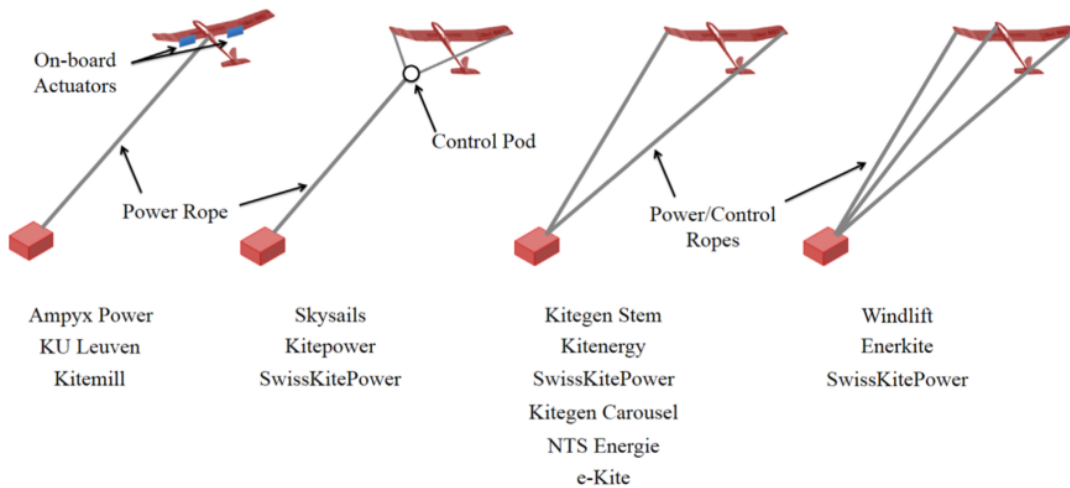
Figure 1.3: From left to right: Steering through on-board actuators with one line to the ground, steering with the help of a control pod with one line to the ground, steering with two lines which also transfer the forces, steering with two lines to the ground and an additional force line to the ground. Here only rigid flying structures are given but flexible structures can also be used. *source:* [8]
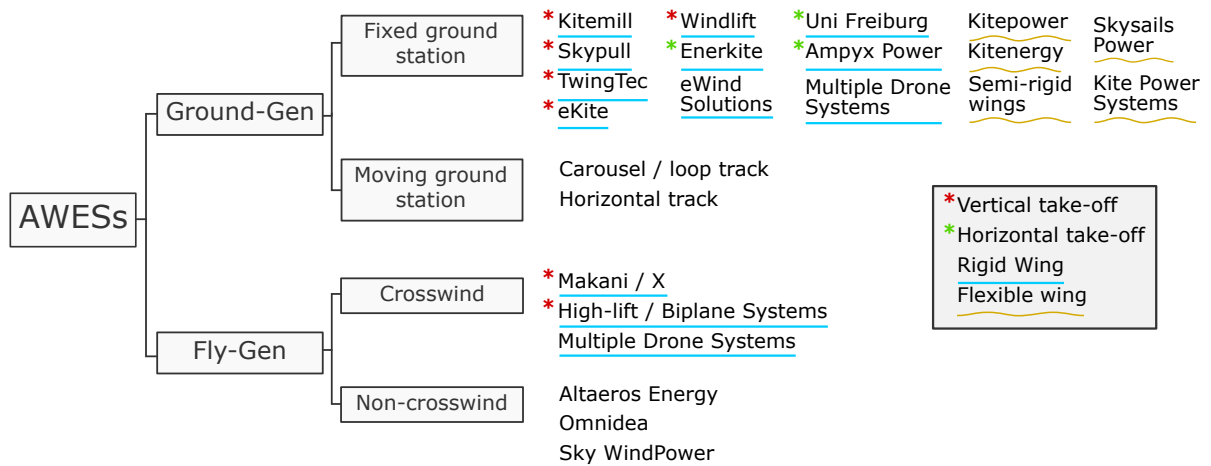
Figure 1.4: All different companies currently working on airborne wind energy and their respective implementation type. *source:* [7]
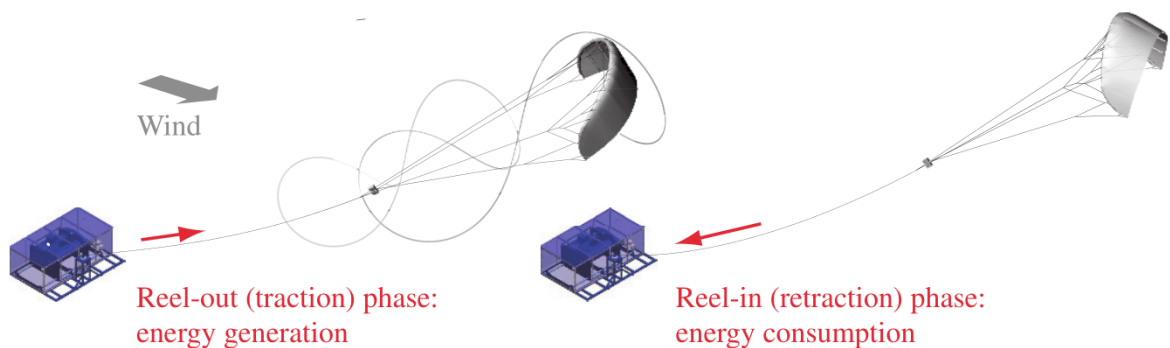
Figure 1.5: The working principle of the Kite power system. A kite drives a generator while flying figures of eight which produce large forces, when a certain tether length is pulled out the kite turns into the wind and depowers allowing the generator to pull the kite back down with low energy cost. *source:* [32]

The key here is the difference between the manners of flying during reel-out and reel-in. During reel-out the forces need to be as big as possible thus the kite flies crosswind. Why this manner of flying generates high forces will be explained in section 1.5. Subsequently during the reel-in the forces need to be as small as possible. For both situations it is important that the airborne system is controllable. For this a kite control unit or KCU is utilized. The KCU is able to steer by means of pulling on steering lines which makes the kite move in a desired direction.

Cross-wind flying

As soon as a kite is flying fast loops in a crosswind direction the tension in the lines increases significantly [10, p.4]. The lift force created by a wing that flies in crosswind motion equals:

$$F_L = \frac{1}{2}\rho A C_L v_a^2, \tag{1.3}$$

where F_L is the lift force in newtons, ρ is the density of the air, A is the airfoil area, C_L is the lift coefficient, and v_a is the apparent wind velocity. The apparent wind velocity in this case is the velocity that is felt by the kite moving through the air. The movement of the kite in a direction perpendicular to that of the wind direction increases the apparent wind velocity. In practice the relation in equation 1.3 shows that for an airfoil that flies crosswind and experiences a velocity v_a ten times greater than the wind velocity v_w, the force in the tether will be a hundred times more powerful than when such an airfoil hangs still in the wind.

As mentioned before, Loyd was arguably the first person to compute the power generation potential of crosswind flying tethered wings[10]. He investigated and patented the idea of an airplane or kite flying circular trajectories in the sky while being connected to the ground by means of a tether. Then there are two ways of producing power either by means of a drag mode or a lift mode. The drag mode uses the high apparent wind velocity v_a to drive small turbines on the flying plane and the lift mode transfers force to the ground to drive a generator there. This is the same distinction as was made earlier, the drag mode corresponds to sky-gen and the lift mode to ground-gen. When the sky-gen principle is compared to that of a conventional wind turbine we see that effectively the entire plane replaces only the outer regions of the wind turbine as shown in figure 1.6. This is a great benefit to the efficiency of the airborne system. *The motivation for this is the fact that the outer 30% of the blades of a conventional wind turbine provide more than half of the total power* [10, p.5]. Now the power that can be generated by the airborne system in this case was estimated by Loyd[24] to be:

$$P = \frac{2}{27}\rho A v_w^3 C_L \left(\frac{C_L}{C_D}\right)^2, \tag{1.4}$$

with P the power available, ρ the density of air, A the area of the wing, v_w the wind velocity, C_L the lift coefficient, and C_D the drag coefficient. Thus we see that the available power is driven by one term that might be greatly influenced by precise steering, the ratio between the lift and drag coefficient $\frac{C_L^3}{C_D^2}$. When this value is maximized for any given system the performance during a power extraction phase is maximized.

A lot of research has gone into optimizing the paths the wings should follow to achieve the maximum amount of power output. Gros [17] for example provides a relaxation strategy of the optimization problem which can deal with the highly non-linear behavior of the flying kite system. This however means that a precise knowledge of how the kite steers is required before such an optimized path can be utilized.

Theory

One of the main ways of computing the controls flexible kites at the moment need to steer is using the so called turn rate law. This law is a relatively simple relation between a steering input and the rate at which the kite yaws.
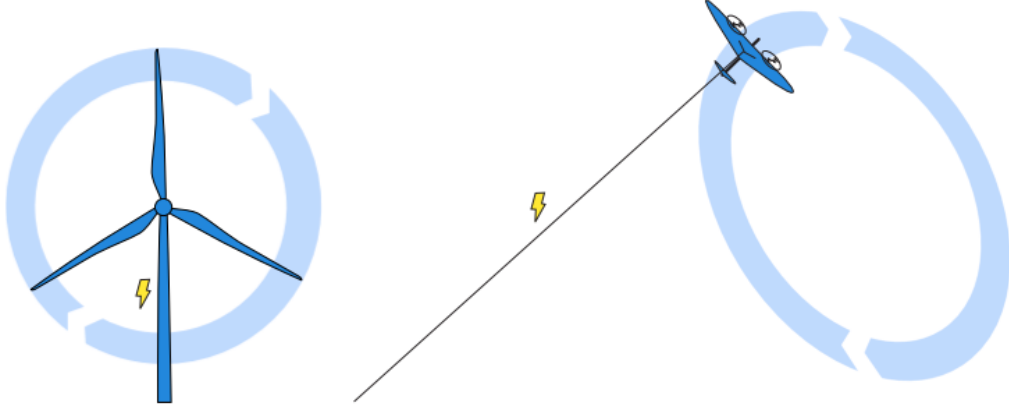
Figure 1.6: A conventional wind turbine compared to a sky-gen crosswind system. The entire airborne system effectively replaces only the outer regions of the turbine which generate the most power. *source:* [10]

Turn rate law

There are several papers that discuss the origin and proof to show what the turn rate law is, two of those are are discussed here. One of the first thorough investigations to the steering of soft kites has been done by Fagiano et al.[13]. The final conclusion of his research was the turn rate law, a relation between several parameters and a turn (yaw) rate of the kite. In order to come to his relation he used two assumptions:

1. The difference between the velocity angle $\gamma(t)$ and the heading angle $\chi(t)$ is negligible.

2. The angle roll $\psi(t)$ is sufficiently small to linearize its trigonometric functions.

The first assumption means that the apparent wind projected onto the tangent plane to the wind window at the wing's location is equal to the wing's velocity $\vec{v}_k(t)$. In addition, all forces in the direction of vector $\vec{v}_k(t)$ are negligible compared to lift and drag.

The second assumption says that the non dimensional roll angle $\psi(t)$ is very small, it can be computed by:

$$\psi(t) = \arcsin\left(\frac{\delta(t)}{b}\right), \tag{1.5}$$

where $\delta(t)$ is the difference in length between the right and left steering bridles, and b is the wing span. Here however a model has been used where there are two steering lines that go all the way to the surface. This leads to the use of an added term for $\delta(t)$ to be:

$$\delta(t) = \delta_u(t) + \delta_g(t), \tag{1.6}$$

with the geometric input $\delta_g(t)$:

$$- d\sin(\phi(t))\cos(\beta(t)). \tag{1.7}$$

But the fact that in the systems that are investigated the steering is done from a KCU means that this term can be neglected since the geometric term as used in [13] is not present.

For the final relation however it changes nothing and following the steps encountered in the paper leads to the turn rate law as:

$$\dot{\gamma} = \frac{C_L \rho A}{2mb}\left(1 + \frac{1}{E_{eq}^2}\right)^2 |\vec{v}_a|\delta + \frac{g\cos(\beta)\sin(\gamma)}{|\vec{V}_a|} + \sin(\beta)\dot{\phi}, \tag{1.8}$$

with $\dot{\gamma}$ the turn rate, C_L the lift coefficient of the kite, ρ the density of the air, A the area of the kite in square meters, m the mass in kg, b the span of the kite, E_{eq} the equivalent aerodynamic efficiency, $\vec{v}_a$ is the apparent wind velocity at the kite, δ is the steering input as described above, g is the gravitational acceleration. The
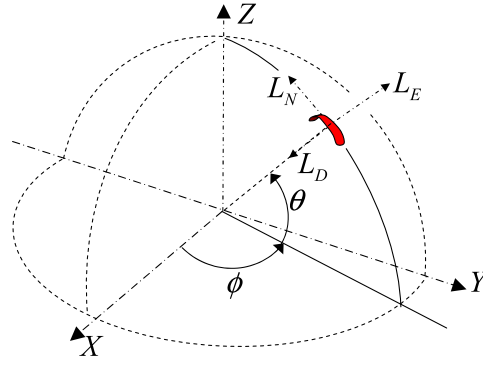
Figure 1.7: The angles used in Fagiano et al.'s derivation of the turn rate law. *source:* [13]

angles β and ϕ are the elevation and azimuth angle which are shown in figure 1.7.

Erhard and Strauch [11] have another, somewhat simpler intake on the turn rate law. Skysails was a company that used kites to assist in vessel propulsion. They launched a kite attached to the vessel and fly figures of eight on a tether of constant length. The Skysails team has included experiments for their sea fairing kites by in field testing.

For modeling purposes they have used several assumptions:

1. Gravitational terms are neglected

2. Rope dynamic neglected

3. Aerodynamics assumed in equilibrium, and steering deflections can be described by a single parameter g

4. Wind field constant and homogeneous

5. Vessel dynamics neglected

The first assumption leads to many simplifications. When the gravity is neglected the aerodynamic forces and forces in the tether are equal and in opposite directions. The second assumption means they assume the tether to be a rigid straight massless tether which is only a means of transporting the forces to the vessel. The third assumption means that the kite is always in a steady state, this allows the behavior to be fully determined by the glide ratio G, or L/D or C_L/C_D. And the fact that the steering is described by a single parameter allows for very simple steering control, if shown that it can be done. The fourth assumption is one that is clearly not one that corresponds to normal wind fields, however it does simplify the model to be able to relate all the dynamics to a single velocity v_0 and in their paper they have found a correlation where this simplification does not lead to severe errors. And the last one is very specific for the Skysails operation. Their purpose is to create as much force forward as possible, therefore an optimal situation would differ from the one where power is generated. However this aspect is neglected so this assumption fits the purpose of this research.

Following the steps taken in [11] another turn rate law is given as:

$$\dot{\gamma} = K_{\dot{\gamma}}\delta + M\frac{\cos{(\beta)}\sin{(\phi)}}{v_a}, \tag{1.9}$$

where $\dot{\gamma}$ is the turn rate, $K_{\dot{\gamma}}$ is the current gain between turn rate and deflection ($K_{\dot{\gamma}} = g v_a$), the angle β is the elevation angle, ϕ is the azimuth angle, and δ is the deflection (difference between left and right bridle lengths in meters). Then M is a collection term for all the gravitational influences present in the tether and kite system. This term was neglected in the initial derivation of dynamic relations but then later added as a corrective term. And finally v_a is the apparent wind velocity.

In the end both theories are very comparable. Fagiano however specified more precisely which exact parameters are responsible for the effectiveness of the steering. While Erhard and Strauch took on a more

application driven approach where emperic relations have a more dominant position and is more usefull for an initial validation of any given test setup.

Kite deformations

Breukels[6] explains what the current ideas are on how exactly it is that a kite makes a turn as seen from the kite reference frame. He created a computational model based on multi-body dynamics. From this model he determined that the cornering of kites is governed by two principles. First of all when a steering line pulls on for example the right side and lets the left side go, the surface area of the right side will increase and the surface area on the left will decrease. Besides this pulling on the kite tip has another effect. Due to the asymmetric force on the kite an asymmetric deformation of the kite structure occurs that increases the angle of attack on the right and decreases the angle on the left. both of these mechanisms will increase the lift and drag forces on the right and decrease the lift and drag forces on the left since we have:

$$L = \frac{1}{2}\rho v_a^2 A C_L(\alpha), \qquad , \text{ and} \tag{1.10a}$$

$$D = \frac{1}{2}\rho v_a^2 A C_D(\alpha), \tag{1.10b}$$

where L is the lift force, ρ is the density, v_a is the apparent wind velocity, A is the surface area, C_L is the lift coefficient, α is the angle of attack, D is the drag force, and C_D is the drag coefficient. When increasing/decreasing the surface areas and angle of attack the lift and drag forces will also increase/decrease alongside them. This means that a lift force offset to the right will make the kite move to the right and a drag force offset will create a moment force turning the kite clockwise (when viewed from below). This leads to the behavior we expect when the right side is pulled down.

Besides this another effect is mentioned, a warping of the kite occurs due to the fact that a pulling force is applied on the right trailing edge moving the right side somewhat forward. This creates an offset in the lift forces which allows for an added yawing moment to exist. Figure 1.8 shows how this would occur:
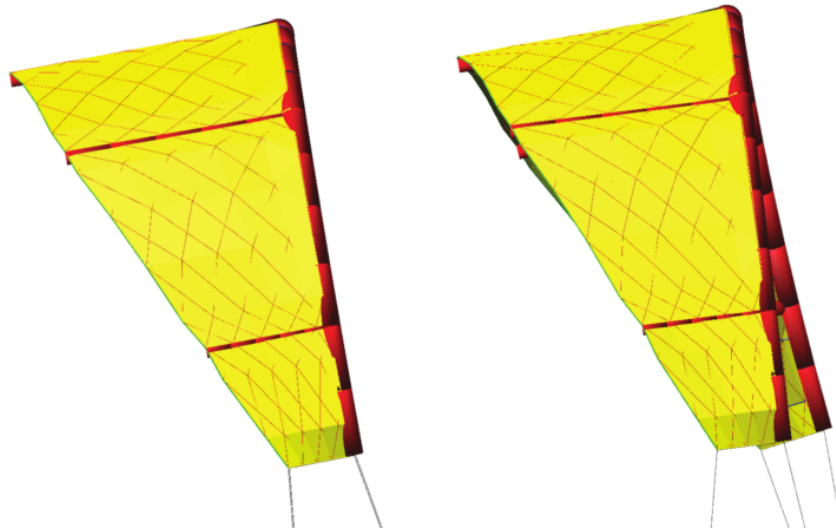

Figure 1.8: Here a kite is shown from the side before and after a steering input to the right has been applied. Right here is defined from the pilots' perspective. The right side is pulled forward and the left side is allowed to move backwards. This creates an offset in lift forces which in turn creates a yawing moment. *source:* [10]

Experiments

The amount of quantitative experiments performed on kite systems is very minimal since there exist difficulties in performing experiments. For aircraft or wind turbines use can be made of non dimensional number to change the flow environment in a distinct manner to find the performance using small models. The flexibility of kites however eliminates this possibility. In real lift tests the flow domain around the kite is not exactly known due to natural disturbances in the wind field which change the density, temperature and apparent flow velocity [30] around the kite. Even the shape of the kite is not known due to the high flexibility which comes with the benefit of the lightweight structure [6]. Despite these difficulties the last few decades have shown multiple strategies to be effective in obtaining quantitative data from kite experiments. An overview of the different relevant experiments is given in table 1.1 showing the main goals and parameters measured per experiment.

Table 1.1: A selection of relevant experiments performed on kites in the past.

Test performed by	moving/static ground station	kite size	main parameters	goals
Erhard [11]	moving seavessel	up to 320 m^2	yaw rate, steering deflection, apparent wind velocity, line angles	Justify main dynamics of their turn rate law
Stevenson [21]	car mounted	3.2-12 m^2	wind speed, line forces, line angles	Define main aerodynamic properties (C_L, C_D)
Dadd [9]	car with trailer	3 m^2	wind speed and direction at car, line forces, line angles	Compare two line tension models with real flight experiments
Hummel [20] and Python [30]	car with trailer	9-14 m^2	wind speed and direction at car, line forces, line angles, steering input, power ratio	Improve assessment of aerodynamic properties and their exactitude
Fagiano [13]	static	6-12 m^2	velocity vector, position	Test the overall control system for tethered wings
Fagiano [14]	static	8-18 m^2	position, traction forces, line length	The effectiveness of the developed optimal and suboptimal approximation control techniques are tested
Fechner [15]	static	20.36 m^2 (projected)	wind speed, line forces, line speeds, power output, line angles at GS	Test and verify control algorithms

The Skysails team has performed in field measurements of their envisioned turn rate law [11]. One of their operational kites was used in different flow fields including disturbed sea trial conditions. The key to the experiments was to perform bang-bang flights. This manner of testing for the turn rate was to apply a constant

steering command of $+\delta_0$ and when a certain angular threshold (ψ_0) was reached an opposite steering command of $-\delta_0$ is commanded. This would bring the kite to move in the opposite direction, subsequently when the angular threshold of ($-\psi_0$) is reached again the positive steering input of δ_0 is applied moving the kite yet again in the opposite direction which creates a loop. The test setup is shown in figure 1.9a. The results are shown in figure 1.9b. The results back up the found relation given in equation 1.9. The parameter G can be found by the shown linear result.

(a) The BBC Skysails with towing kite. The 132-m vessel utilizes kites of sizes up to 320 m^2.*source:* [19]
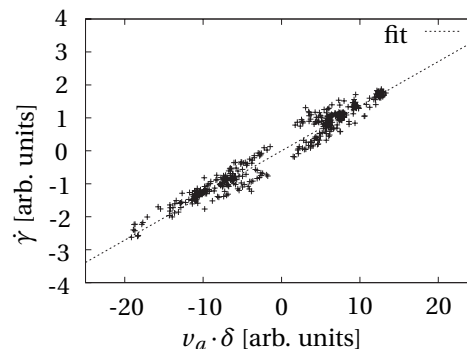
(b) The results of the experiments performed by Skysails show the linear nature of the response to control inputs, it shows the measured data of a bang-bang flight. Yaw rate $\dot{\gamma}$ as a function of the air path speed multiplied by deflection $v_a\delta$. *source:* [11]

Stevenson [21] created a different test setup making use of a car-mounted rig as shown in figure 1.10. *The repeatability of the results from this test rig was found to be $\pm 0.8^o$ on the angle guides and $\pm 15\%$ for the lift coefficient*[21]. For initial testing this showed promise as the measurement of the angles were accurate, only later it was found that for real experimental data this setup was not adequate since the overall data was not accurate enough. Stevenson concluded that it was useful for determining the general performance of a particular design though. This setup is therefore interesting if the accuracy could be improved by utilizing better sensors.

Figure 1.10: Photograph of the test rig mounted on the car. This first crude attempt to measure different aspects of the performance of kites proved to be good for initial testing but not for highly quantitative experiments. *source:* [21]

Fagiano et al.[13] have created a different test setup as shown in figure 1.11. It is a simple ground station without any possibility to reel out and is mainly built to assess the control of a kite. Within this research they have found results concerning the steering behavior of a kite.

The data is shown in figure 1.12 where it is compared to the theoretical linear relationship between the behavior and given steering inputs. This shows that the relation describes the behavior of the kite given a certain steering input well. This however does not provide a clear validation case for high fidelity models since

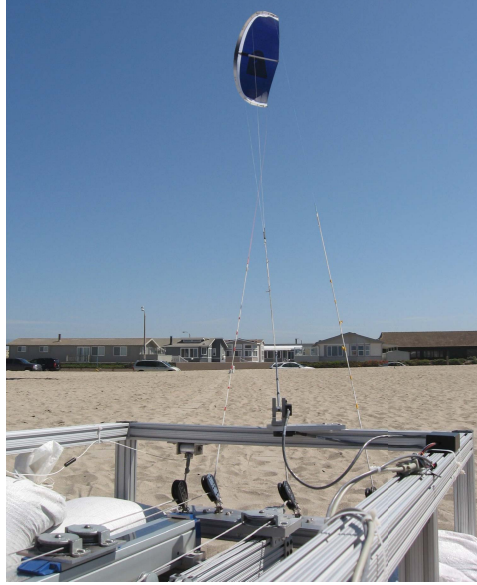the flow field the kite operates in is highly dynamic and unknown.

Figure 1.11: The test setup used by Fagiano et al[13]. The small kite is controlled by two lines that reach the ground station.
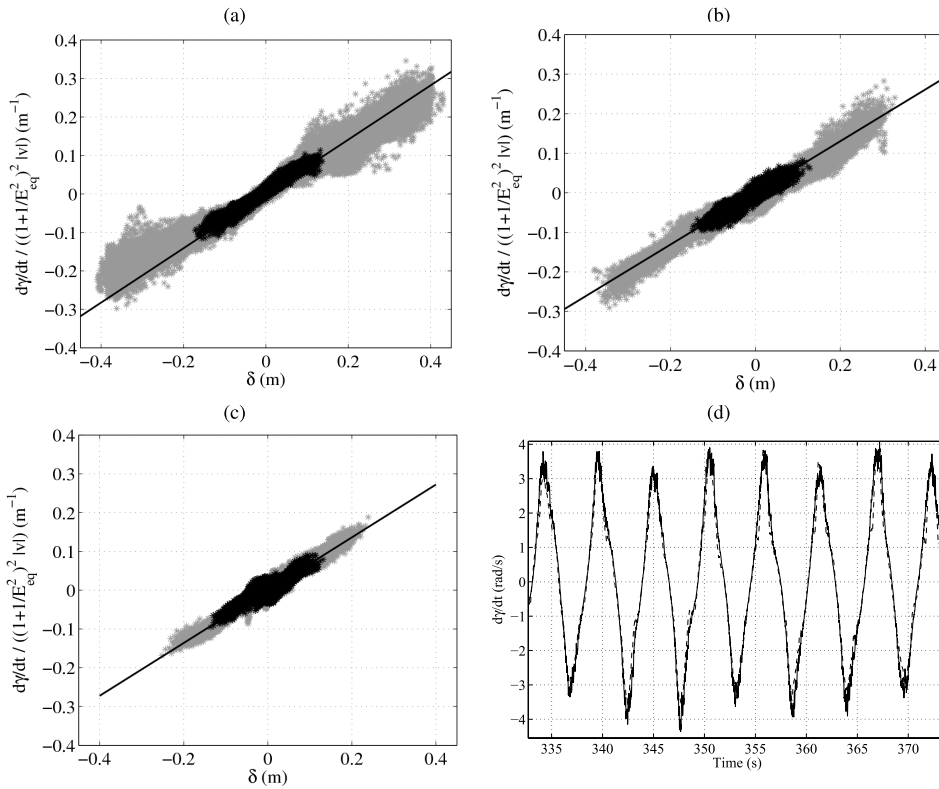

Figure 1.12: The results found by Fagiano et al.[13] Experimental results. (a)–(c) Comparison between the measured values of $\dot{\gamma}(t)/((1+1/E_{eq}^2)^2|\vec{v}_a(t)|)$ as a function of the steering input $\delta(t)$ (gray and black dots) and the theoretical linear relationship given by the gain $\rho C_L A/2md$, as per (16a) (solid line). The gray dots represent experimental data collected in the whole range of β, ϕ spanned by the wing during operation, while the black dots represent values collected when $|\phi| \leq 5^o$, i.e., in crosswind conditions. (a) Airush One 6 kite. (b) Airush One 9 kite. (c) Airush One 12 kite. The lumped parameters for the kites are reported in Table I. (d) Comparison between the value of $\dot{\gamma}$ obtained in experimental tests (solid) and the one estimated using the simplified model and the result of Proposition 1 (dashed line). Wing size: 6 m^2

Oehler [27] constructed a test setup that flew just above the KCU of the Kitepower system during one of their test flights. Figure 1.13 shows where it is placed with respect to the kite itself and which flow angle the wind vane measures. The reason that the system is placed this far from the kite itself is to minimize the effect that induced velocities of the kite have on the measurement setup. Using his test setup the apparent flow velocity v_a, the angle of attack α, the sideslip angle β_s and the GPS coordinates and altitude were measured. From this and data collected by the ground station he was able to determine the aerodynamic coefficient C_R during a production flight.

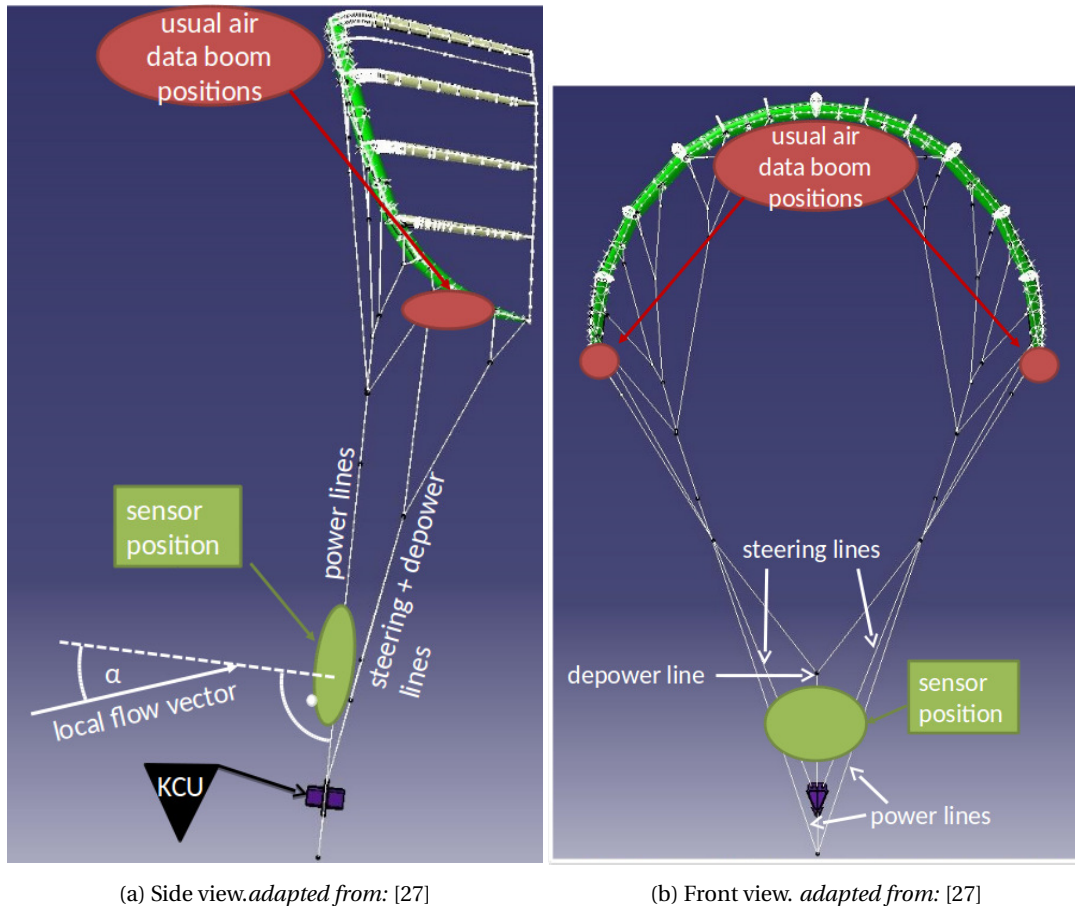(a) Side view. *adapted from:* [27]   (b) Front view. *adapted from:* [27]

Figure 1.13: Sensor position in the bridles below the kite and a definition of the inflow angles measured by the system designed by Oehler[27]

Based on the work performed by Oehler most sensors are copied from his setup. The uncertainties from his setup are given in table 1.2.

Table 1.2: The uncertainties in Oehlers test setup per sensor [27]

Sensor	Uncertainty in measurement
Wind vanes	1.88^o
Pitot tube	$0.86\ m \cdot s^{-1}$

One issue with the setup of Oehler however is the indepencency of the angle of attack of the kite with the angles that the bridle system experiences. A different power setting changes the angle of attack of the kite in another manner than the bridle system changes attitude.

Research goal

The aim of this study is to improve the flight models currently available for the 20 kW Kitepower system of Kitepower and and validate them. This is done by experimentally determining the exact turning rates and creating an aerodynamic model for the kite system which is validated using flight test data. The research questions are:

1. What is the current aerodynamic model for the 20 kW kite used at Kitepower?

    (a) Which assumptions are used?

    (b) What kind of control is in place?

    (c) What can and should be improved?

2. What are the different values for the aerodynamic moment coefficients for the 20 kW kite?

    (a) How are the coefficients defined for kite flight dynamics?

    (b) What experiments are needed to determine the coefficients?

3. How are the coefficients incorporated in the current aerodynamic model of the kite used at Kitepower?

    (a) How well does the current model compare to the results from the experiments?

    (b) Can a simplified model still effectively show the behavior encountered in the experiments?

4. What causes the moment coefficients to have these values?

    (a) What is the current theory of turning dynamics for kites?

    (b) What is the turning mechanism for the kite shown from the experiments?

    (c) Does a model show the same mechanisms that were found in the experiments?

    (d) Can the model accurately compute the values for the turning coefficients based on design inputs?

Current situation

In order to be able to improve the system that is currently used at the Kitepower company first it has to be established what the system entails at the moment. Based on the research goal several questions arise.

What is the current aerodynamic model for the 20 kW kite used at Kitepower?

Currently Kitepower is in an extensive testing period to make their working system robust enough that a near infinite autonomous control is allowed for commercial use. The current focus of research is not on the optimization of the flight path but rather on the safety of the system and the consistency of the controls.

This is the reason that the current control is the simplest that one might imagine, when the kite needs to steer right the right line is pulled, when the kite needs to steer left the left line is pulled. The only assumption that is in place is that there is a linear relation between the amount of steering and the rotational speeds achieved by the steering. For every kite that is used (several different prototypes are currently in use) a different amount of maximum steering and power setting is defined as to not stall the kite in flight.

The control of the kite is taken care of by means of a Kite Control Unit or KCU. Figure 1.13 shows where this KCU is positioned with respect to the kite. The KCU has a connection to the ground station where the desired flight paths are defined. Then two motors can reel in and reel out the steering lines and the power setting lines which activates the system in a manner that is similar to how a kitesurfer would steer a kite. This line setup is also shown in figure 1.14.

What are the different values for the aerodynamic moment coefficients for the 20 kW kite?

The coeffients for these kites are not defined in a manner that is normal for aircraft. But as Fagiano[13] and Erhard[11] show a turn rate law is a surprisingly good way to show for a kite how effective it steers based on control inputs. But since the current system design is not yet focussed on flight path optimization the precise values for all the different kites are not known and thus not implemented in the control system.
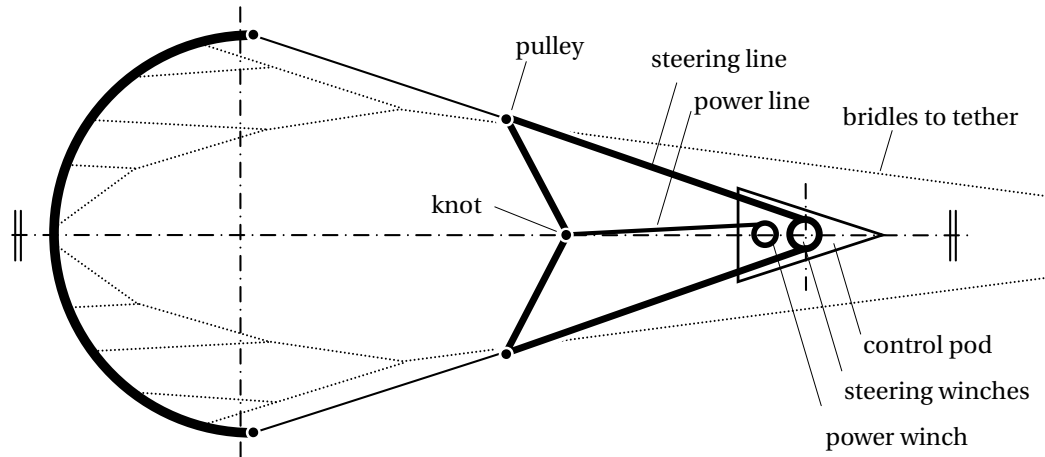

Figure 1.14: The Kite Control Unit [KCU] and activation lines with kite layout. The system acts as a kitesurfer would where the power setting and steering are two different lines but activate the same control surfaces. *source:*[22]

Research approach

In order to improve the flight models used at Kitepower first the theoretical basis of current models is expanded to include the quantitative influence of the flexibility of the kite. An attempt is made to build on qualitative theory provided by Breukels [6].

To validate these models experiments are needed where the different aerodynamic coefficients are measured together with the flow environment of the kite and the deformations. The first coefficient that will be measured is the C_R which is the nondimensional value for the amount of force a given kite is able to produce. It is defined as:

$$C_R = \frac{F_T}{\frac{1}{2}\rho v_a^2 A},$$

(1.11)

where F_T is the tether force, ρ is the density of the air, v_a is the apparent flow velocity, and A is the projected surface area. From these parameters the unknowns that need to be measured by the test setup are the tether force F_T, the density ρ, and the apparent wind velocity v_a. The lift force for any lift producing airfoil will change with the angle of attack α. For use in models this parameter is significantly more usefull than the power setting that was defined in the work of Python [30] for example. Therefore this angle needs to be determined as well.

For describing the turning behaviour of a flexible kite the deformations need to be defined as a result of a given steering input δ. It is assumed that the two sides of the kites are responsible for the steering of kites and that these deformations are not symmetric. This means that the deformations on both sides needs to be measured with respect to the center of the kite which is assumed to contribute little to any turning. Besides this the rate at which the kite rotates along the yawing axis needs to be measured to relate the deformations to their intended effect. This means that the test setup needs to measure the yaw rate $\dot{\gamma}$, and the Euler angles pitch θ, roll ϕ, and yaw γ on both sides and the center to see how the kite deforms. The angles of attack for the two sides will also be dependent on the sideslip angle β_s which therefore also should be measured.

All of the measured parameters together will be put together in one test setup shown in figure 1.15

IMU for attitude θ, ϕ, and γ
Pitot tube for v_a
wind vanes for
angles α and β_s

kite

power line

IMU

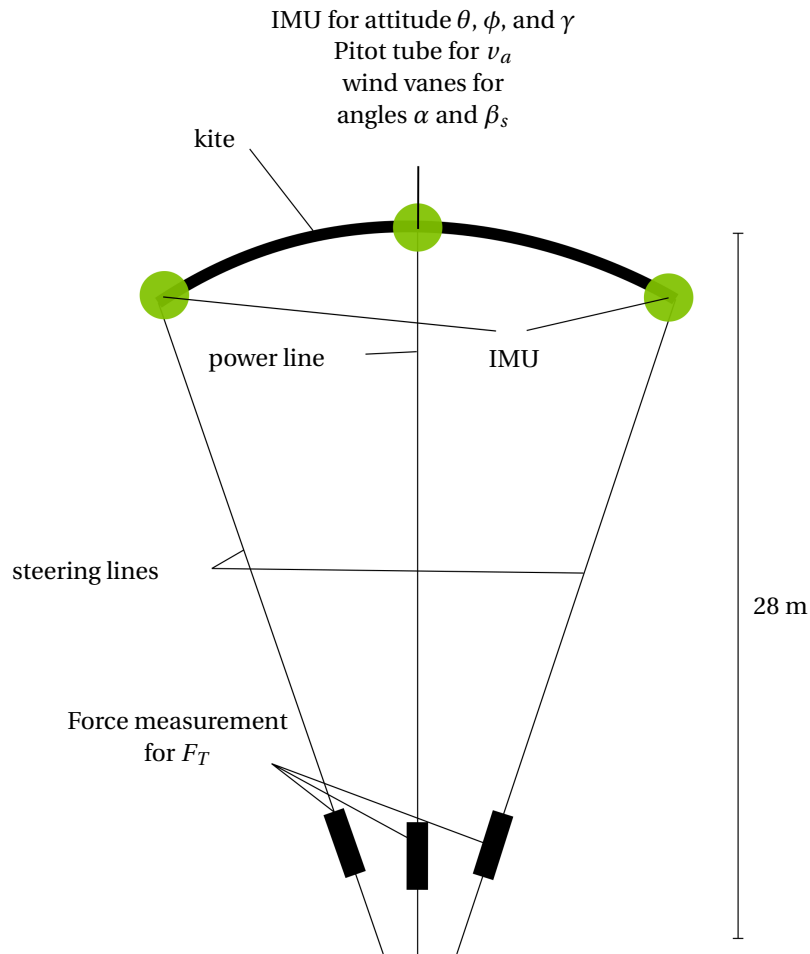steering lines

28 m

Force measurement
for F_T

Figure 1.15: The test setup that is needed to validate the theory on performance of kites and the deformations that drive their steering behaviour.

Now first chapter 2 will show the expanded theory on the kite deformations and how these influence the turning behaviour of the kite. Then chapter 3 will explain the test setup and the test plan. Chapter 4 will then show how the analysis of the experiments are done and explain several corrections needed to asses the data. The results of the experiments are shown in chapter 6 and the model provided in chapter 2 will be assesed using these results. Then finally conclusions and recommendations are given in chapters 7, and 8 respectively.

<div style="text-align: right; font-size: 4em;">2</div>

Turning mechanism

Breukels [6] presents a qualitative model to explain how the deformations cause a kite to turn due to a steering input. He later presents a model that show the relative influence the different mechanisms have based on a computational model he created using a multi body approach. Here the qualitative model is worked out to show the quantitative influence the different mechanisms have on the yaw rate of any given kite that has a relatively flat center and steering surfaces that have a significant dihedral angle.

Warping mechanism

The turning of flexible kites knows several explanations. The two main ones for yaw turning flexible kites are wing warping and the change in drag forces due to an increased angle of attack. To be able to quantify the influence of the two seperate explanations we accept that both of these mechanisms have an effect and that they are together the result of the flexibility of the kite.

When a kite needs to be directed in another direction one pulls on the back of the side you want to go it to. Figure 2.2 shows how a warped wing has deformed with respect to it was before the warping which is shown in figure 2.1. The top view shows that the right side has moved backwards, in this figure it is attempted to move to the left (relative to the topview). The front of the kite is defined as the light part of the gradient and the back as the dark part.

Figure 2.1: From left to right, Top view, front view, and side view of a kite in normal operation.

An overview of the forces is shown in figure 2.3. The warping offsets the forces S_1 and S_2 by the amount $\frac{b}{2}\sin(v)$ where b is the wingspan and v is the warping angle of the kite. The sideforces are caused by the steering surfaces as these surfaces are directe perpendicular to the top of the kite the local aerodynamic lift forces are directed to the sides. The total moment that is caused by this phenomenon now becomes:

$$M_{\text{warp}} = (S_1 + S_2)\sin(v)\frac{b}{2}. \tag{2.1}$$

The actual moment is thus related to the forces S_1 and S_2 . These are found to be:

$$S_i = \frac{1}{2}\rho_\infty v_a^2 A_i C_L(\alpha_i), \tag{2.2}$$
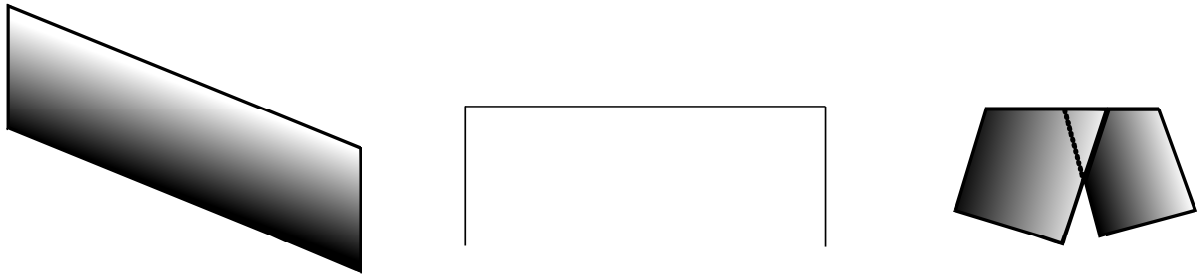
19

Figure 2.2: From left to right, Top view, front view, and side view of a kite that is warped. This deformation is due to a pull on the left side (in the top view figure)
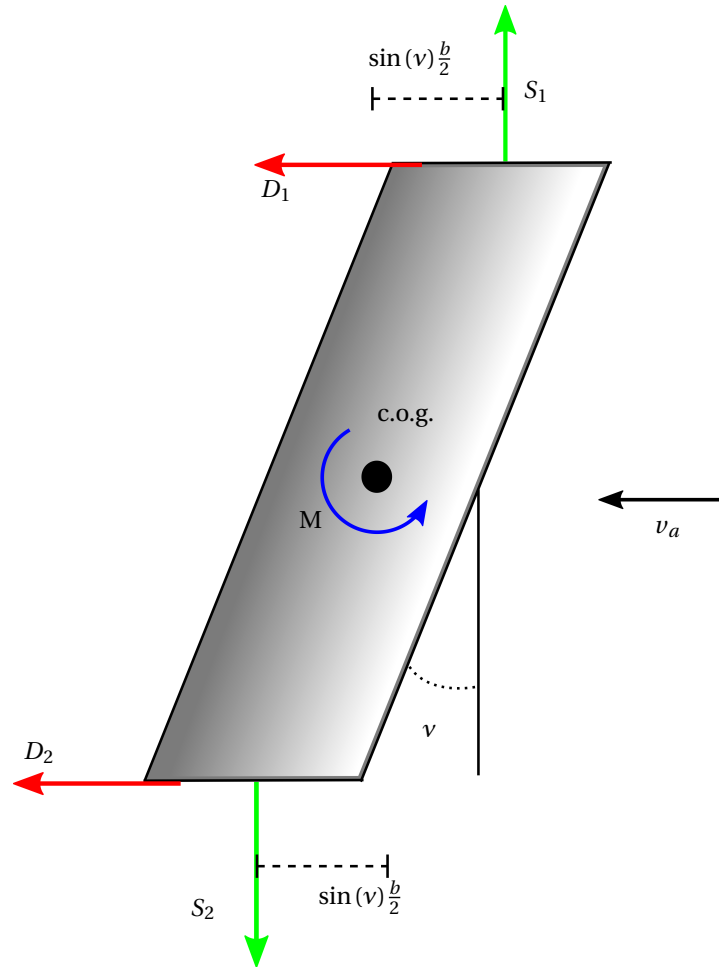

Figure 2.3: The forces on a warped kite, the offset of the so called sideforces S_1 and S_2 creates a moment force that yaws the kite. v is the warping angle of the kite, $c.o.g.$ is the location of the center of gravity, M is the resultant moment force, v_a is the apparent wind velocity, and D_1 and D_2 are the drag forces.

where ρ_∞ is the density of the free flow, v_a is the apparent wind speed, A is the area of the section that creates the force and $C_L(\alpha)$ is the nondimensional lift coefficient as a function of the local angle of attack α. The same goes for the resulting drag forces that can be seen in figure 2.3:

$$D_i = \frac{1}{2}\rho_\infty v_a^2 A_i C_D(\alpha_i). \tag{2.3}$$

This now describes how the kite rotates around the yaw axis. The kite however during a turning motion also translates mass in the direction it turns into.

Upward forces perpendicular to the plane of the turning direction do not affect this motion. The same

applies to the drag forces Therefore only the side force S1 and S2 are responsible for the motion and a difference between the two is required for a net force. According to this explanation the difference between S_1 and S_2 is found after some turning has already taken place. Due to the rotation of the kite the steering part in the direction of the turn, S_1 in figure 2.3, will experience a higher angle of attack α, thus increasing the lift and drag forces. A similar thing happens for S_2 but here the angle of attack decreases, decreasing the lift and drag forces. Thus in this situation it is found that:

$$S_1(t_0) < S_1(t_1), \qquad S_2(t_0) > S_2(t_1). \tag{2.4}$$

This means that the combined increase on the side of S_1 and the decrease on the side of S_2 will combine into the force $\vec{F}_{\text{centripetal}}$ that is needed to translate the kite into the path of the desired turn:

$$\vec{S}_1(t_1) + \vec{S}_2(t_1) = \vec{F}_{\text{centripetal}}. \tag{2.5}$$

Differential drag mechanism

The other mechanism known to turn the kite is a difference in drag forces between the two steering sides. Here it is assumed that the local angles of attack are at such a value that pulling on it for the angle to increase leads to an increased lift and drag force as shown for S_2 and D_2. Letting go on the other hand, as can be seen for S_1 and D_1 leads to a smaller lift and drag force. For given airfoils this relation between change in angle of attack and the lift and drag force might differ, here however it is assumed that most kites used for power generation follow this relation.
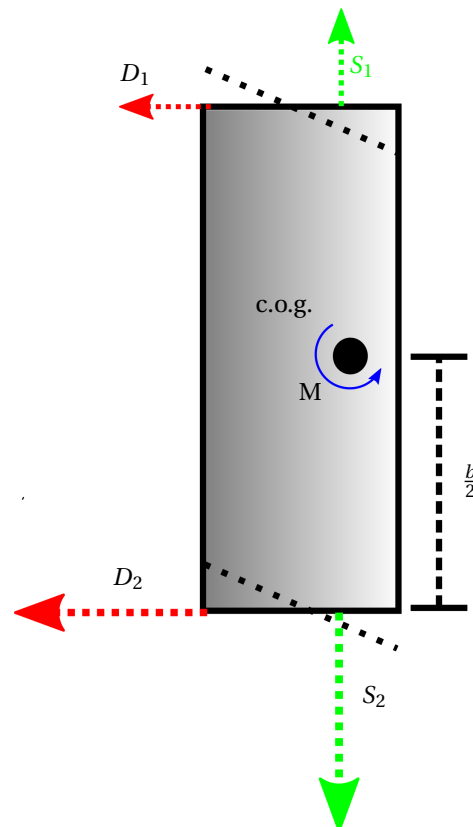

Figure 2.4: The changes in angle of attack due to the pulling on the bottom side and the letting go of the top side changes the local angles of attack resulting in a change in lift and drag forces.

The resulting moment seen in figure 2.4 is now caused by the difference in the drag forces. The sideforces S_1 and S_2 seen here are assumed to be directed in line with the center of gravity, this might not be the case but the moment arm will be relatively small compared to that of the drag forces and are therefore neglected

in this derivation.

Now the resulting moment can be defined as:

$$M_{\text{diffdrag}} = (D_2 - D_1)\frac{b}{2}. \tag{2.6}$$

And the drag forces follow the relation given in equation 2.3. Now one might argue however that any deformation given by the warping will automatically be present in the drag differential moment arms as well. since these deformations happen at the same time. For clarity in explaining the two different phenomena this is however not shown in figure 2.4 but it should be taken into account. Equation 2.6 can thus be transformed to:

$$M_{\text{diffdrag}} = (D_2 - D_1)\frac{b}{2}\cos(v). \tag{2.7}$$

Yaw rate

Now the different moments are provided in equations 2.1 and 2.7 the relation to the actual yaw rate can be found. In order to properly know the resulting moment that acts on the the kite also the mass moment of inertia from section 4.3 is needed:

$$I_\gamma = \frac{M}{\ddot{\gamma}}, \tag{2.8}$$

where I_γ is the mass moment of inertia for the yaw axis, M is the resulting moment around the yaw axis and $\ddot{\gamma}$ is the yaw acceleration. For the kite system both the yaw acceleration and the mass moment of inertia are known, thus it is possible to determine the resultant moment during the first part of the turn where the yaw rate increases.

However during a usual turn the kite will follow a path that is very similar to a circular arc as shown in figure 2.5. And during this movement the yaw rate will remain constant. This means that there is no longer an effective moment acting on the yaw axis of the kite since $\ddot{\gamma} = 0$. For this part of a turn there is thus a moment equilibruim present on the kite. Both the drag differential and the warping of the kite have counteracting phenomena that stop the kite from accelerating the yawing motion.

There are two counteracting options as to how this equilibrium is established. The first one is a the difference in velocity that both sides experience during a turning motion the second one is a sideslip that the kite experiences during a turn. Figure 2.6 shows how for a counter clockwise turn the induced velocities behave. This can also be given in equative form as:

$$v_i(y) = \dot{\gamma}y. \tag{2.9}$$

Thus at the steering surfaces the induced velocity will be simply where $y = b/2, -b/2$ so:

$$v_i(b/2) = \dot{\gamma}\frac{b}{2}. \tag{2.10}$$

Now the resulting force will be a function of the velocity experienced by the local airfoil. That means that the aparrent wind velocity has to be added to this induced velocity:

$$v_{\text{local}}(y) = v_a + v_i(y) = v_a + \dot{\gamma}y. \tag{2.11}$$

Figure 2.7 shows how the local apparent wind velocity $v_{\text{local}}(y)$ behaves during a turn while moving with a velocity of v_a and a rotational velocity $\dot{\gamma}$

Thus to calculate the moment that is created along the topside of the kite we need to integrate along the top part of the kite [-b → b]. For any given local strip of airfoil we know that the drag force is (which is the part of the aerodyanamic forces that has an arm that is unequal to zero wrt the yaw axis):

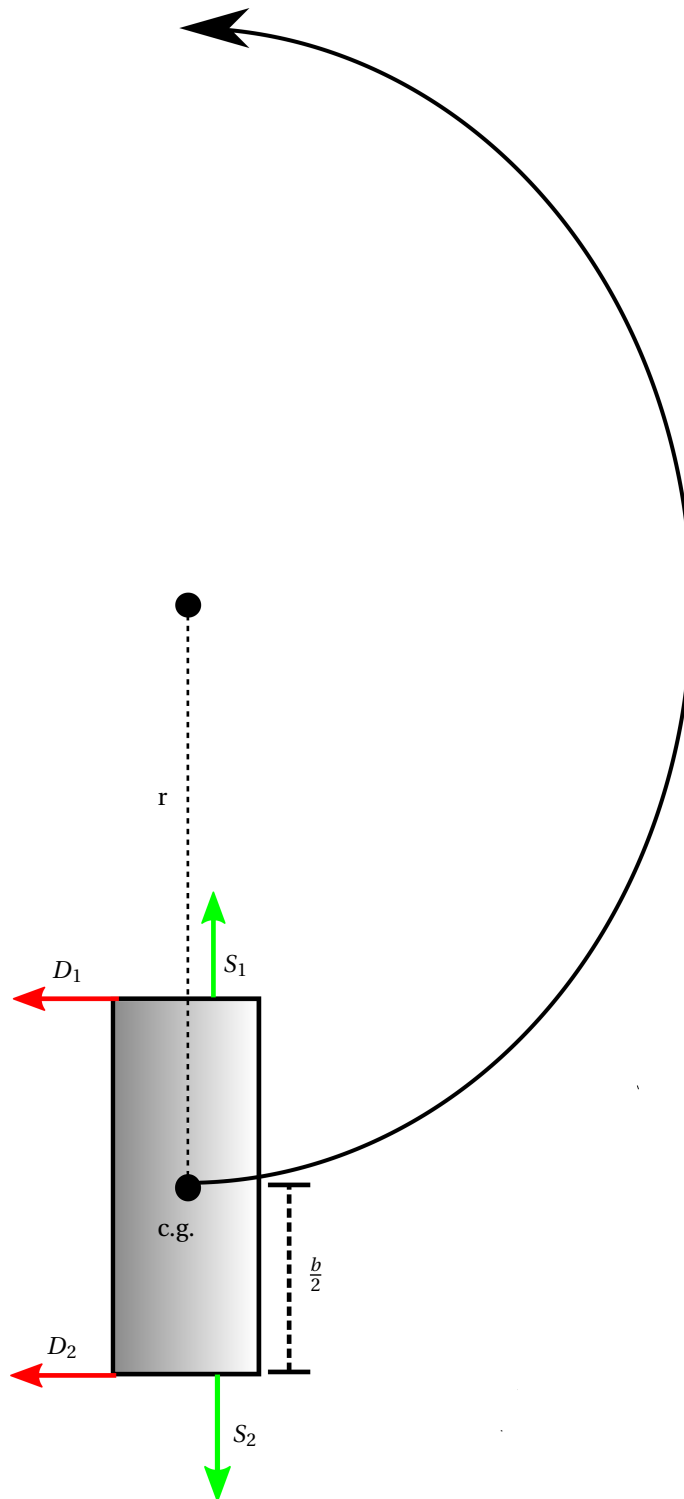$$dM_{\text{top}} = y\frac{1}{2}\rho_\infty v_{\text{local}}(y)^2 c(y) C_D(\alpha(y))\mathrm{d}y. \tag{2.12}$$

Figure 2.5: During normal operations in flying figures of eight a power producing kite will move from straight flight in a circular turn. During this constant turn the yaw moment is 0.
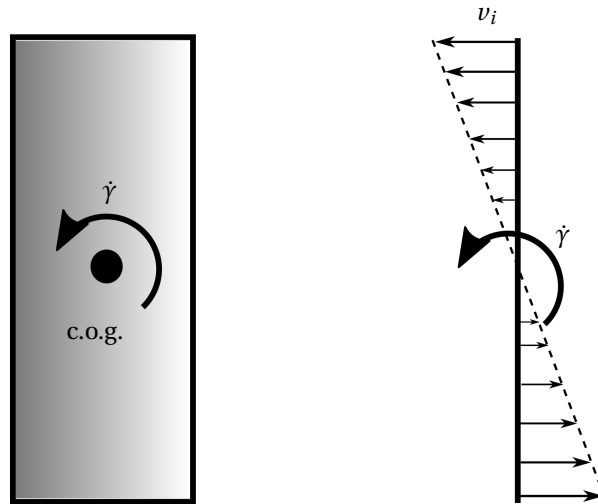
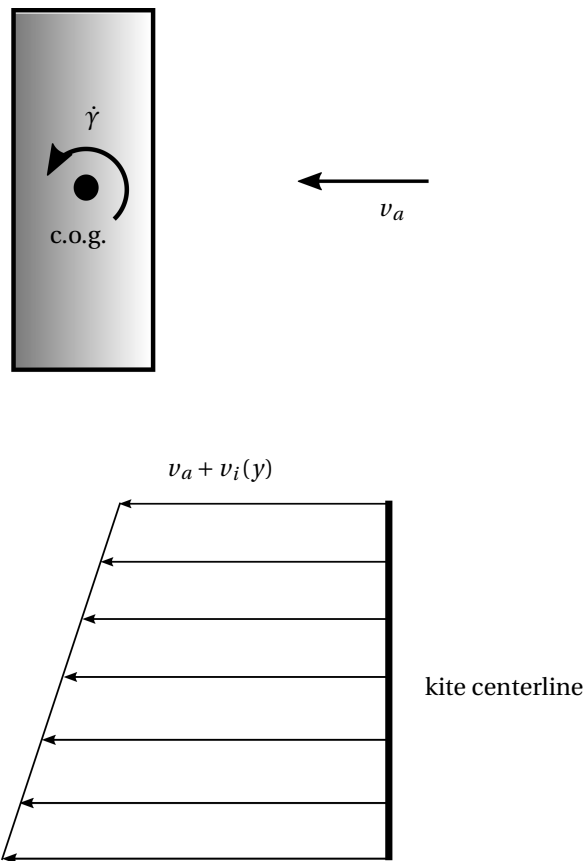Figure 2.6: The turning of a kite induces a velocity upon itself that is related to the yaw rate $\dot{\gamma}$.

Figure 2.7: The apparent wind velocity as the kite experiences along it's span during a constant turn of $\dot{\gamma}$.

Where dM_{top} is the infinitessimal amount of moment, y is the moment arm of the infinnitessimal strip to the center of gravity, $v_{\text{local}}(y)$ is the local apparent wind velocity, $c(y)$ is the local chord length, and $C_D(\alpha(y))$ is the local drag coefficient.

Then the total moment induced by the different velocities along the top of the kite will be:

$$M_{\text{top}} = \int_{-b/2}^{b/2} y \frac{1}{2} \rho_\infty v_{\text{local}}(y)^2 c(y) C_D(\alpha(y)) \mathrm{d}y. \tag{2.13}$$

This integral can be simplified by the fact that we assume the kite to be square, have a single angle of attack and changes in density of the flow field are negligible which means α, $c(y)$, C_D, and ρ are all constants. Then equation 2.13 can be written as:

$$M_{\text{top}} = \frac{1}{2}\rho_\infty c C_D(\alpha) \int_{-b/2}^{b/2} y v_{\text{local}}(y)^2 \mathrm{d}y. \tag{2.14}$$

On the steering sides there is also a moment inducing difference in velocity. In this case it is simpler since the entire steering area is located at a single distance from the center of gravity, thus the velocity is also a constant. The moment induced by the sides becomes:

$$M_{\text{sides}} = \frac{1}{2}\rho_\infty A b \left(v_{\text{local}}(-b/2)^2 C_D(\alpha_1) - v_{\text{local}}(b/2)^2 C_D(\alpha_2) \right). \tag{2.15}$$

Within equation 2.15 also the second means of counteracting the initial moment forces is hidden. The sideslip angle manifests its influence on the moment forces in the terms $C_D(\alpha_1)$ and $C_D(\alpha_2)$. Since a sideslip angle would in the right situation be able to counteract any change in angle of attack by simply responding with an equally large negative sideslip angle. This means that the original angle of attack or even a smaller one can be existent on the sides returning them to their original situations where there was no difference in the magnitude of forces.

But since it is known that the sum of all the moment terms needs to be zero the following relation should be satisfied:

$$\sum M = 0 = M_{\text{warp}} + M_{\text{dragdiff}} + M_{\text{top}} + M_{\text{sides}} = (S_1 + S_2)\sin(v)\frac{b}{2}$$
$$+ \frac{1}{2}\rho_\infty c C_D(\alpha) \int_{-b/2}^{b/2} y v_{\text{local}}(y)^2 \mathrm{d}y + \frac{1}{2}\rho_\infty A \frac{b}{2} \left(v_{\text{local}}(b/2)^2 C_D(\alpha_1) - v_{\text{local}}(-b/2)^2 C_D(\alpha_2) \right) \frac{b}{2}\cos(v), \tag{2.16}$$

Here the M_{dragdiff} and M_{Sides} are taken as one term in the RHS of the equation, the influence for the drag difference is in the angle of attack and the influence of the M_{sides} is in the one where the difference in velocity and angle v are the cause.

There is however another relation that needs to hold in order for the kite to follow the circular path. That is the one of a mass following a circular orbit. For this movement a centripetal force is needed. The known force that is needed to move in a circular movement is:

$$\vec{F}_{\text{centripetal}} = \frac{mv^2}{r}, \tag{2.17}$$

where F is the resultant force directed at the center of the circle on which the movement is taking place, m is the mass of the system, v is the velocity, and r is the radius of the circle on which the movement is taking place.

In order for the kite to move in this circular path the sum of the forces needs to result in this centripetal force. The only means by which this sum is possible is the combination of steering side forces to combine into this as given in equation 2.5, thus it is required that:

$$\vec{S}_1 + \vec{S}_2 = \frac{1}{2}\rho_\infty A \left(V_1^2 C_L(\alpha_1) - V_2^2 C_L(\alpha_2) \right) = \frac{mv_a^2}{r}. \tag{2.18}$$

Now when the integral in equation 2.16 is solved and a part of the warping term is replaced with the centripetal force equation from equation 2.18 the relation becomes:

$$\sum M = \frac{mv_a^2}{r}\sin(v)\frac{b}{2} + \frac{2}{3}\rho_\infty A_{\text{top}} C_D(\alpha_{\text{top}}) v_a \dot{\gamma} \left(\frac{b}{2}\right)^2$$
$$+ \frac{1}{2}\rho_\infty A \frac{b}{2} \left(v_{\text{local}}(b/2)^2 C_D(\alpha_1) - v_{\text{local}}(-b/2)^2 C_D(\alpha_2) \right) \frac{b}{2}\cos(v) = 0. \tag{2.19}$$

Sideslip angle β_s

From the theory shown here it is evident that the sideslip angle β_s is not neccesarily responsible for the turning of the kites. In fact this analysis shows that the two different means of steering allow sideslip angles in two directions or a turn where there is no sideslip at all. To explain this three extreme cases are discussed here. These cases use force distributions that will not likely occur in real life but are intended to clarify what the possibilities are concerning the turning of kites and the sideslip angle.

Positive sideslip angle

The sideslip angle at this point is defined as positive if the angle measured is in the direction of rotation of the kite as shown in figure 2.8. This situation could occur when a fictitious situation occurs where the angles at the two sides change in such a way that at the left side (as seen in the direction of movement) produces extra lift and the right side produces less lift. These changes in lift are then not accompanied by a change in drag forces or wing warping. Or when a more realistic setup is considered some added drag by means of a drag flap of some sort is applied at the right side.
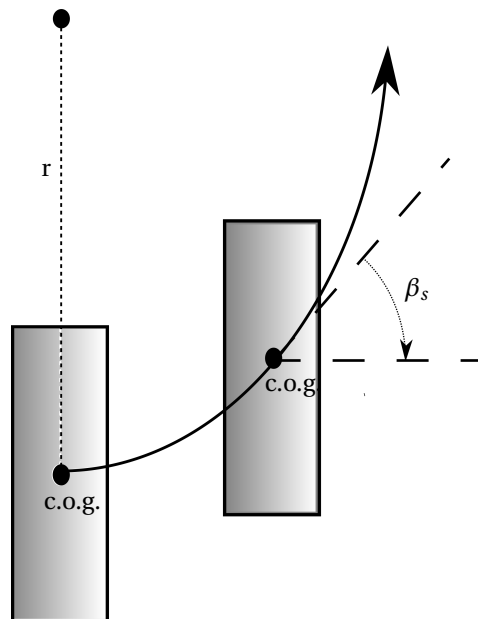
Figure 2.8: The sideslip angle is defined as positive when the kite is not turned into the direction of the rotation.

Negative sideslip angle

A negative sideslip angle occurs when the forces that rotate the kite are relatively dominant compared to any changes in lift in the direction that the kite needs to turn. So when for example only wing warping occcurs and the forces stay exactly the same. This will rotate the kite but actually not change its path at all.

Zero sideslip angle

The last situation is one where no sideslip angle occurs at all. This happens when the rotational moment forces and the acceleration forces towards the center of rotation are aligned perfectly with the mass that needs to be accelerated and the mass moment of inertia of the entire system. One of the benefits of this setup could be that the deformations of the kite solely show what the forces of the kite are doing and where the forces that dictate the maneuver come from.
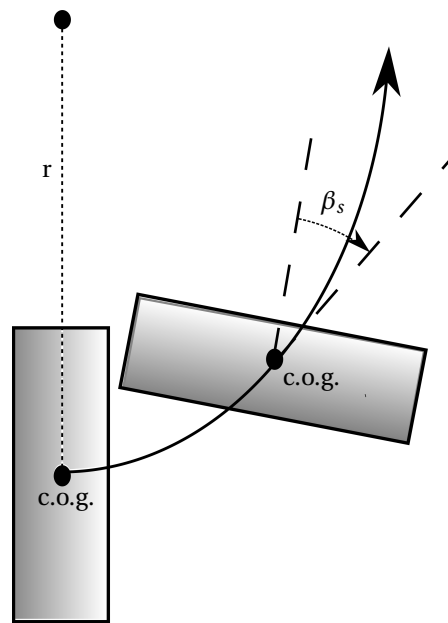
Figure 2.9: The sideslip angle is defined as negative when the windvane is turned into the direction that goes towards the direction the turn is in.
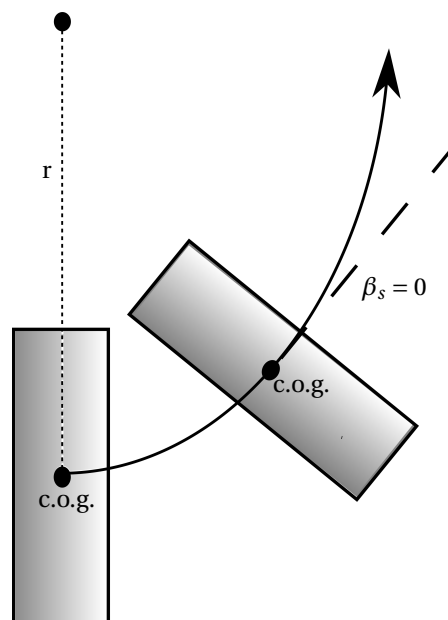

Figure 2.10: When the sideslip angle is zero the kite aligns perfectly with the arc that it is traveling on, in this case the heading of the kite is tangent to the local direction of the path.

3

Test setup

The test setup of the system consists of several parts and can be divided into two distinct parts, sensors on the ground and sensors on the kite. These sensors work in different reference frames but can be translated using translational matrices. The sensors on the kite are derived from [27] where a more elaborate description of the system can found. After that an overview of the locations of the sensors on the kite is given and the testing procedures are presented.

Following the research approach presented in chapter 1 the parameters that are measured by the test setup are:

Table 3.1: Variables measured by the test setup

Sensor name	**Sensor type**	**Location(s)**	**Measured variable(s)**
Pixhawk	inertial measurement unit	measurement boom left tip right tip	pitch angle θ $[deg]$ yaw angle γ $[deg]$ roll angle ϕ $[deg]$ pitch rate $\dot{\theta}$ $[deg \cdot s^{-1}]$ yaw rate $\dot{\gamma}$ $[deg \cdot s^{-1}]$ roll rate $\dot{\phi}$ $[deg \cdot s^{-1}]$ accelerations along X,Y,Z axis $[ms^{-2}]$
GPS module	GPS sensor peripheral for pixhawk[31]	measurement boom left tip right tip	GPS time [UTC] GPS lat, lon, alt GPS speeds $[ms^{-1}]$
Windvane α	flow direction measurement	measurement boom (front)	flow angle α $[deg]$
Windvane β_s	flow direction measurement	measurement boom (front)	flow angle β_s $[deg]$
Pitot tube	total and static pressure sensor	measurement boom (front)	apparent wind velocity v_a $[ms^{-1}]$
Force sensor box	force sensor	lines just above steering bar	power line tension $[N]$ right steering line tension $[N]$ left steering line tension $[N]$

Kite

The kite that is tested is the Hydra V5 from Genetrix Kiteboarding[4]. It is a leading edge inflatable kite with a 14 m^2 surface area. This is the kite that the current Kitepower system kites are based on and therefore particularly usefull to use as the kite to perform the experiments on.

Figure 3.1: Hydra V5 [4]

Table 3.2: Kite characteristics for the Hydra V5

Characteristic	Value
Surface area	14 $[m^2]$
Projected area	11.7 $[m^2]$
Kite mass	4.29 $[kg]$
Bar + line mass	1.6 $[kg]$
Number of struts	6
Number of lines	4
Wind range	9 - 30 $[kts]$

Measurement boom

The angle of attack on a kite is not easily measured. The flexibility of the canopy, leading edge and struts leave room for a device attached to any of these to measure local deformations instead of changes in angle of attack. To counter this a measurement boom is connected to the kite close to the trailing edge and on the leading edge. This significantly more rigid boom is then assumed to maintain a straight shape leading from the trailing edge to the leading edge.

The booms consist of three seperate carbon fibre beams, a single one that spans between the two center struts and is attached to the kite by means of the attached steering lines at those truts. Then there is a circular tube attached to this beam that points towards the leading edge. And finally there is a square hollow beam that goes over the long circular beam that points towards the leading edge. The square beam allows for sensors to be fastened in a specific attitude more easily.

To make sure that the square beam does not rotate a metal plate is attached that is placed under the leading edge inflatable tube. In this manner the roll atitude of the square beam is determined by the tangent of the leading edge tube. In theory the tube could deform in order for the central strut to rotate but it is assumed that in this direction the deformations are negligible during flight.

Pitot tube

The pitot tube shown in figure 3.2 measures the flow velocity. It does this by measuring the difference between the static pressure and the total pressure. By means of Bernoullis equation the flow velocity can be deduced. Bernoullis equation is often denoted as:

$$\frac{v^2}{2} + gz + \frac{p_{\text{static}}}{\rho} = \text{constant} \tag{3.1}$$

Where v is the velocity of the flow, g is the gravitational acceleration, z is the height of the current location on the streamline relative to a given reference plane, p_{static} is the static pressure, and ρ is the density of the air.

This equation however can be simplified when we assume that the alteration of the height is insignificantly small compared to the other terms, therefore the term gz is omitted. Then the equation can be used to relate two entities, the static pressure where the flow still has a velocity and one where the velocity goes to zero. In the latter one this means that the total pressure is found where all the kinetic energy is converted into pressure.

$$\frac{v^2}{2} + \frac{p_{\text{static}}}{\rho} = 0 + \frac{p_{\text{total}}}{\rho} \tag{3.2}$$

With p_{total} the total pressure. Since the velocity is the parameter that needs to be found and the static and total pressure are known from the measurement this equation is rewritten into:

$$v = \sqrt{\frac{2\left(p_{\text{total}} - p_{\text{static}}\right)}{\rho}} \tag{3.3}$$

Therefore it is possible to find the airspeed by means of these two pressures and the density. The density is found by using the ideal gas law in the molar form:

$$p = \rho R_{\text{specific}} T \tag{3.4}$$

Where p is the pressure, ρ is the density, R_{specific} is the specific gas constant, and T is the temperature in degrees Kelvin. The R_{specific} for air is known to be 286.9 $J/kg \cdot K$. This can be used to find the density when the temperature is known, and the temperature is measured by an additional sensor in the pitot tube.

Figure 3.2: The pitot tube in it's mount to attach it to the measuring boom.

As can be seen in figure 3.2 the pitot tube is fixed to the measuring device without being perfectly aligned with the flow velocity. This is not a problem however. When one looks at figure 3.3 it is clear that angle offsets that are less than 15 degrees will not affect the measurement greatly. Figure 3.3 simply shows the ratio between the measured velocity when the pitot tube is perfectly aligned versus when the tube is put at an angle. The relation is easily described as:

$$v_{\text{offset,Ratio}} = \cos(\theta), \tag{3.5}$$

where the region shown in figure 3.3 is assumed from regions in which normal airfoils usually operate in. This will be verified later when the angles of attack have been measured. The initial angle of the Pitot tube compared to the measuring boom is 10.8 deg pointing downwards.

Wind vanes α and β_s

Using magnetic angular measurement chips [1] and some simple 3D printed wind vanes the flow angles can be measured, these instruments are situated one meter in front of the kite to make sure the influence of the kite is not too large to determine the accurate inflow angles α and β_s of the kite. Figure 3.4 shows the wind-vane. The chip supplies a 0 - 3.3 DC voltage to one of the pixhawk input ports. This signal is later transformed into the appropriate angle during postprocessing. These windvanes are based on the work done by Oehler[27] which uses these several meters below a kite to measure incoming flow directions.
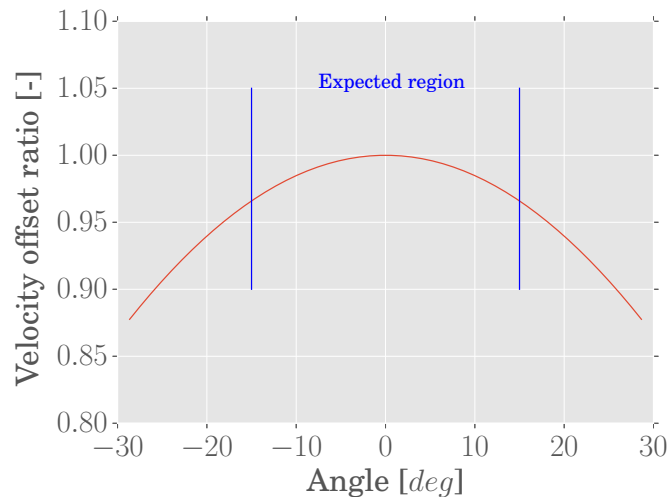
Figure 3.3: The offset ratio that is measured by the pitot tube based on the misalignment with the local flow. The expected region in operation is defined between the two blue lines.

Figure 3.4: One of the wind vanes used to measure the angle of attack.

Pixhawk

In order to measure the accelerations, angles, and angular velocities a Pixhawk [3] is used. These devices are normally applied for the steering of drones as the onboard computer is able to perform automated flight based on measured inputs. For the performed experiments in this study however it is usefull since it is also able to log all the information it receives to an sd-card with timestamps at a rate of 20 Hz. Figure 3.5 shows the pixhawk with a power bank to supply the power over a USB cable. The wind vanes and the pitot tube are also connected to the pixhawk which saves all data that these devices measure as well.

GPS module

Using a GPS peripheral as shown on figure 3.5 the position of the kite can be determined to an accuracy of several meters. Besides this the time is available which is required for comparing it to other times that are being logged on other pixhawks. It can also be very usefull for comparing the data to videos that have a timestamp so that certain behaviour shown in the data can be designated to specific phenomena occuring on video.

Force sensor box

In order to measure the aerodynamic properties of the kite the forces in the tethers need to be measured. This is done by means of load cells with strain gauges. The whole setup is given in appendix A. The cells themselves are attached to three tethers, one on the right steering line, one on the left steering line and one

Figure 3.5: A Pixhawk and together with a gps module, these are powered by a power bank over usb.

on the power lines. Figure 3.6 shows where they are attached. Figure 3.7 shows how the sensors are exactly attached to be able to measure the tether forces.
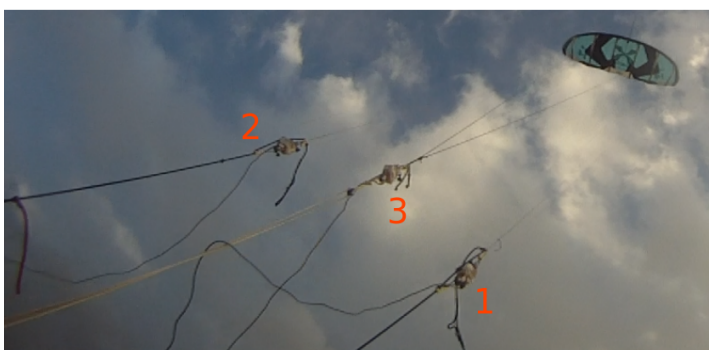
Figure 3.6: The force sensors are attached to the right steering line (1), the left steering line(2) and the power lines (3).
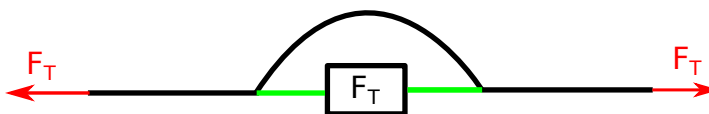
Figure 3.7: The force sensors are attached to the lines (black) and replace a piece of the line through which all forces now go (green). The force measurement device (block) is now strained dus to the tether forces.

Steering bar

A standard kite surf steering bar is used [2]. The bar length is 0.47 m. To quantify the steering offset the angle of the steering bar is measured visually by means of a video camera. The steering input then follows from:

$$\delta = 0.47 m \cdot \sin{(\angle_{\text{bar}})}, \tag{3.6}$$

with δ being the steering input in meters.

Figure 3.8: The steering bar used in the test setup. In order to steer in a direction the bar has to be pulled down on that side. The chicken loop is attached to the sandbad to secure the lines to a single point.

Overview

The whole test setup can be seen in figure 3.9 and an image showing how the central measurement boom is connected is shown in figure 3.10. In figure 3.9 all the devices are shown as they are attached to the kite (view from below the kite). One of the pixhawks that measures the angles at the side of the kite is shown after the cutoff piece, it is attached to the upper side of the fabric near the last piece of the leading edge inflatable tube.
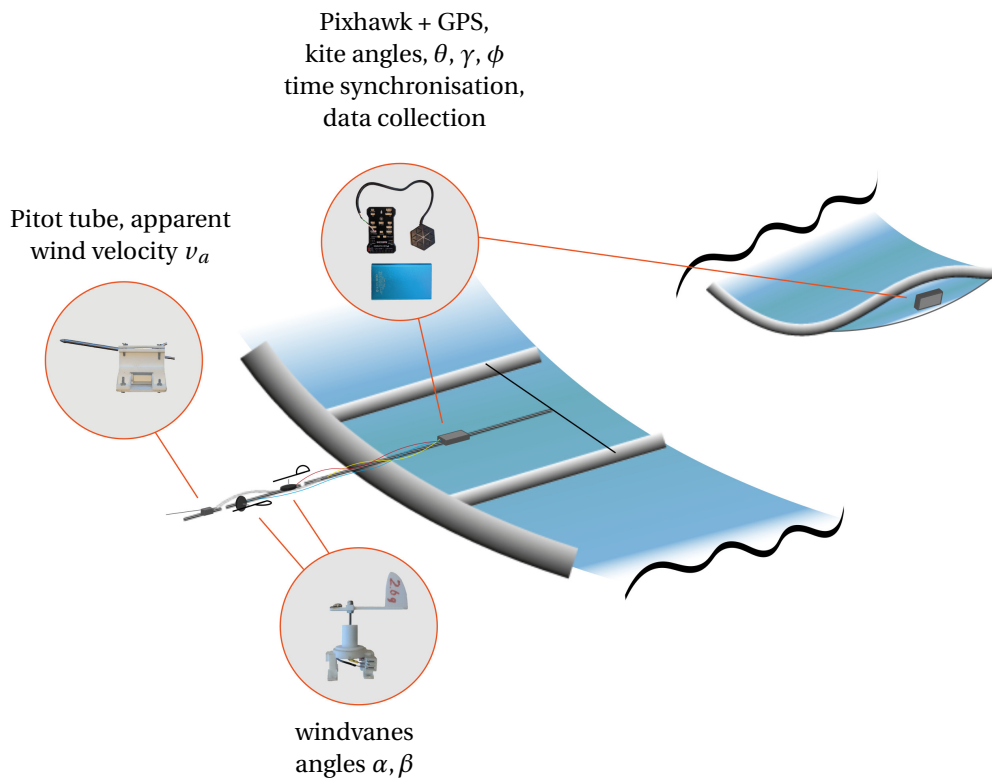
Figure 3.9: The whole test setup as it is connected to the kite. The system of carbon rods places the pitot tube and wind vanes in front of the kite to be able to measure undisturbed flow as good as possible. The middle pixhawk is rigidly attached to the rods to ensure it follows the angle of attack as it is seen by the rod itself. The two pixhawks attached to the sides of the kite are applied to the fabric using velcro.

Figure 3.10: The test boom is attached to the kite by means of a boom normal to the test bar. This normal boom is attached where the red and blue steering lines on the most central struts are attached.

Test strategy

Now the test setup is known the last part of the test is the different maneuvers and settings that will be applied to find all the required parameters. The tests will consist of a static part to find the global aerodynamic coefficients and then a dynamic part to provide information about the steering.

Static test

First the aerodynamic values need to be determined based on the angle of attack. When these are found they can be later used to quantify the forces that exist on different parts of the kite to steer. The plan is to set the power setting to a constant and test at a constant velocity to find the angle of attack that coincides with different power settings and the corresponding nondimensional aerodynamic coefficient. It was planned to test five different power settings that would relate to the results presented by Python [30]. However during the test the last power setting that was used stalled at points so this setting is omitted from the data. All the different values are shown in table 3.3. In total there are four different settings that are tested for one minute each. Testing each setting for one minute is assumed to be enough to obtain a statistically adequate dataset.

Table 3.3: The different values for the parameters that define the static maneuvers. The values are based on the comparable test performed by Python [30]

Velocity [kts]	Power setting [-]	different settings
± 22	0	
	1	
	2	
	3	
1	4	4

Dynamic test

The dynamic maneuvers should show how the kite behaves based on steering inputs. This will be done by means of steering with different steering inputs at different power settings. The steering will be set to one side and lasts untill a threshold has been reached. Table 3.4 shows the different settings that will be used for

different steering behaviour. In the end 8 combinations need to be tested. All of these need to be performed ±15 times which leads to 120 maneuvers.

Table 3.4: The different values for the parameters that define the static maneuvers. The values are based on the comparable test performed by Python [30]

Velocity [kts]	Power setting [-]	steering input [deg]	different settings
±22	0	8	
	1	20	
	2		
	3		
1	4	2	8

4

Analysis tools

In order to perform the analyses several principles need to be investigated. First the three different Pixhawks will be measuring in three different reference frames. In order to compare the values logged by all three transformations from one to the other are needed. Then the use of a testing boom will create some issues for the wind vanes with induced velocities that should be corrected for. And finally to figure out the forces that are driving the maneuvers a mass moment of inertia is established by means of an experiment.

Reference frames

To obtain the correct angles of attack at different locations on the kite several Inertial Measurement Units [IMU], also known as Pixhawks were placed. These IMU's register a quaternion that defines the direction and orientation of the device. The orientation of the incoming flow however also changes. To find the local flow velocities and angles of attack there is a need for translational matrices converting vectors from one reference frame to the other. The method to do this is explained thoroughly in [25] but here the ones used for the current investigation are given. First the different reference frames that are used are defined.

Local earth fixed reference frame

This referenc frame is the one in which all the pixhawks do their directional measurements. The Z-axis is defined as the gravitational center of the earth. The X-axis is defined as magnetic north and from this the Y-axis follows in this right-hand reference frame.

Wind kite reference frame

The wind kite reference frame is one that is pointed against the direction of the wind with the Z-axis directed at the center of gravity of the earth. It is assumed that the streamlines of the wind follow a path perpendicular to the X-axis and the Y-axis is defined by a right hand reference frame.

Body fixed reference frame

When the orientation of the kite is taken into account the frame is defined as the body fixed kite reference frame. Here the x-axis is in line with the heading of the kite. This also means that the pitch angle is now related to the X-axis of this reference frame. The X-axis is defined as the line that follows the path of the measuring boom attached to the kite during the experiments. The Y-axis or the pitch axis is defined as being tangent to the kite shape at the center of the kite. From this the Z-axis is defined downwards when the kite is located in the zenith position.

Local kite reference frame

The local kite reference frame can be defined along the span of the kite. Since the kite itself is a flexible structure different parts of the kite can have different deformations. This requires this work to deal with local reference frames that can cope with an attitude changing kite system. Here the definition of the X-axis is the one going from trailing edge to leading edge at the point being considered. The Y-axis now is defined as the tangent to the local kite surface when looking in the direction of the X-axis. From this the Z-axis is defined pointing towards the center of the kite.

Transformation matrices

To be able to switch from one of these frames to the other use can be made of transformation matrices [25]. In order to go from the local earth fixed reference frame to the body fixed frame the attitude of the kite is taken into account. The order of rotating around axes is first yaw γ then pitch θ then roll ϕ as shown in figure 4.1.
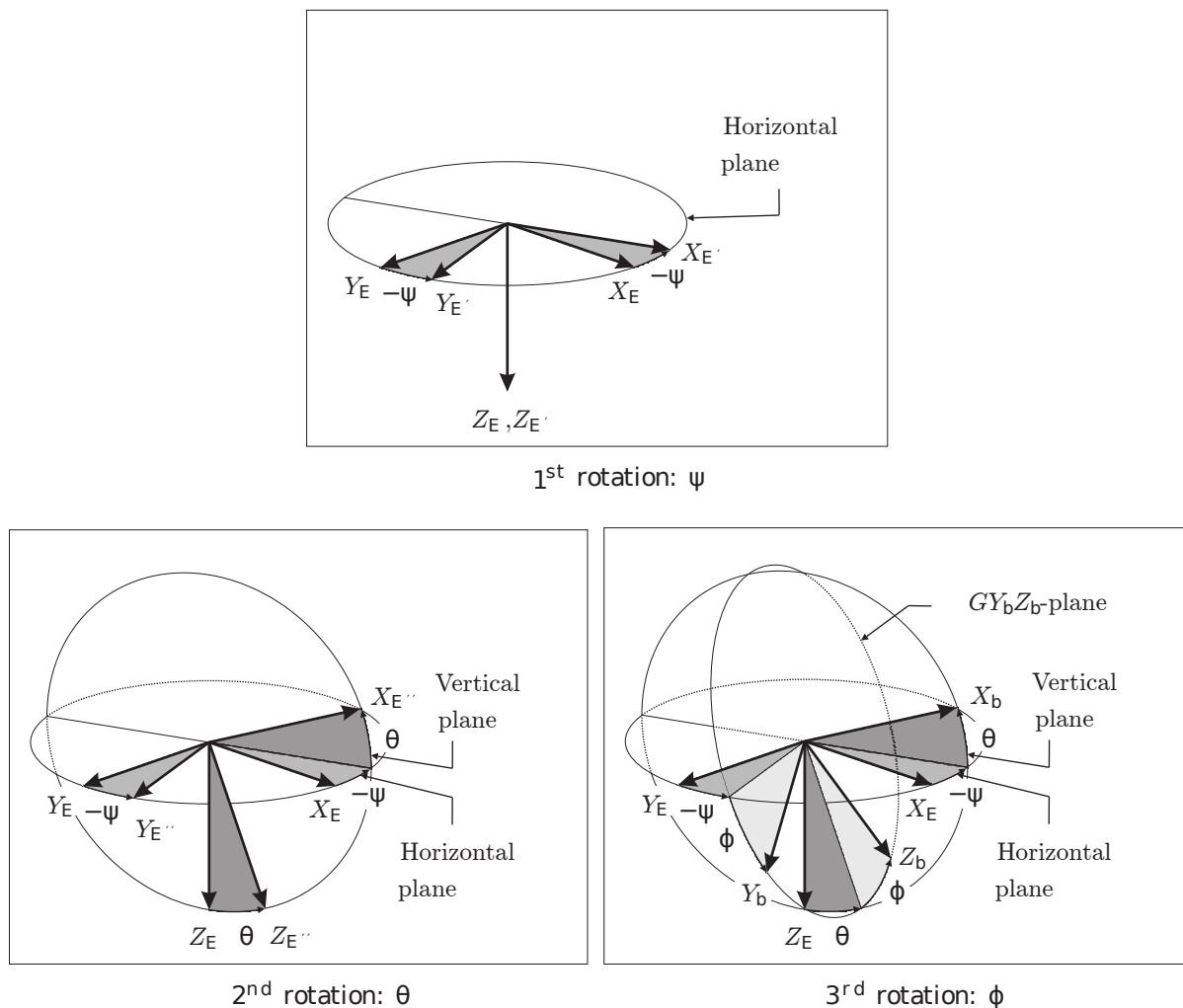
Figure 4.1: The rotations that the transformation matrices use to go from one reference frame to the other, the order is yaw, pitch roll.
source: [25]

Per rotation the matrices are given as:

$$\text{Yaw} \rightarrow T_{\text{F}'\text{F}} = \begin{bmatrix} \cos(\gamma) & \sin(\gamma) & 0 \\ -\sin(\gamma) & \cos(\gamma) & 0 \\ 0 & 0 & 1 \end{bmatrix} \tag{4.1}$$

$$\text{Pitch} \rightarrow T_{F''F'} = \begin{bmatrix} \cos(\theta) & 0 & -\sin(\theta) \\ 0 & 1 & 0 \\ \sin(\theta) & 0 & \cos(\theta) \end{bmatrix} \tag{4.2}$$

$$\text{Roll} \rightarrow T_{bF''} = \begin{bmatrix} 1 & 0 & 0 \\ 0 & \cos(\phi) & \sin(\phi) \\ 0 & -\sin(\phi) & \cos(\phi) \end{bmatrix} \tag{4.3}$$

With $T_{F'F}$ the rotation matrix around the yaw axis, $T_{F''F'}$ the rotation matrix around the pitch axis, and $T_{bF''}$ the rotation matrix around the roll axis. To go from the earth fixed reference frame to the body reference frame the matrices are simply mutliplied to find:

$$T_{bF} = T_{bF''} T_{F''F'} T_{F'F} \tag{4.4}$$

With T_{bF} the transformation matrix from the local earth reference frame to the body fixed reference frame. Now to go back from the body fixed reference frame to a local earth fixed reference frame the transformation is easy to find. Mulder[25] states: *"The eigenvalues of the transformation matrix must satisfy one of the following (orthogonalityproperty):*

- All eigenvalues 1.

- One eigenvalue is 1 and the other two are -1.

- One eigenvalue is 1 and the other two are complex conjugates of the form $e^{i\theta}$ and $e^{-i\theta}$.

The other criteria is given as: *"The determinant of the transformation matrix must be (normality property):"*

$$\det(T) \equiv 1$$

These criteria assure that the following can be used for the other matrices:

$$T_{ab}^{-1} = T_{ab}^{t} = T_{ba}, \qquad T_{ab}^{t} T_{ab} = T_{ab}^{-1} T_{ab} = I \tag{4.5}$$

This means that it is allowed to use:

$$\vec{V}_{\text{localearthfixed}} = T_{bF}^{t} \vec{V}_{b} \tag{4.6}$$

Where V_b is a vector defined in the body reference frame and $\vec{V}_{\text{localearthfixed}}$ is the same vector defined in the local earth fixed reference frame.

Deformations
In order to define the influence deformations have on the behaviour of the kite these reference frames are especially usefull. One might take a device that measures the orientation at the very tip of the kite as shown in figure 4.2. A manner in which one might translate the orientation of the angles found at the tip could be:

$$\vec{V}_b = T_{bE} T_{El} \vec{V}_l \tag{4.7}$$

Where T_{bE} is defined by the same matrix as in equation 4.4 but uses the angles γ_b, θ_b, and ϕ_b that are provided by the measurement device in the middle. And T_{El} is defined as the inverse of the matrix given in equation 4.4 but then with the angles γ_l, θ_l, and ϕ_l.

The pitch angle shown in figure 4.2 is found by transforming the unit vector in the direction of the X_l axis and transforming this vector to the kite body frame. Then the vector that is found here loses the dimension in the direction of Y_k to find the projection on the XZ-kite plane and the leftover components on the X_k and Z_k axis yield the following deformation angle.

$$\angle_{\text{pitch}} = -\arctan\left(\frac{\vec{V}_b \cdot \vec{Z}_k}{\vec{V}_b \cdot \vec{X}_k}\right) \tag{4.8}$$

The same procedure can be used for the other deformational angles defined by the Y_l and Z_l axes transformed to the kite reference frame.
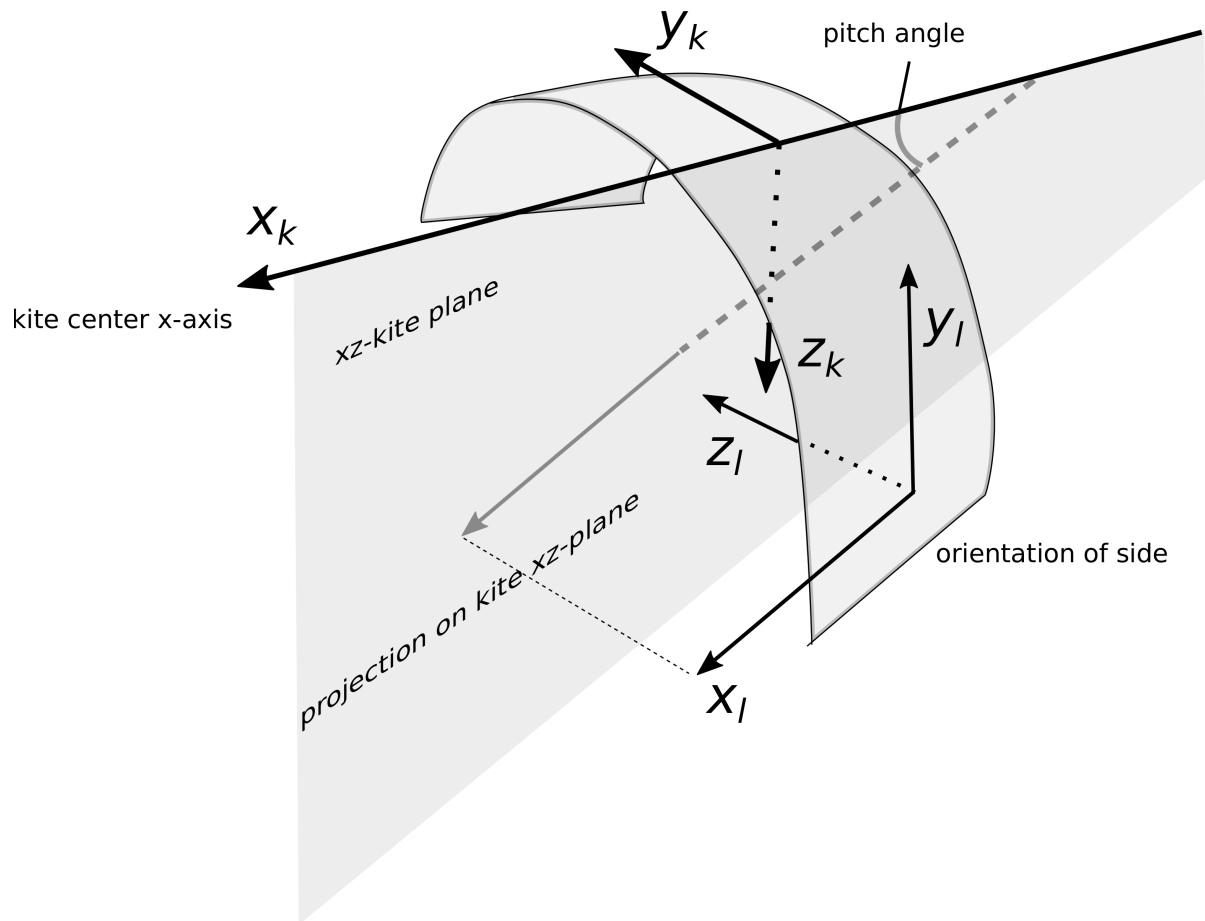
Figure 4.2: The projection of the measured angles at the tip of the kite on the XZ-plane of the body fixed reference frame. *adapted from:* [16]

$$\angle_{\text{roll}} = \arctan\left(\frac{\vec{V}_b \cdot \vec{Z}_k}{\vec{V}_b \cdot \vec{Y}_k}\right) \tag{4.9}$$

$$\angle_{\text{yaw}} = \arctan\left(\frac{\vec{V}_b \cdot \vec{Y}_k}{\vec{V}_b \cdot \vec{X}_k}\right) \tag{4.10}$$

For a deformation where the right side (pilot view) of the kite comes forward the new deformation angle is shown in figure 4.3. The old situation in shown in light blue. Now the angle with respect to the center axis is smaller.
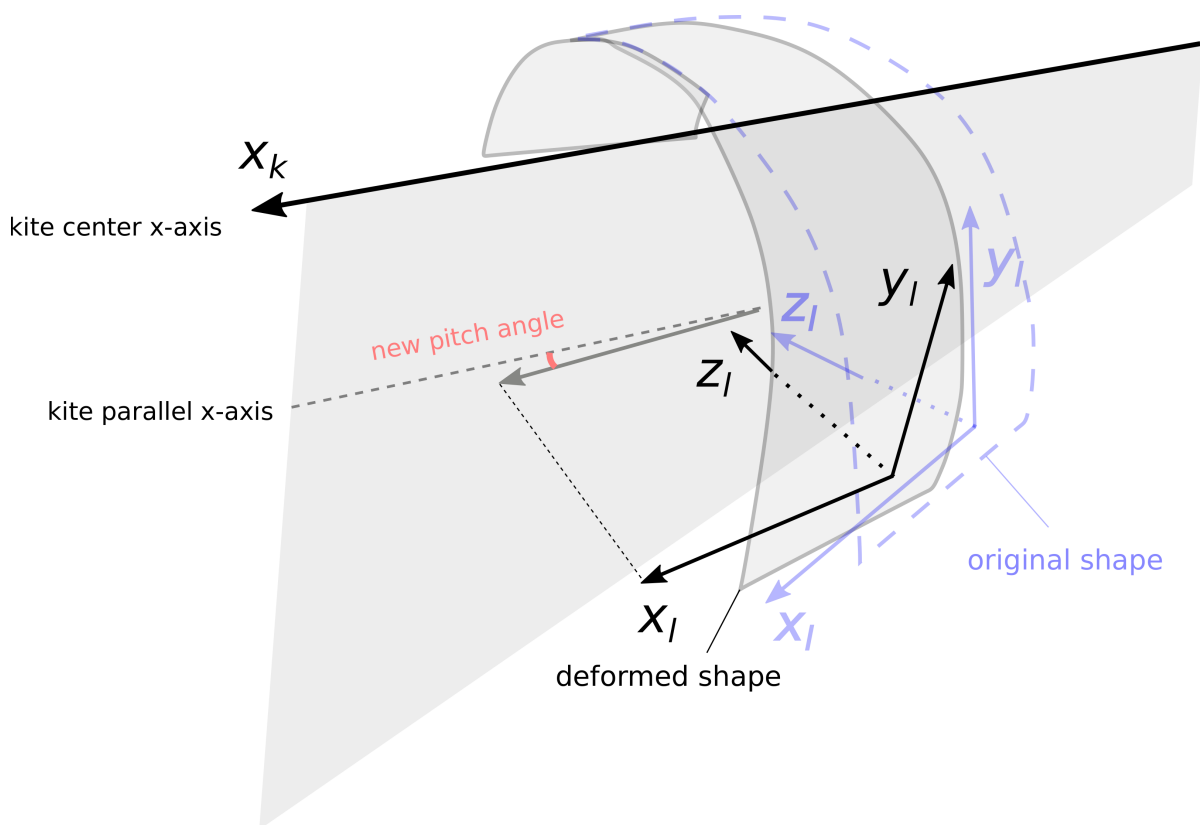
Figure 4.3: The projection of the measured angles at the tip of the kite on the XZ-plane of the body fixed reference frame after a control input is given and the kite deforms. *adapted from:* [16]
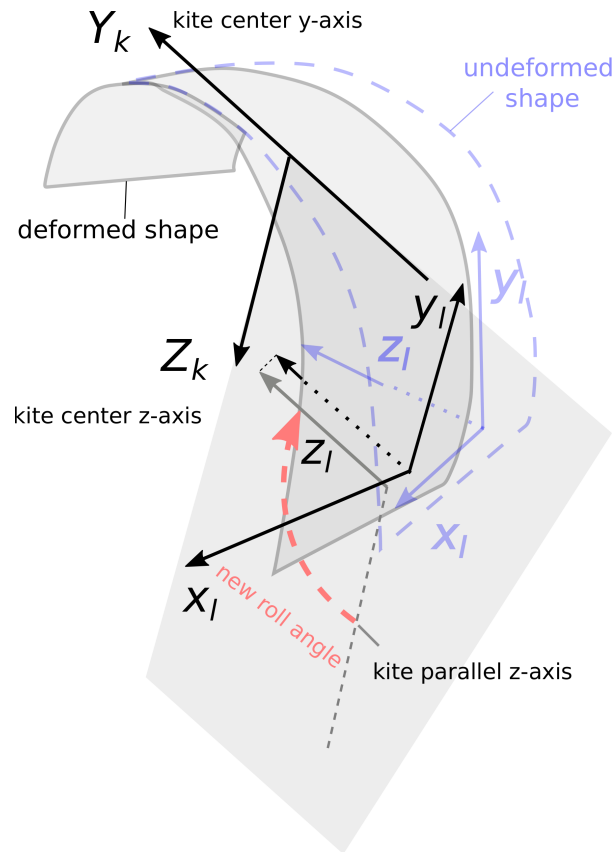
Figure 4.4: The projection of the measured roll angles at the tip of the kite on the YZ-plane of the body fixed reference frame after a control input is given and the kite deforms. *adapted from:* [16]
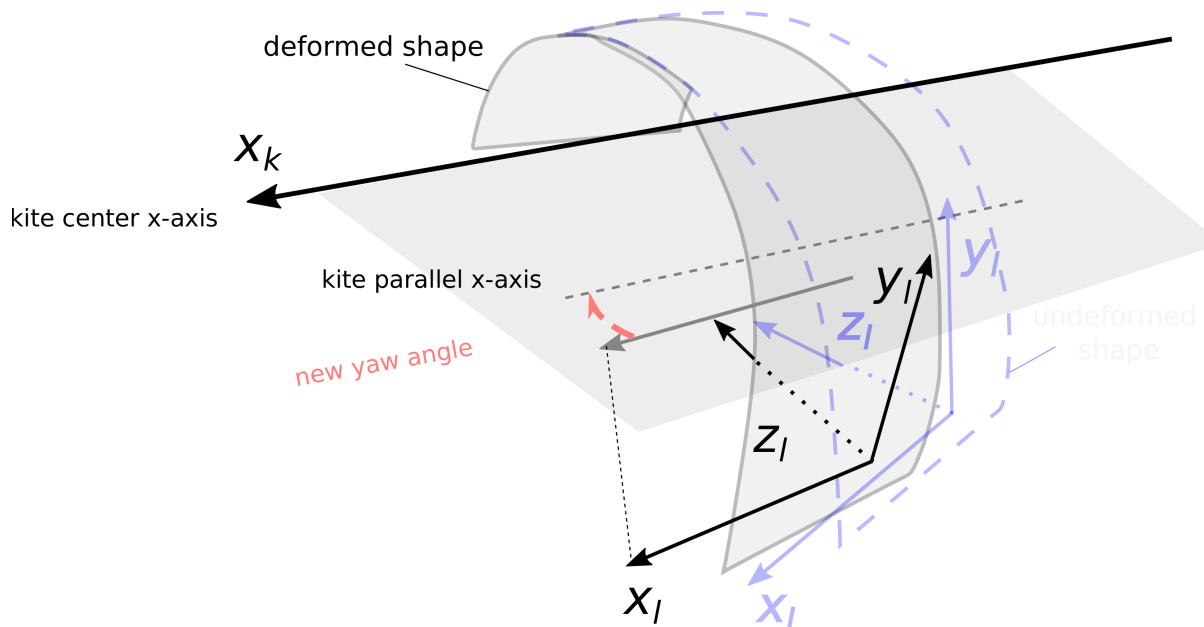
Figure 4.5: The projection of the measured yaw angles at the tip of the kite on the XY-plane of the body fixed reference frame after a control input is given and the kite deforms. *adapted from:* [16]

Angle of attack

The angle of attack is usually defined as the angle between the incoming undisturbed flow direction and the line that goes through the leading and the trailing edge as shown in figure 4.6
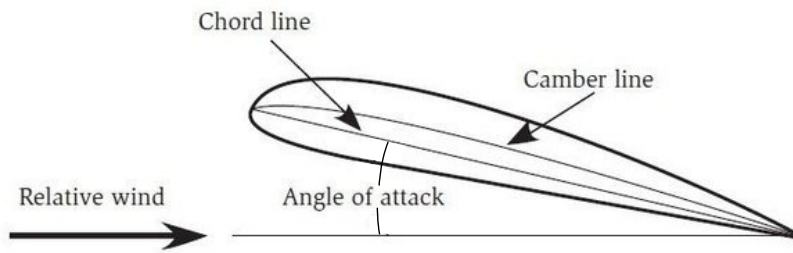
Figure 4.6: The definition of the angle of attack for airfoils.

In order to determine the influence of the angle of attack on the (steering) forces, measurement devices have been placed on the tips of the kite and on the measuring boom as shown in chapter 3 and in more detail in figure 4.7. This figure shows that there is an offset between the normally defined real angle of attack and the angle that is being measured, at least for the measurement in the center of the kite. On the sides it is different. Here the devices are attached directly to the fabric of the kite as shown in figure 4.8 which creates an uncertainty in the measurement for the angles. The fabric can deform to obtain different camber lines which would change the angle of the measured device to become erronous. The measurements for the local roll and local yaw however are more precise since the fabric will not be able to deform in a shearing manner as easily as for the camber shape.
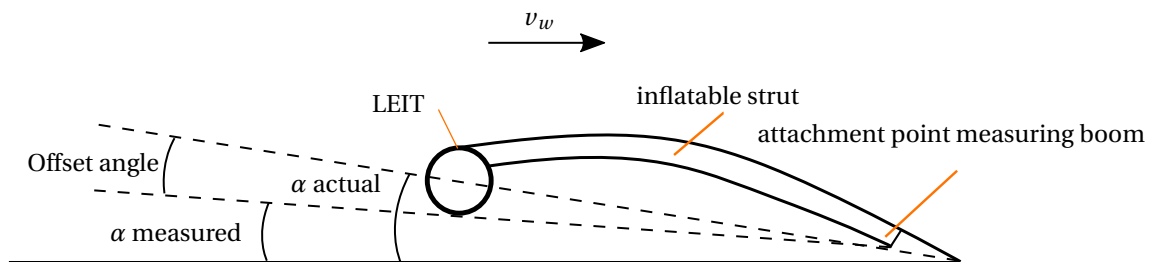
Figure 4.7: The definition of the angle of attack for a kite and the offset the measuring boom has with that angle.
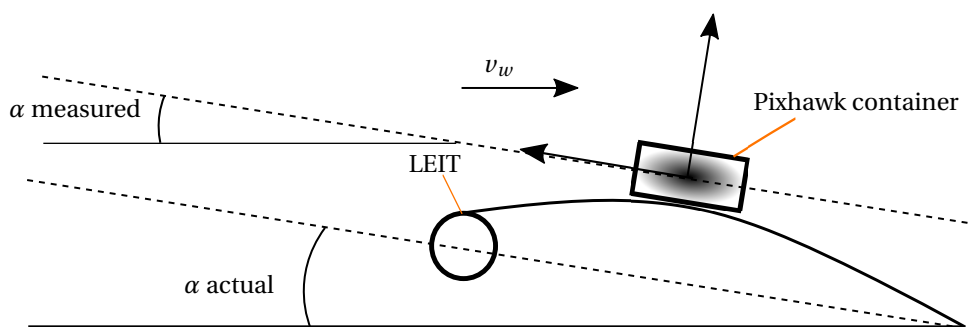
Figure 4.8: The angle measuring devices at the left and right tips of the kite are attached directly to the fabric. This however creates an uncertainty in the measurement since the fabric is free to move and deform. It is assumed however that the aerodynamic pressure forces are big enough to force fabric and therefore the pixhawk containers in their natural positions. The angle of the measuring device here seems to be in line with the actual angle of attack but this is not guaranteed.

In the end the uncertainty for the absolute angles at the sides results in only utilizing differences in measured angles. So for example the local earth fixed pitch angles are measured and during a maneuver these values change from +10 to -20 degrees. Then the information taken from that is a 30 degree change in angle,

and not the fact that it starts at +10 or ends at -20.

IMU vs windvane

Since the windvane is in front of the kite the vorticity produced by the kite will induce an extra velocity upwards that will affect the flow direction at the location of the windvane. The magnitude of this induced velocity is dependent on the distance to the kite, the flow velocity, the density of the air, and the amount of lift the kite produces. For the two dimensional case the relation between the vorticity and the local lift is given by Kutta-Joukowski theorem:

$$L'(y) = -\rho_\infty v_\infty \Gamma(y), \tag{4.11}$$

where $L'(x)$ is the lift of an infinitessimally small piece of kite, ρ_∞ is the freestream density of the flow, v_∞ is the flow velocity, and Γ is the local vorticity produced by this infinitessimaly small piece of kite. Then for the whole kite the lift force existing at the kite can be described by:

$$L = -\rho_\infty v_\infty \int_{-b/2}^{b/2} \Gamma(y) dy, \tag{4.12}$$

with b the span of the kite. Now to simplify things it is assumed that the wake of the kite has an influence that is significantly smaller than the kite itself and is therefore neglected, it is also assumed that the path of the vorticity can be described as a straight path at the height of the windvane and the distribution of lift has a circular distribution. In order for this distribution to be equal the vorticity will have the function:

$$\Gamma(y) = \frac{\sqrt{((b/2)^2 - y^2)}}{b/2} \Gamma_0, \tag{4.13}$$

where Γ_0 is a term that relates this function to the total amount of vorticity present at the kite in order for it to produce the right amount of lift. To find this value we fill in the function for the vorticity of equation 4.13 into equation 4.12 to find:

$$L = -\rho_\infty v_\infty \int_{-b/2}^{b/2} \frac{\sqrt{((b/2)^2 - y^2.)}}{b/2} \Gamma_0 dy. \tag{4.14}$$

Since a circular distribution is used the integral of this function will have the value of half a circle, $\frac{1}{2}\pi r^2$. This allows us to rewrite equation 4.14 into:

$$L = -\rho_\infty v_\infty \Gamma_0 \frac{1}{2}\pi \left(\frac{b}{2}\right)^2. \tag{4.15}$$

The value for Γ_0 is found by:

$$\Gamma_0 = \frac{L}{-\rho_\infty v_\infty \frac{1}{2}\pi \left(\frac{b}{2}\right)^2}, \tag{4.16}$$

which can be filled in into equation 4.13 to find a fully known function for the vorticity in the 3D space. The next step now is to calculate the influence this vorticity has on the flow direction at the location of the windvane. From Munk[26] it is found that the downwash of a finite piece of vorticity on the flow direction at a certain other point can be defined as:

$$dw = \frac{1}{4\pi \rho_\infty v_\infty} \frac{\xi - x}{r^3} \Gamma(x, y, z), dy \tag{4.17}$$

with:

$$r^2 = (\xi - x)^2 + (\eta - y)^2 + (\zeta - z)^2, \tag{4.18}$$

where (ξ, η, ζ) is the location where the downwash is calculated, and dw is the contribution to the downwash from the vorticity at point (x, y, z). All the variables in equation 4.17 are known. The situation is shown in figure 4.9.
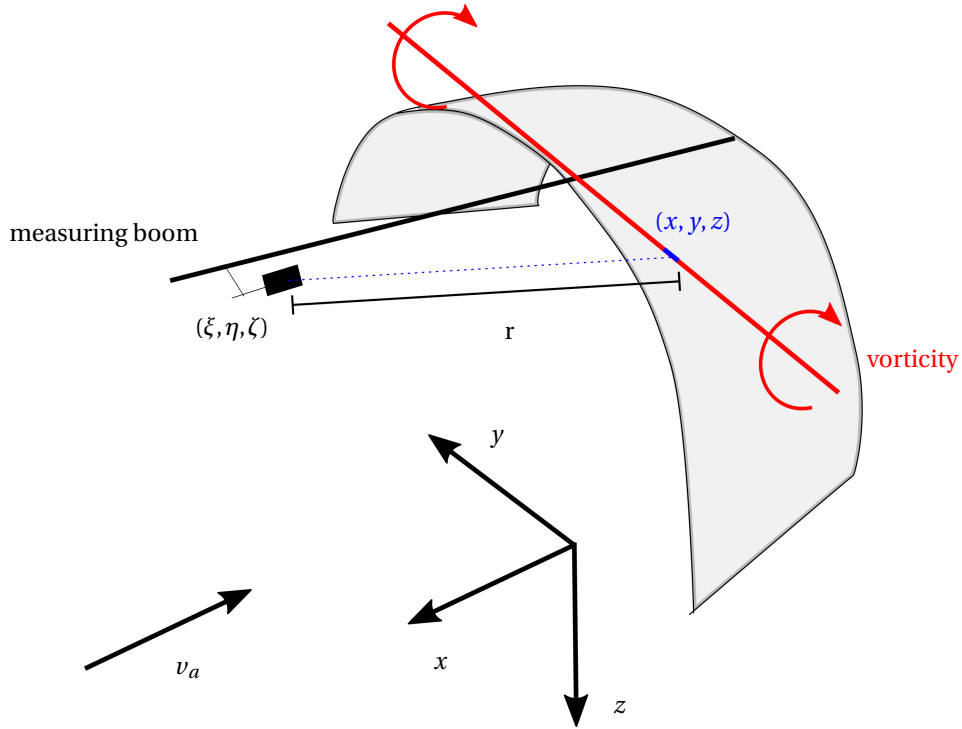
Figure 4.9: The vorticity that the kite creates is modeled as a straight line. Then the downwash at a certain point (ξ, η, ζ) of the entire line can be calculated by taking the value of the blue part and using equation 4.17 and integrating over the entire vorticity line.

To find the influence of the entire line equation 4.17 is simply integrated over the entire path of the vorticity, thus the red line shown in figure 4.9 to find:

$$w = \int_{-b/2}^{b/2} \frac{1}{4\pi\rho_\infty v_\infty} \frac{\xi - x}{r^3} \Gamma(x, y, z) \mathrm{d}y. \tag{4.19}$$

So it is found that when the lift force, apparent flow velocity and the density are known together with the geometry of the kite it should be possible to account to a certain degree for the offset in flow angle at a given location.

To implement this model into the data some assumptions need to be made since not the exact parameters are being measured. First the lift force L is assumed to be equal to the combined tether forces:

$$L \sim F_T. \tag{4.20}$$

The free stream velocity V_∞ is assumed to be equal to the measured apparent flow speed V_a, There might be a slight offset in this value due to the angle of attack but it is neglected here. It is also assumed that the vorticity follows a circular distribution along the kite which simplifies the integration of the function considerably. The vorticity in the wake that is a function of the derivative of the vorticity on the kite is neglected. This is done since the wake is farther away from the windvane and the values of the derivative of a convex function with homogeneous boundary conditions will be significantly smaller than the original function. And the last assumption is that the path of the vorticity is a straight line tangent to the kite canopy at the center of the kite. This is in fact physically impossible but here it is assumed that it will not affect the correctional term too much.

The final induced velocity will be calculated computationally thus the integral in equation 4.19 is implemented as a collection of constant vortex filaments of length l_i:

$$w(t) = \frac{1}{4\pi\rho_\infty(t)v_\infty(t)}(\xi - x)\sum_{i=1}^{N}\left(\frac{\Gamma_i(t)}{r_i^3}l_i\right), \tag{4.21}$$

with Γ_i:

$$\Gamma_i(t) = \Gamma_0(t) \frac{\sqrt{((b/2)^2 - y_i^2)}}{b/2}, \tag{4.22}$$

and r_i^2 (notice the difference in component):

$$r_i^2 = (\xi - x)^2 + (\eta - y_i)^2 + (0)^2. \tag{4.23}$$

Here $\xi - x$ is constant and defined by the location of the windvane and $\zeta - z = 0$ due to the definition of the path and location of the modeled vorticity. The value of y_i is defined in the center of every discretized piece of path of vorticity.

Figures 4.10a and 4.10b show the calculated distribution of vorticity and the corresponding downwash effect that vorticity has on the windvane that is placed 0.5 m in front of the kite.

(a) The vorticity distribution over the modeled vorticity line

(b) The downwash induced over the modeled vorticity line per length of vorticity.
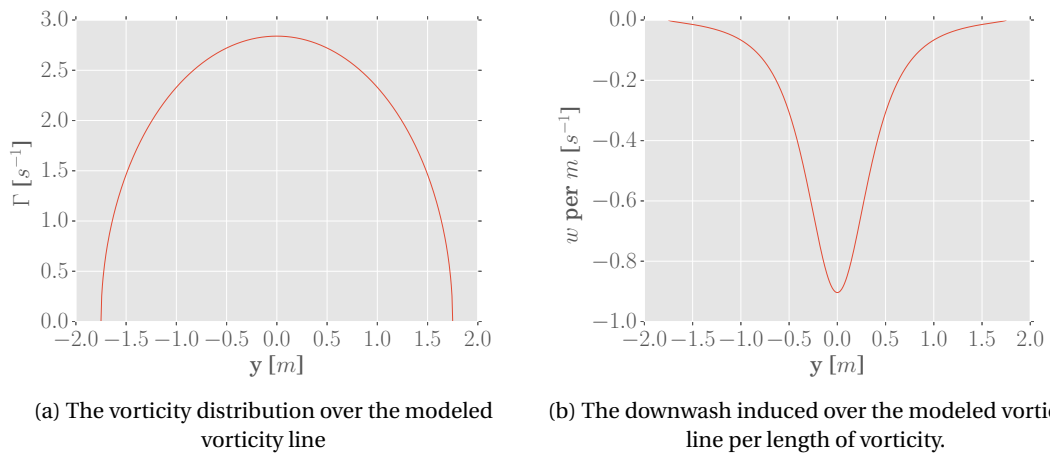
Figure 4.10: The vorticity and downwash are calculated for a kite that creates 800 N liftforce in a flowfield moving at 12 ms^{-1} with a density of 1.22 kgm^{-3}.

Sideslip angle

For the sideslip angle measured by the windvane there is a comparable problem. When the kite is rotating the offset from the axis of rotation that the windvanes are located on creates an extra induced velocity that is not experienced by the kite as a whole. Figure 4.11 shows how a rotation adds a velocity component to the sideslip windvane during steering. This velocity can be calulated by:

$$\vec{v}_{\dot{\gamma}} = \dot{\gamma} \cdot \Delta x, \tag{4.24}$$

where $\vec{v}_{\dot{\gamma}}$ is the induced velocity at the location of the sideslip windvane in $m \cdot s^{-1}$, $\dot{\gamma}$ the kite yaw rate in $rad \cdot s^{-1}$, and Δx the offset of the windvane relative to the yawing axis in m.

In order to account for the error caused by this rotation the angle can be calculated using the measured value for the yaw rate in the kite frame and the apparent wind velocity. As figure 4.12 shows how the velocities create an angle that can be calculated by:

$$\beta_{\dot{\gamma}} = \arctan\left(\frac{\vec{v}_{\dot{\gamma}}}{\vec{V}_a}\right). \tag{4.25}$$

So this angle needs to be subtracted from the measured sideslip angle to find the sideslip angle that is present at the kite itself.
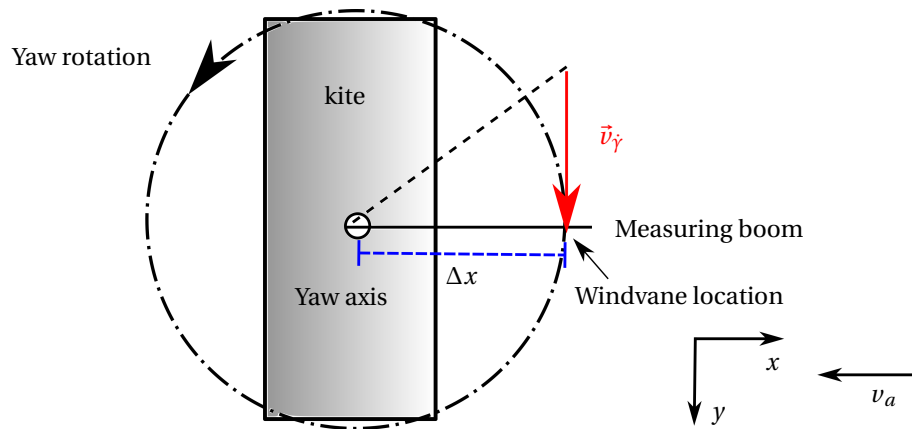
Figure 4.11: Top view of the kite that rotates counter clockwise during a steering maneuver. This induces an additional velocity component at the location of the windvane that measures the sideslip that is not actually present at the location of the kite itself.
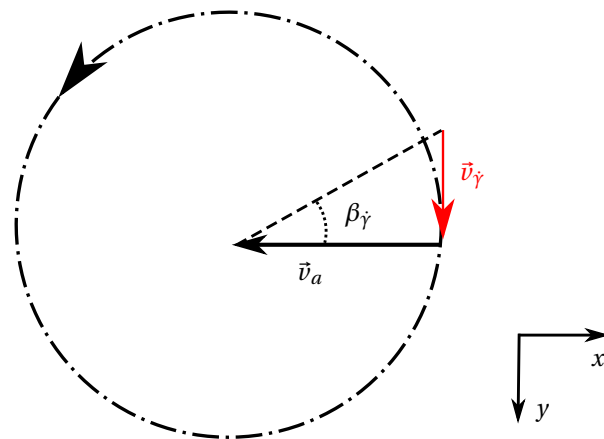
Figure 4.12: The rotation of the kite creates an added angle measured by the sideslip windvane shown here as $\beta_{\dot{\gamma}}$.

Mass moment of inertia

In order to get a quantative estimation of the forces that drive the yawing acceleration first the mass moment of inertia has to be determined. The mass moment of inertia is the resistance of an object to changes in rotational speed about a specific axis. This means that the larger the moment of inertia is the harder it is to change its rotational velocity.

The manner in which the relationship between the moment, mass moment of inertia and the rotational acceleration holds is given as:

$$\text{mass moment of inertia} = \frac{\text{torque}}{\text{rotational acceleration}} \tag{4.26}$$

This means that for the yawing axis we find the relation:

$$I_\gamma = \frac{M}{\ddot{\gamma}}, \tag{4.27}$$

here I_γ is the mass moment of inertia around the yawing axis, M is the applied moment around the yawing axis, and $\ddot{\gamma}$ is the rotational acceleration around the yawing axis. This means that when the acceleration and the mass moment of inertia is known, the moment around the given axis can be computed. In order to find the mass moment of inertia of an object several approaches can be used. The first one would be to calculate it by means of equation 4.28 given in [18] p.545

$$I = \int_V r^2 \rho \, dV, \tag{4.28}$$

with I the moment of inertia around the considered axis, V the volume of a given object, r the distance between two points being considered, and ρ the density. However the shape of the kite during flight is very complicated and the distribution throughout the shape is not homogeneous. Instead of numerically estimating the moment of inertia it is also possible to do so experimentally by the bifilar pendulum method [23].

As seen in figure 4.13 the bifilar pendulum method hangs an object to two straight lines. The given mass, geometry of the setup, and period of the pendulum movement determine the mass moment of inertia. In [23] the equation that finds the mass moment of inertia is then given as:

$$I = \frac{mgT^2}{4\pi^2} \frac{b_1 b_2}{\sqrt{\left(S^2 - (b_2 - b_1)^2\right)}}, \tag{4.29}$$

here I is the moment of inertia around a given axis, m is the mass of the system, g is the gravitational acceleration, T is the period of the oscillation, b_1 and b_2 are the lengths between the points of suspension and where the strings are attached to the object respectively, and S is the length of the two lines. Now since we design the experiment in such a way that the lines hang vertically we have that $b_1 = b_2$, which allows the equation to be simplified to:

$$I = \frac{mgT^2 b_p^2}{4\pi^2 S}. \tag{4.30}$$

Thus from the geometry of the test setup the moment of inertia of the kite with the measurement tools on it can be determined.

The test was performed in the cyberzoo of the Delft University of Technology. Figure 4.13 shows the setup as it was carried out. In the figure the lengths of the pendulum are shown. For the variable S the length of the line to the attachment point at the bridles is taken to be the pendulum line length. This means that it is assumed that the bridles in combination with the kite will behave as a single solid object. The argument here is that the different attachment points of the bridle on the kite form a tensioned equilibrium and the small rotations that happen during the experiment are not enough to significantly distort this equilibruim.
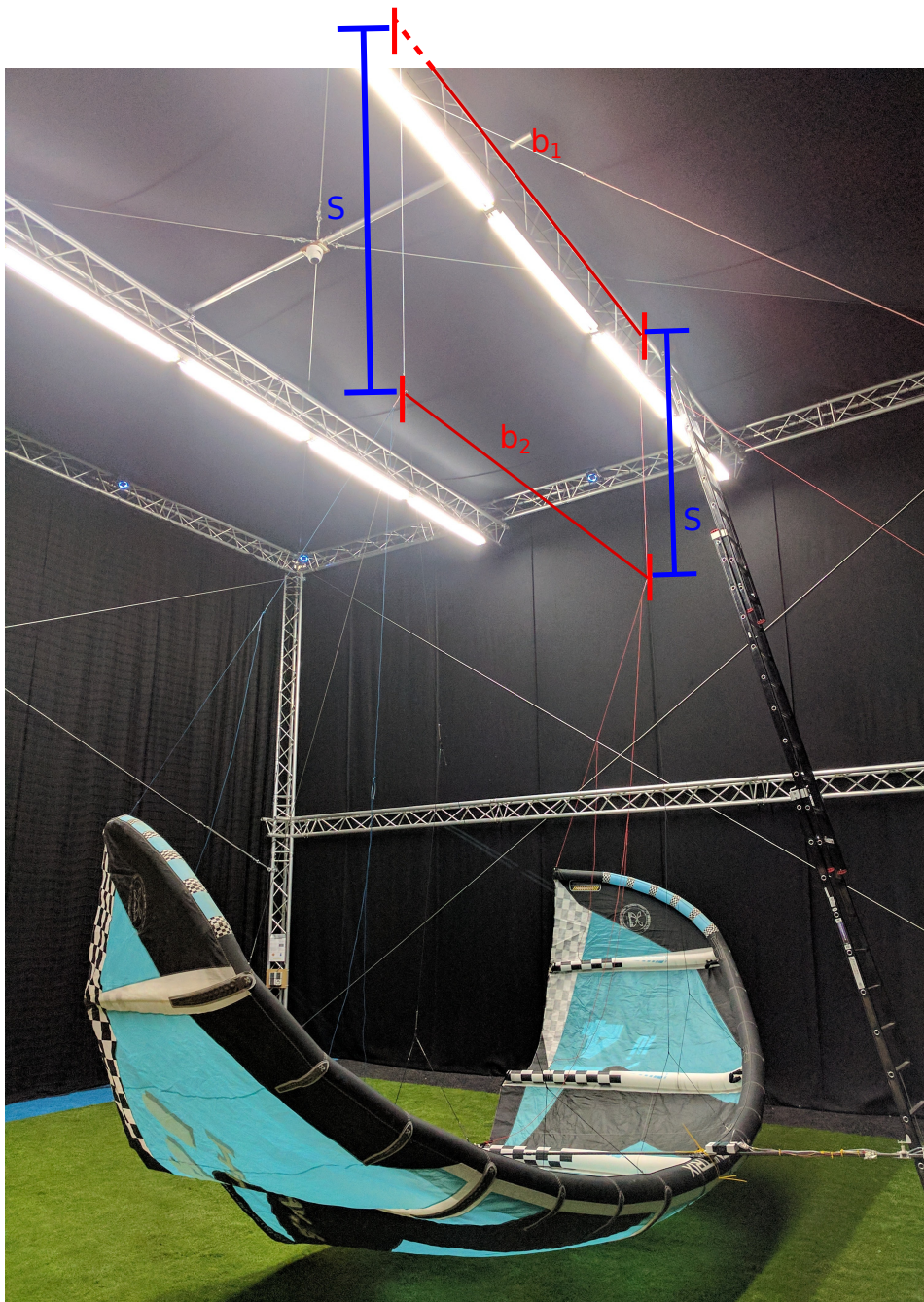
Figure 4.13: The test setup of the bifilar pendulum which can determine the mass moment of inertia of the kite system with added experimental objects. Here b_1 and b_2 are of equal length, as is the length of the two strings S.

The several parameters that are needed to determine the mass moment of inertia the values are given in table 4.1. Using the tracking mechanism that was already available in the cyberzoo the period of the oscillation can be found. The tracking system of the cyberzoo works with several cameras that track reflective tags that can be placed on any kind of object. Using the relative locations of the cameras and the tags a location in the three dimensional space can be determined up to 1 mm accuracy. [28] figure 4.14 shows where the tags were placed.

Now in order to determine the period of the oscillation that is caused by a minor initial rotational offset in the system the X-coordinate of the tip of the stinger is taken as the tag that shows the oscillation the most clear since it has the largest distance to the center of rotation.

Table 4.1: Bifilar pendulum test setup variable values.

Variable name	Value
hangoff width b_1, b_2	2.3 $[m]$
gravitational acceleration g	9.81 $[ms^{-1}]$
hangoff length S	2.3 $[m]$
Mass M	6.8 $[kg]$
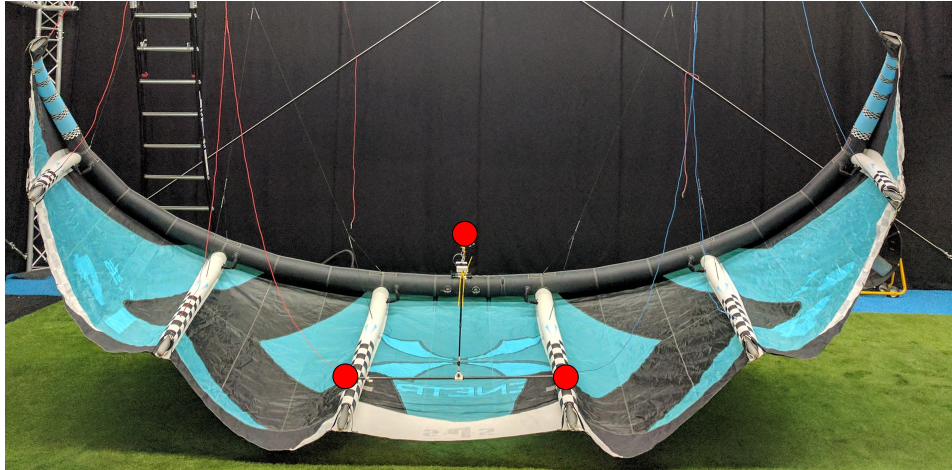
Figure 4.14: The backview of the kite during the bifilar pendulum experiment. The three red dots show where the tags were placed on the system. The red dot at the end of the stinger is the one that is later used to determine the period of the oscillation.
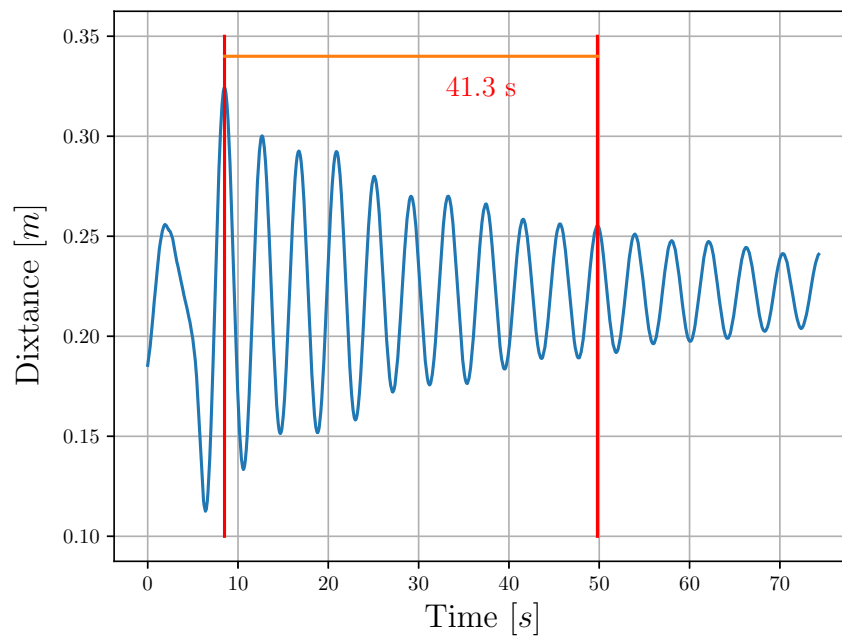
Figure 4.15: The movement of the tag at the tip of the stinger during the bifilar pendulum experiment. Here it is shown that 10 periods take a time of 41.3 seconds which makes a single period take 4.13 seconds.

Figure 4.15 shows a measurement where ten periods take 41.3 seconds, thus the period of the oscillation is 4.13 s. The values from table 4.1 and the measured period are inserted into equation 4.30 to find:

$$I = \frac{7kg \cdot 9.81 m \cdot s^{-2} \cdot 2.3^2 s^2 \cdot 4.13^2 m^2}{4\pi \cdot 2.3 m} = 17 kg m^2. \tag{4.31}$$

<div align="right">

5

</div>

Turn rate law

The overall steering of kites has been shown to follow a turn rate law [12]. It relates the yaw rate $\dot{\gamma}$ to the steering input δ and apparent wind velocity v_a as:

$$\dot{\gamma} = G\delta v_a \tag{5.1}$$

Where G kite specific constant value to be determined experimentally.

To determine if the test setup is suitable to measure the precise behaviour of the kite first it has to be established the turn rate law follows from the current sensor system. Oehler [27] tested with the Kitepower team in march 2017 his sensor system which utilizes the same collection of systems as the current setup. This is therefore an ideal test to see if a full scale test yields this result.

During the test however there were no figures of eight as are usually desirable for power producing kite systems. Figure 5.1 shows one of the reel out maneuvers for a given power cycle.
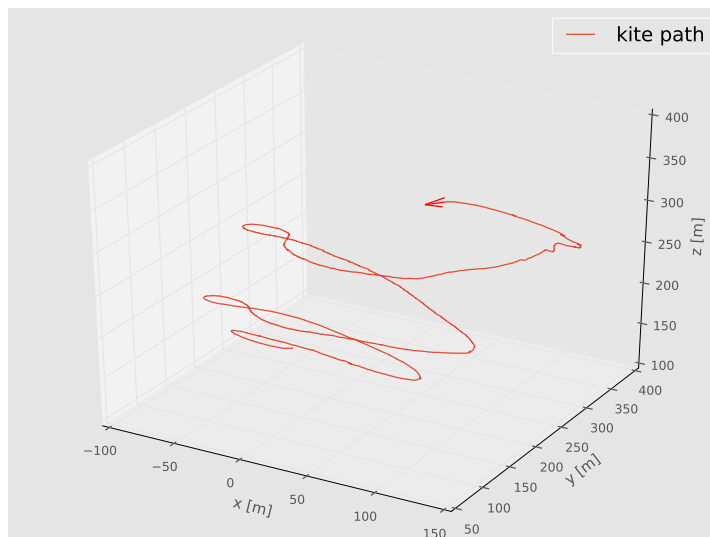
Figure 5.1: The kitepath of one of the reel out maneuvers of one power cylce during the test that was done by Oehler[27]

To get a first idea if the presented data shows any promise on delivering the desired results the turn rate $\dot{\gamma}$ is plotted against the product of the steering input times the apparant wind velocity $\delta \cdot v_a$. This is then compared to the result shown in [12]. The comparison is shown in figure 5.2. The data shown in figure 5.2a shows the values of every instantaneous point in time.

Figure 5.2 shows that the Kitepower steering system also shows a linear behaviour when compared to the steering input times the apparent wind velocity. Now in order to determine the value of the single constant that relates the two we rewrite equation 5.1 to find the constant G as follows:

(a) The Turn rate $\dot{\gamma}$ for values of the steering input times the velocity measured during the test at Valkenburg done by Oehler together with Kitepower [27]

(b) The Turn rate $\dot{\gamma}$ ($\dot{\psi}_m$ in the figure) for values of the steering input times the velocity measured during bang-bang flight performed by Skysails [12]
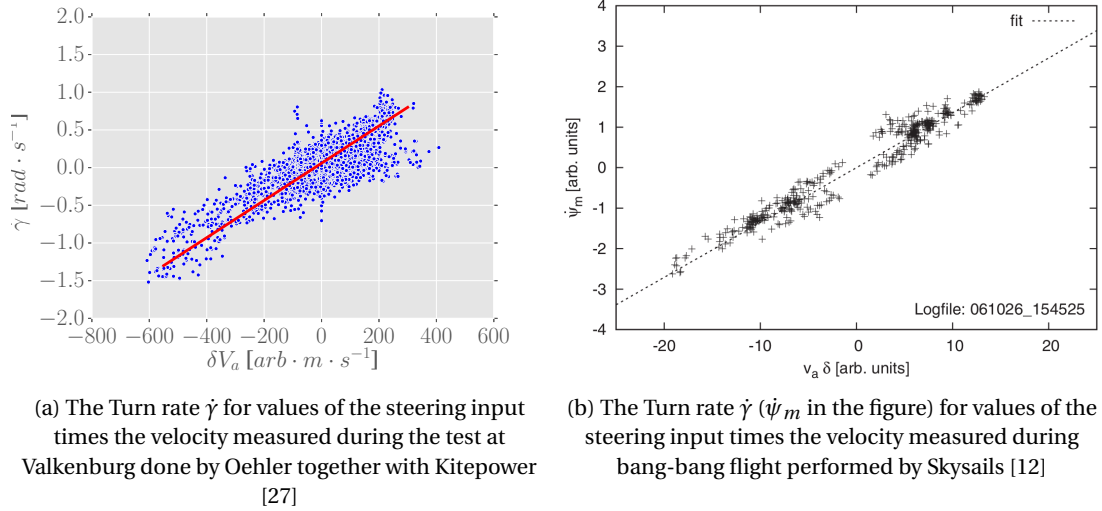
Figure 5.2: A comparison between the data obtained during a testflight in March 2017 by Kitepower and data obtained by Skysails in 2006

$$G = \frac{\dot{\gamma}}{\delta v_a} \qquad (5.2)$$

To find the value for G a distribution of values is plotted where one should be able to determine the value for G. In order to do this all values found for G are rounded to their closest integer and then the amount of occurences of each available integer within the dataset is plotted against their rounded value. Figure 5.3 shows the distribution cut off at -2000 and + 2500 for values of G.
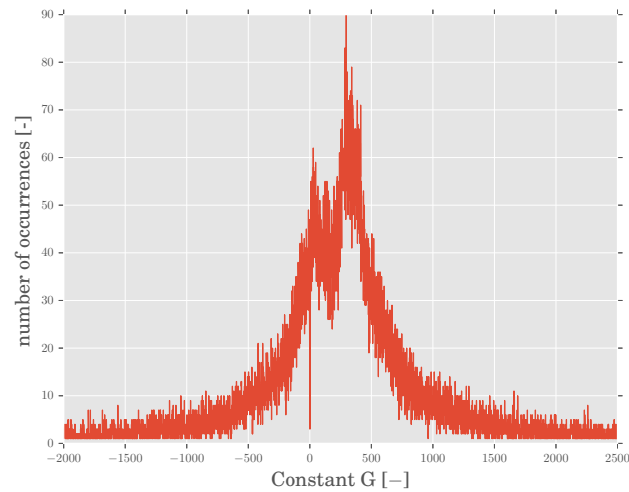
Figure 5.3: The distribution of the amount of occurences of values found for G during the flighttest at Valkenburg performed by Kitepower in March 2017.

Figure 5.3 clearly does not show a simple normal distribution as was expected. it more seems to be a bimodal distribution with two distinct peaks. However this can be explained by the fact that this shows the steering relation for the whole flight test, not specific parts. The idea is that this coefficient changes during certain parts of the test. For example the steering during the reel-in phase will be less effective than the steering during the reel-out phase, leading to different values of this coefficient G.

After isolating both the reel-out phase as the reel-in phase by checking if the derivative of the tether length

was positive or negative a significanty different distribution of *G* is obtained. Figures 5.4 and 5.5 show the distribution of *G* for these specific parts of the test where two classical normal distributions are seen.
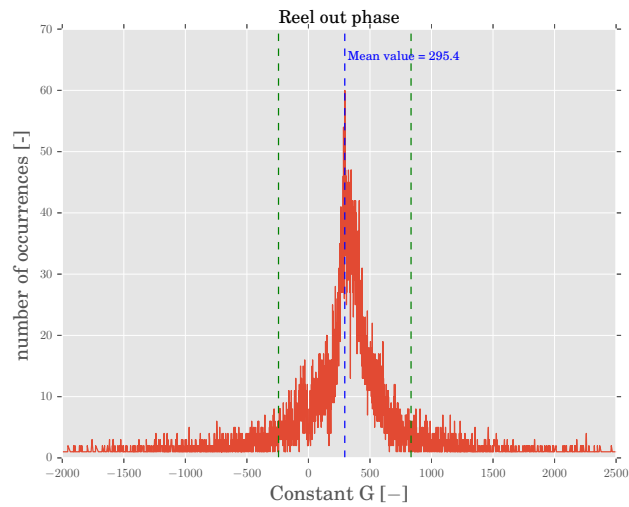
Figure 5.4: The distribution of the amount of occurences of values found for *G* during the reel out phase of the flighttest at Valkenburg performed by Kitepower in March 2017.
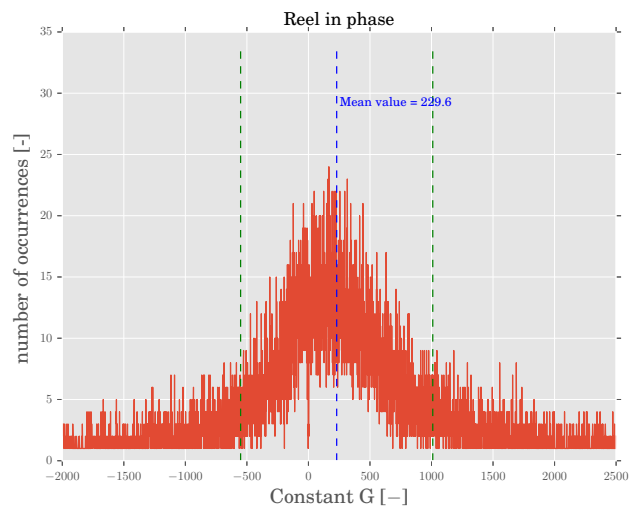
Figure 5.5: The distribution of the amount of occurences of values found for *G* during the reel in phase of the flighttest at Valkenburg performed by Kitepower in March 2017.

Figure 5.4 showing the distribution of values for *G* during the reel out phase shows that the coefficient on the one hand is higher, meaning that any given steering input during the reel out phase (thus flying faster and with a higher power setting) will result in a greater turn rate than during reel in shown in figure 5.5 making it essential for the experiments that different power settings are treated seperately. Also the standard deviation of the higher power setting is smaller which leads to the idea that a higher power setting constrains the kite more defining the steering properties more effectively however this is not conclusive.

6

Results

The results of the experiments are shown and discussed in this chapter. Up to 17 attempts were made to get the test setup to provide all the essential measurement data. After a succesfull test the C_R values were found but the steering by the pilot was found to be too inconsistent. Then an added feature in the test setup that restricted the amount of steering that was possible by the pilot yielded a final test from which the turning data is presented.

Angle of attack

An important means of measuring the performance and being able to control the behaviour of a kite is knowing what the aerodynamic forces are based on the inflow angles. The inflow angles are defined as the angle of attack α and the side slip angle β. This section will show how these parameters behave for different power settings.

Wind vane versus IMU

On the kite there are two devices that measure the angle of the kite with respect to the incoming flow. There is a windvane that can rotate along an axis parallel to the pitch axis 0.5 m in front of the leading edge of the kite. And there is the Pixhawk that measures the orientation of the kite with respect to the gravitational acceleration it measures from gravity.

Figure 6.1 shows the measurements of the angle of the kite by means of the wind vane and the pixhawk orientation. There is a clear offset between the two values that increases as the power setting, and thus aerodynamic forces increase. This offset can be explained by modeling the kite as a single lifting line as envisioned by Prandtl. This line consists of a vorticity that allows the kite to produce lift forces. This is thoroughly explained in chapter 4.2.

Since the performance of a kite is measured by the inflow angle that is defined by the undisturbed flow this angle measured by the wind vane is clearly not the one that should be used. Therefore the assumption is made that the flow that the kite experiences during the test is a perfect horizontal one and that the pixhawk itself provides the correct angle of attack.

As is described in chapter 4.2 an attempt is made to correct for the offset created by the vorticity. Following the strategy presented figure 6.1 shows the original values measured by the two devices with an added signal that uses the correction (purple line). As is seen the corrected values are very close to the values measured by the pixhawk thus this method shows a lot of potential for providing the free stream angle of attack when the current method cannot be used. One can imagine a kite flying crosswind figures of 8 cannot rely on the assumption that the flow is a horizontal one combined with the kite velocity and will need a device that measures the angle of the incoming flow.
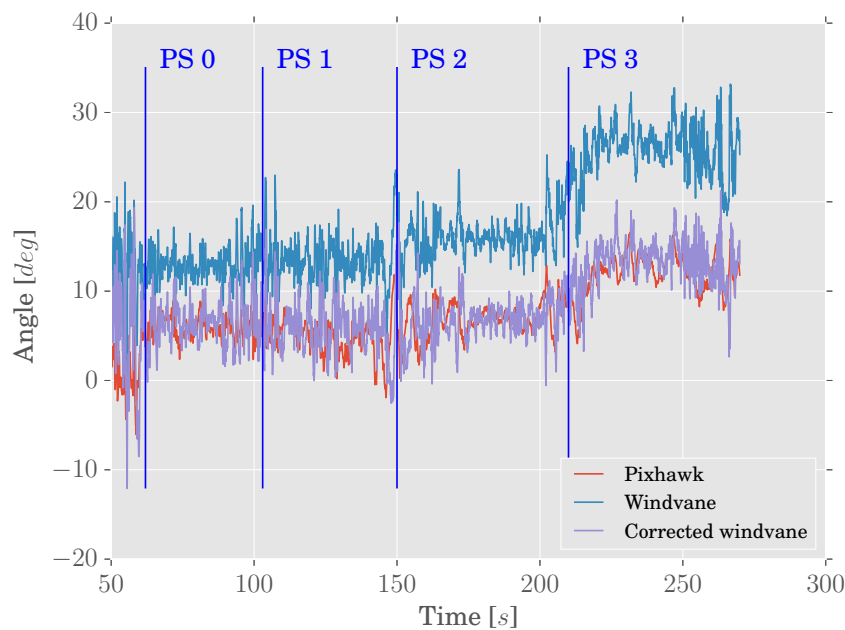
Figure 6.1: The angles measured by the windvane and pixhawk for different power settings together with the angles of the windvane that have been corrected using the simplified lifting line model presented in chapter 4.2, the power settings 0, 1, 2, and 3 begin at every shown vertical line.

Velocity and force data

The data that the pitot tube provided seemed to have a large fluctuating signal that was not expected from the weather forecast that day. The values ranged from 19-27 kts where in fact the report said it would be more in the order of 25-30 kts. In order to investigate this two seperate parameters are compared to each other. The tether forces and the velocity squared should follow the same pattern. From equation 6.1 it can be seen that the tether forces and the velocity squared should follow the same curve when the aerodynamic coefficient C_R, density ρ, and projected kite surface area A are constants. From these values the value of C_R will fluctuate a little due to the kite deforming under the influence of wind gusts.

$$F_T = C_R \frac{1}{2} \rho A \cdot v_a^2 \tag{6.1}$$

In order to compare them the following relationship needs to be found:

$$f\left(\frac{F_{\text{tether}}}{\overline{F}}\right) \sim f\left(\frac{V_a^2}{\overline{V}_a^2}\right) \tag{6.2}$$

Figure 6.2 shows how the normalised velocity squared and the normalised tether forces squared are measured during an arbitrary time period of the test. It shows that both parameters follow the same trends. The offsets at certain points can be explained by differences in C_R at that point in time by a change in angle of attack or power setting. The trend however is very similar and it can be concluded that both parameters are measured correctly.
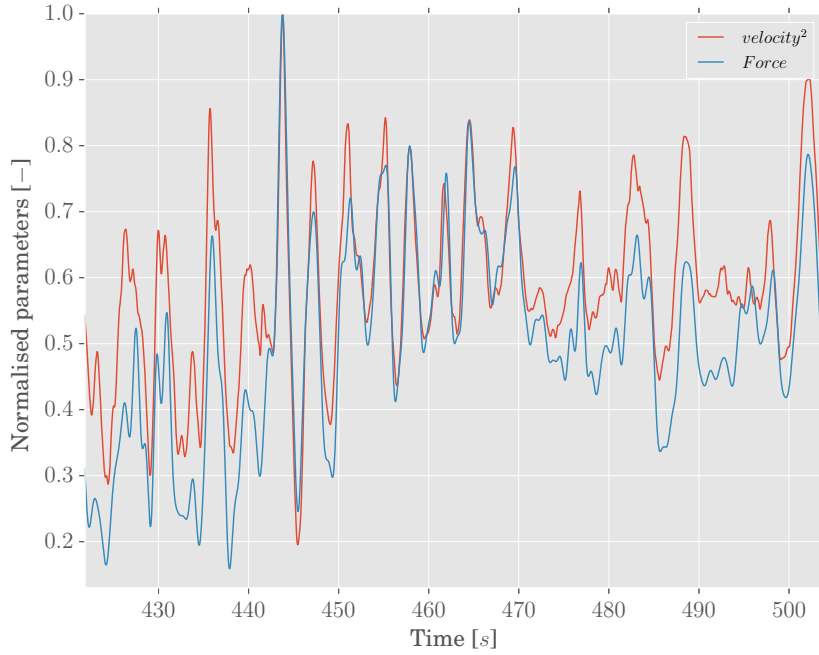
Figure 6.2: The normalised velocity squared V_a^2 compared to the normalised tether forces over an arbitrary period of time during the test.

Aerodynamic coefficients

The results for C_R as a function of the middle angle of attack α of the static test where the power ratio was set to be four distinct values for one minute each are given in figure 6.3.

Figure 6.3 shows how the aerodynamic forces evolve with different power settings and how the angle of attack changes accordingly. The colored clouds are density plots for the different power settings. The power settings are from lowest to highest: red, green, blue, black. The mean value shown is found by rounding all the values for a given angle of attack from all the different power settings. These values are collected into one array and the average of these values is taken as the mean for every angle of attack.

$$\mu(\alpha) = \frac{\sum\limits_{i=1}^{N} C_{r,i}}{N} \qquad \text{for} \quad \text{round}(\alpha_i) == \alpha \tag{6.3}$$

$$\sigma(\alpha) = \sqrt{\left(\frac{1}{N}\sum_{i=1}^{N}\left(C_{r,i} - \mu(\alpha)\right)^2\right)} \tag{6.4}$$

Where $\mu(\alpha)$ is the mean for every value of the angle of attack α, $C_{r,i}$ and α_i are corresponding values for the aerodynamic coefficient and the angle of attack, N is the amount of datapoints within the set for every α, and $\sigma(\alpha)$ is the standard deviation for every collection of values of C_R. To verify these results figure 6.4 shows the values found by Python [30]. The different power settings are defined differently but the overall behaviour of the C_R can be seen to correspond to the values found here.

A few results stand out about how the system behaves. First of all the change in angle of attack from the lowest power setting to the second lowest is unexpected. Usually in aerodynamics a higher angle of attack corresponds to higher lift and mostly drag forces. In this case the angle of attack goes down whilst the forces go up. In order to explain this behaviour here the absolute pitch and roll angles at the sides are shown in figures 6.5b to 6.6b.
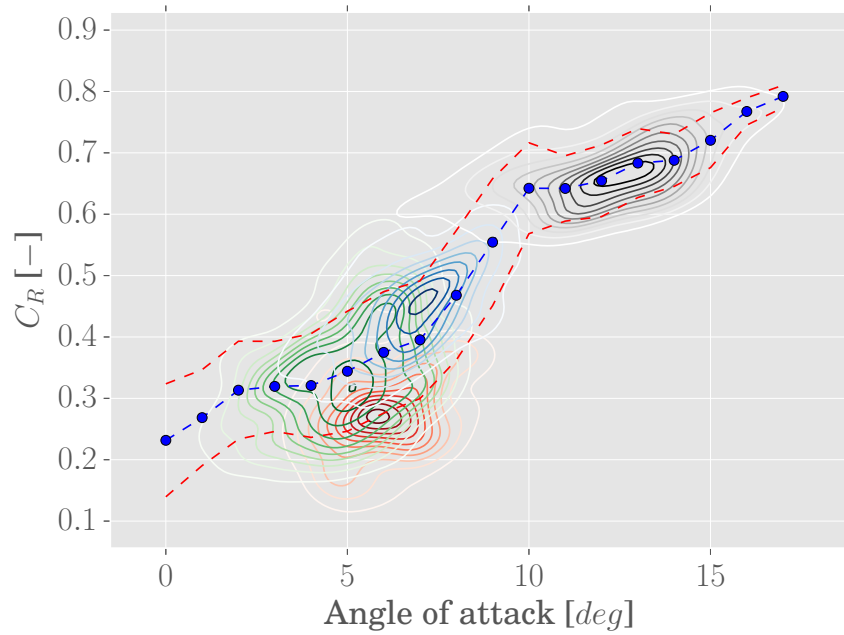
Figure 6.3: The aerodynamic coefficient C_R for different power settings plotted against the angle of attack. The power settings are from low to high: red, green, blue, black. The blue line represents the mean of the found values for the C_R for every angle of attack and the red lines represent the standard deviation for every value of C_R at that angle of attack.
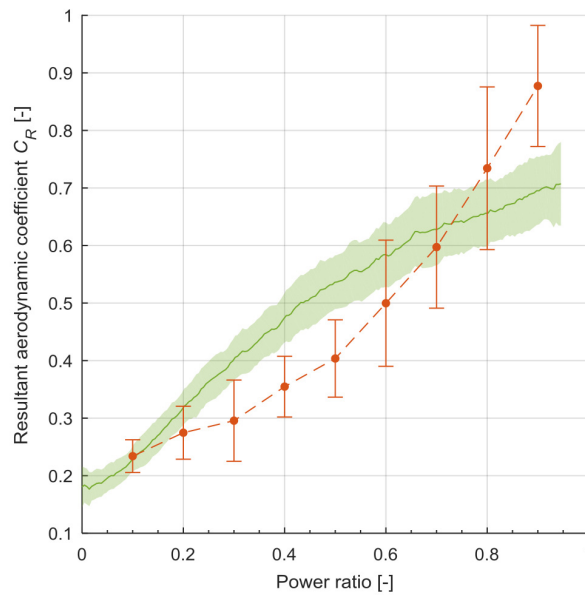
Figure 6.4: The aerodynamic coefficient C_R versus power setting as it was determined by Python [30]. The red line is the data found for static flight where the kite was in equilibrium and therefore the one to compare to the data found in this study.

From the angles at the sides a better understanding of the unexpected behaviour for the angle of attack at the middle of the kite is shown. The absolute pitch angles for example do not go down and from the right side in figure 6.5b it seems that the angle goes up. This together with the fact that the roll angles roll up around ± 5 degrees shows that the kite unfolds as shown in figure 6.7. This in effect creates a larger surface that is able to produce effective lift forces which contribute most to the value of C_R. So the kite over the span deforms where the pitch angles at the sides slightly increase but the kite obtains a larger projected surface area which allows for the kite to increase the aerodynamic coefficient.
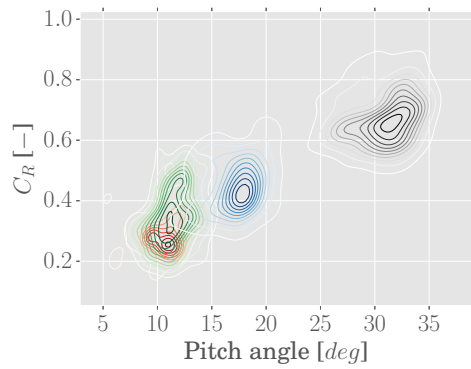
(a) Left side of the kite.   (b) Right side of the kite.
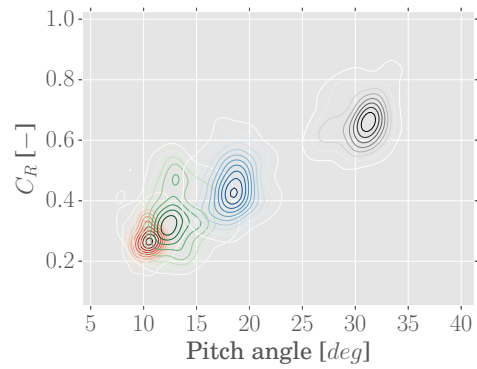
Figure 6.5: The absolute local earth reference frame pitch angles at the sides of the kite during different power settings, a ±90 degrees angle corresponds to perfectly vertical endpoint of the kite. Power setting going from low to high: red, green, blue, black.
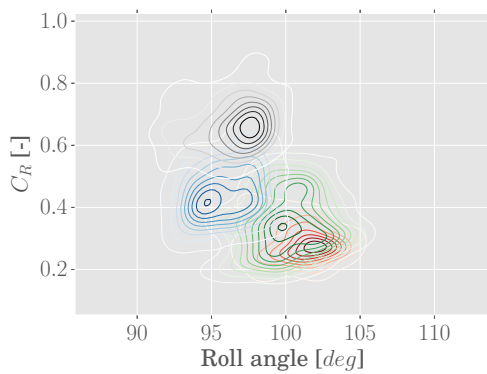
(a) Left tip of the kite.   (b) Right tip of the kite.
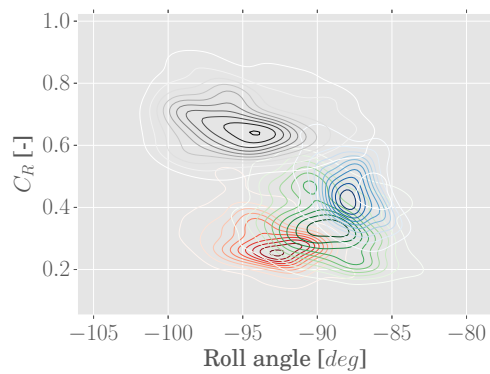
Figure 6.6: The absolute local earth reference frame roll angles at the sides of the kite during different power settings. Power setting going from low to high: red, green, blue, black.
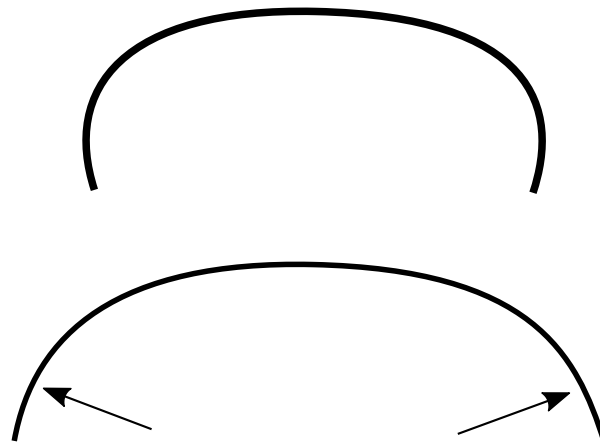
Figure 6.7: During the powering up between the lower power settings the kite unrolls providing a larger surface area to effectively produce lift. (exaggerated for clarity)

The rest of the $C_R-\alpha$ curve shown in figure 6.3 follows a trend as one would expect from an airfoil changing angle of attack and increasing the lift and drag forces. Another phenomenon can be distinguished however.

The difference between the angles at the sides and the angle in the middle of the kite is large. The angles at the sides move from ± 12 to ± 32 degrees while the angle in the center changes from ± 5 to ± 13 degrees. This means that at the sides the angles increase by ± 20 degrees while in the center the change is limited to ± 8 degrees. The change in the performance of the kite can therefore not be linked to the change in angle of attack that is seen in the center. What this data shows however is that the kite deforms spanwise, where the absolute angle of attack at the sides increases more than twice as much than at the center.

An explanation for this specific behaviour can be found in the bridle setup of the Hydra. The power lines that are attached to the leading edge of the kite do not go all the way to the tips of the kite. The last attachment point of the powe lines is at the second most outer strut. This leaves a section of the kite to attain a much higher angle of attack since the leading edge at that point is not fixed to stay a certain distance from the center point on the ground. Now an aerodynamic moment will find an equilibrium position at a much higher angle of attack than at the center where the power lines are attached. This behaviour can therefore not be linked to C-shaped kites per se as other bridle sets might prohibit this large increase in angle of attack.

To further show that this is in fact the case figure 6.8 shows the ratio between power and steering line forces for the different power settings. This ratio is calculated by means of dividing the power line forces over the total amount of force as shown in equation 6.5.

$$PR = \frac{F_{\text{power}}}{F_{\text{power}} + F_{\text{steering}}} \tag{6.5}$$

Where PR is the non dimensional power ratio, F_{power} is the force on the power lines, and F_{steering} is the force on the steering lines. It can be seen that for higher power settings the ratio decreases meaning that more and more of the force is going through the steering lines. When looking at the bridle setup this must mean that bigger amounts of aerodynamic force are generated at the tips. Which is in line with the significantly higher angles of attack that are measured there.
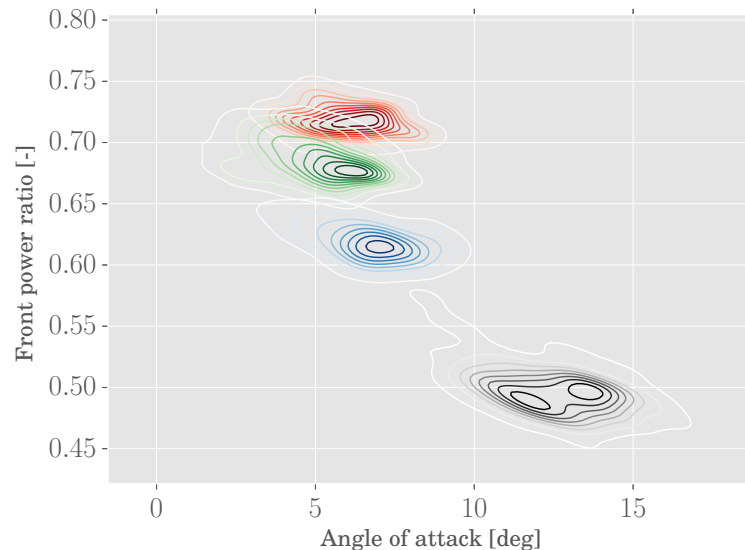
Figure 6.8: Power ratio between power and steering lines, from low to high power setting: red, green, blue, black. During the powering up there is a shift in the force distribution over the kite. The steering lines carry relatively more loading for the higher power settings, a the highest power setting an equal amount of force goes through the steering lines as through the power lines.

Steering rates

The steering rates of the kite are according to literature dependent on the turn rate law[11]. To see if the test also shows this law to hold true the constant steering maneuvers carried out are analysed.

Yaw rates

The first parameter to find is the yaw rate itself. During this dynamic maneuver this is not trivial. The movement itself consists of a starting point: the moment the pilot applies the steering input. An initialization period: the transition from steady flight into the constant turning maneuver. The steering period: the time where the kite finds an equilibrium situation which a constant yaw rate is found based on newly deformed kite. And finally the point where the pilot believed the kite needed to steer back unto a path in order for it not to crash on the ground. We call these moments I, II, III, and IV. Figure 6.9 shows the yaw rate for a single yawing maneuver including the discussed moments . The first line is the start of the steering input and every other line indicates the end of one of the described periods II, III, or IV.
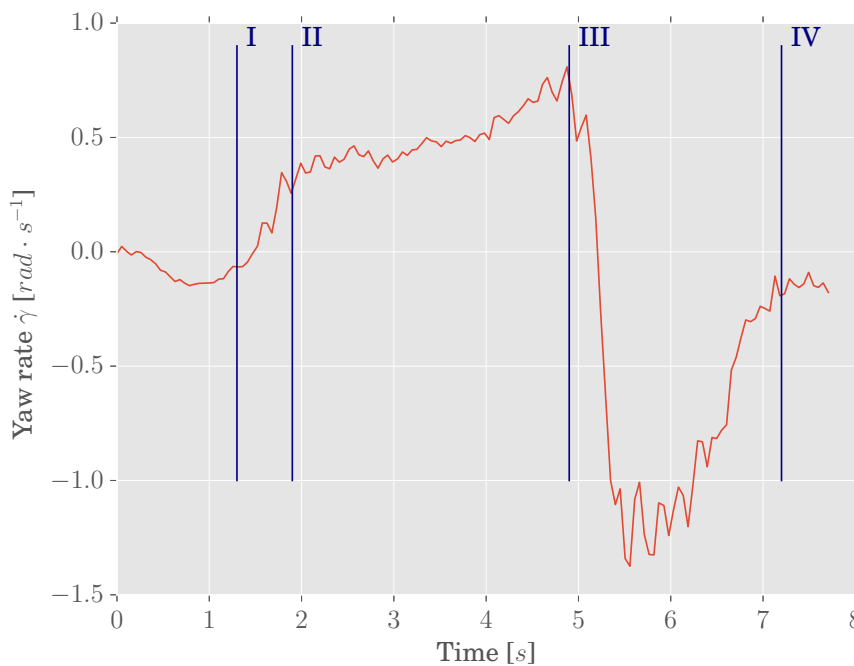
Figure 6.9: One of the yaw movements encountered during the testflight. The yaw speed is measured in the body frame of the kite. The blue lines indicate different important moments of the movement; I is the start of the steering input by the pilot, II is the end of the acceleration period, III is the end of the equilibrium steering period, and IV is the end of the return maneuver to a flight path to avert crashing.

The different stages can be distinguished between the defined moments I to IV. The equilibrium period between II to III shows an increasing signal which is not as expected but is caused by an increase in velocity that is occuring during this same period. This however should not change the relation given 5.1 and provide a constant value for G. It is this constant value that is needed to verify if the same turn rate law can be applied for this test setup.

The way to do this now is to determine the points in time where the equilibrium period takes place for each yaw maneuver, average the values that appear during this timeframe and compare this value to the average apparent wind velocity value and steering input that was applied during each maneuver.

$$G = \frac{\dot{\gamma}_{\text{avg}}}{V_{\text{a,avg}}\delta} \tag{6.6}$$

To find the points in time where the maneuver ends the maximum value for the yaw value in the earth fixed frame is used. The start of each maneuver is decided upon based on the roll and yaw of the earth fixed frame. An example of this is shown in figure 6.10. Here it can be seen that the maneuver starts at 1450 and ends at 1454.5 seconds. The difference in the roll and yaw maximum values is caused by the counteraction of gravity where the kite is rotated upwards to steer it away from the ground but there is a time delay for the forces to stop the kite from actually moving towards the ground. The yawing extreme is therefore the proper time to stop viewing it as a constant steering maneuver.
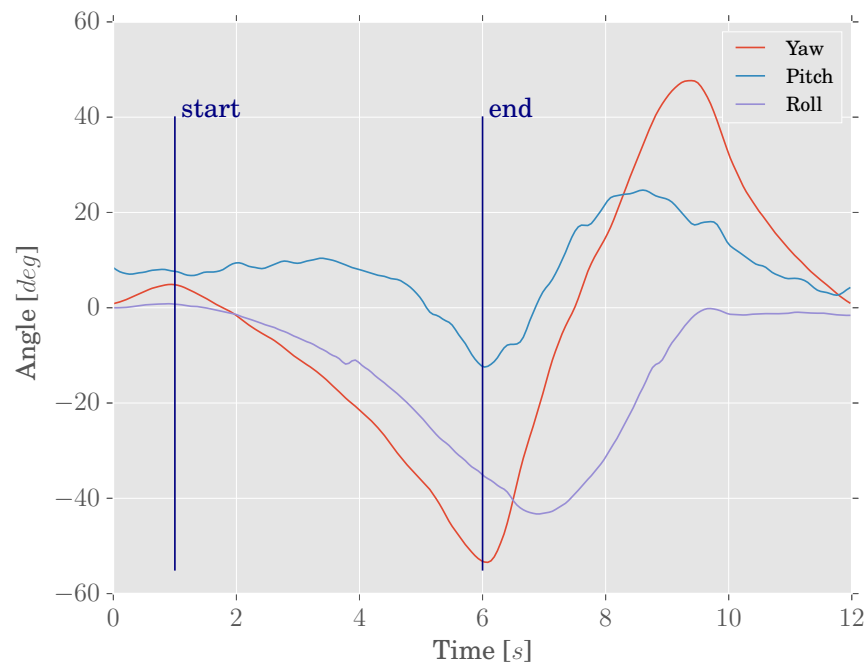
Figure 6.10: One of the yaw movements encountered during the testflight. The yaw and roll angle are measured in the local earth fixed reference frame. here the maneuver is seen to start at 1450 and the yawing stops at 1454.5 seconds.

Using this method the values for the turn rate are plotted against the the apparent wind velocity v_a times the steering input δ. The apparent wind velocity is taken from the pitot tube measurement and the δ is assumed to be constant and defined as a standard steering bar of 0.47 m to have an angle of 8 and 20 degrees for the different stopperball settings. These values are derived from photos taken during the test and shown in figures 6.11a and 6.11b. From the data that was collected by Oehler[27] it was clear that different power settings provide different values for G, these are therefore plotted in seperate figures.

The values shown in figure 6.12a to 6.12d correlate as was expected. In figure 6.12a however there is a clear offset between the two stopperball setttings, which is expected to be caused by a small difference in power setting that was applied during the test. The power setting where the stopperball allowed more powerfull steering was lower than with the small steering input and is therefore lower than expected. The other figures show a clear linear correlation between a product of the steering input and the apparent wind velocity on the one hand and the yawing rate on the other.

(a) The first setting of the stopperball allowed the pilot to steer the kites with a steering bar angle of 8°.

(b) The second setting of the stopperball allowed the pilot to steer the kites with a steering bar angle of 20°.

Figure 6.11: During the test a line with a stopperball set a maximum to the amount of steering that was possible allowing the pilot to steer constantly at this maximum setting. The two steering inputs are the result of two different stopperball positions on the line.
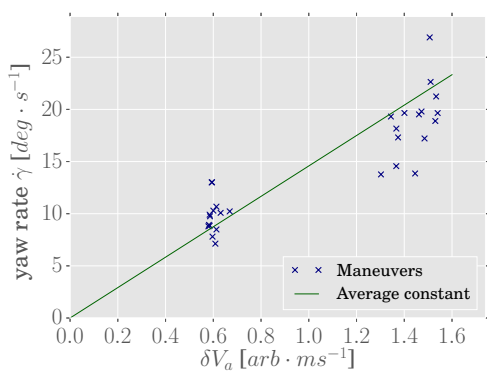
(a) Yaw rates $\dot{\gamma}$ versus the apparent wind velocity v_a for power setting 0.
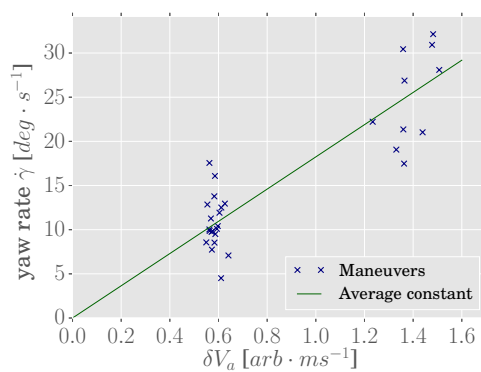
(b) Yaw rates $\dot{\gamma}$ versus the apparent wind velocity v_a for power setting 1.
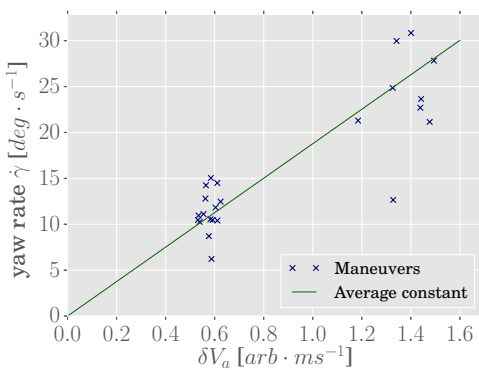
(c) Yaw rates $\dot{\gamma}$ versus the apparent wind velocity v_a for power setting 2.
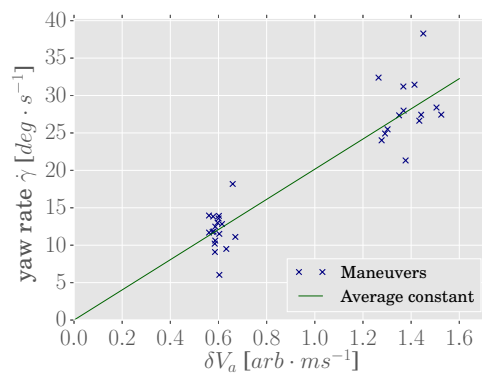
(d) Yaw rates $\dot{\gamma}$ versus the apparent wind velocity v_a for power setting 3.

Figure 6.12: The average yaw rates for the steady yawing period in plotted against the average apparent wind velocity v_a times the steering input δ. In all figures two distinct pointclouds are visible, these are the result of different contant steering inputs.

Angles at tips

According to the theory in chapter 2 the yaw rate should hold to equation 2.19. The steering is dependent on the lift and drag forces that come with different angles of attack and a warping of the kite by means of a differential application of tensile forces by means of a steering input. In order to see which of these effects is dominant the angles at the edges should provide important information. Figures 6.13a to 6.19d show the results of the experiments. The Euler angles at the right and left side are given as well as the C_R value, the

sideslip angle, the yaw rate, and the yaw acceleration.

Figures 6.13a to 6.13d show how the pitch angles at the sides behave with respect to the pitch angle measured in the middle of the kite as explained in section 4.1 and shown in figure 4.3. The results show that the deformed pitch angle of the side that is steered into goes up during the turn. This is exactly what current theory suggested by Breukels[6] says should happen. According to him the kite warps in a way that the pitch angle should increase at the side that the kite steers into. This tells us that for the rest of the steering surface where the surface is no longer perpendicular to the ground, there is positive change in local angle of attack which increases the lift and drag on the right side. The fact that the pitch goes down on the left side therefore determines that the local angles on the left side go down. The data shown also seems to correspond to the lift force offset discussed in chapter 2 however as the yaw results will show it appears that this effect is small.

Figures 6.14a to 6.14d show how the yaw angles at the sides behave with respect to the yaw angle measured in the middle of the kite as explained in section 4.1 and shown in figure 4.5. The left compass had problems and seemed to be inadequately calibrated to account for the vicinity of the battery pack. During some periods it drifted more than 50 degrees and all the absolute yaw angles are therefore assumed to be incorrect. At times that a yaw rate occurs however the Kalman Filter used in the IMU is highly dependent on the gyroscopes present and the differential data is used. First it is assumed that the initial angle relative to the central strut is symmetric to the one measured on the right. It is seen that the angle on the right starts off with a 26 degree offset and the left tip should therfore always start of with a minus 26 degree offset.

The data shows that the yawing goes in the direction opposite of what the drag differential steering suggests should happen. The deformations that are shown are opposite to what figure 2.4 shows. Both the right and left side turn against the direction of the turn. This means that the right side experiences a decrease in local angle of attack and the left side an increase in local angle of attack. Assuming that standard principles for airfoils are applicable the right side will see a decrease in drag forces where the left side will see an increase in drag force, thus creating a moment counter to that needed for the yaw rate to increase. Especially the first one and a half seconds after the steering input is given shows a sharp change in the yaw angle direction.

Figures 6.16a to 6.16d show how the roll angles at the sides behave with respect to the roll angle measured in the middle of the kite as explained in section 4.1 and shown in figure 4.4. The difference between the two starting values is explained by the fact that the left and right roll in opposite directions when related to the center. As with the yaw angles both sides now show the same deformations. This means that left side rolls inwards and the right side rolls outwards as shown in figure 6.15. Looking at the rate at which the roll changes however suggests that this is a secondary effect caused by changing aerodynamic circumstances rather than a deformation that is applied by the pilot.

Figures 6.17a and 6.18a show the sideslip angles. The positive angles correspond to the situation shown in figure 2.9. The kite moves to the right before yawing into the right direction. Between the power settings and the different steering inputs there seem to be no significant differences in sideslip angle besides the speed in which the angles are reached. The steering input of 20° reaches a sideslip angle of 6° in 3 seconds time where maneuvers with the 8° steering input take 6 seconds to reach this value.

Figures 6.17b and 6.18b show the apparent flow velocity v_a during the turns. From the velocity it can be seen that the kite starts to move into cross-wind flight path as it increases while the pitot tube is no longer directed into the direction of the upcoming flow. The change in flow velocity here is also very similar for different power settings and steering inputs. The difference between the two steering settings is again only the speed in which the extra velocities are reached: 6 seconds for 8° steering and $\pm$ 4 seconds for the 20° steering.

Figures 6.19a to 6.19d show the yaw rates and the accelerations based on these rates. The accelerations are calculated by means of second order accurate central differences in the interior points and either first or second order accurate one-sides (forward or backwards) differences at the boundaries. This makes sure that the yaw accelerations show the same period of time as the yaw rates. An initial attempt at finding the derivatives however provided unrealistic values that resulted from the minor fluctuations in the yaw rates. To counter this a low pass filter was implemented and all signals above 0.8 Hz were removed. The derivative of this smoothened signal is what is plotted in figures 6.19b and 6.19b.
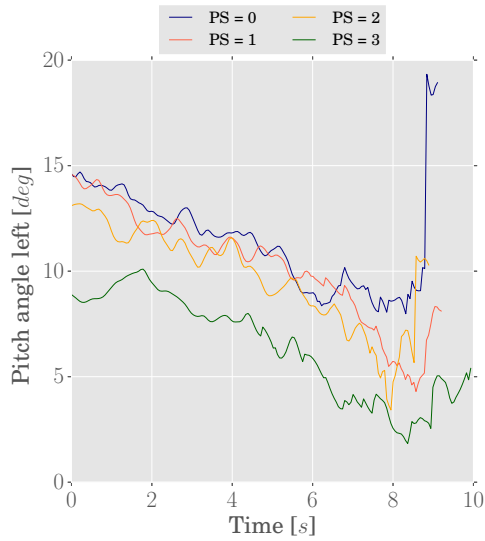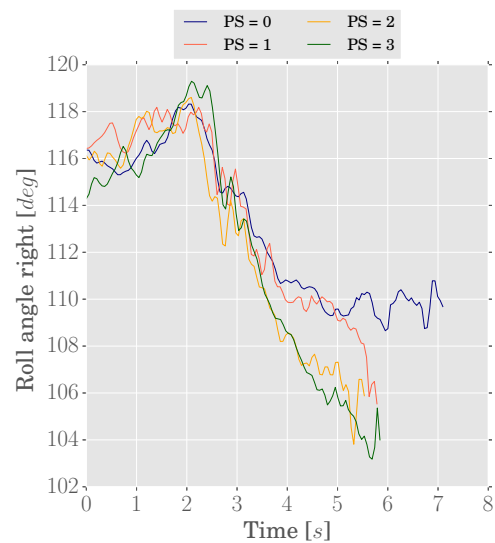
(a) Pitch angle offset at left (pilot point of view) side of the kite with a steering input where the steering bar has an 8° angle.
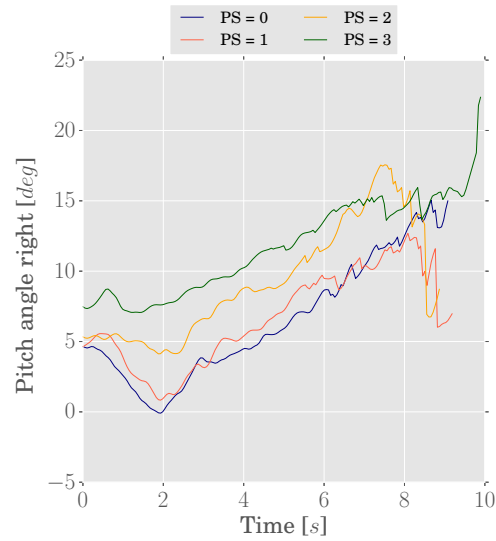
(b) Pitch angle offset at right (pilot point of view) side of the kite with a steering input where the steering bar has an 8° angle.
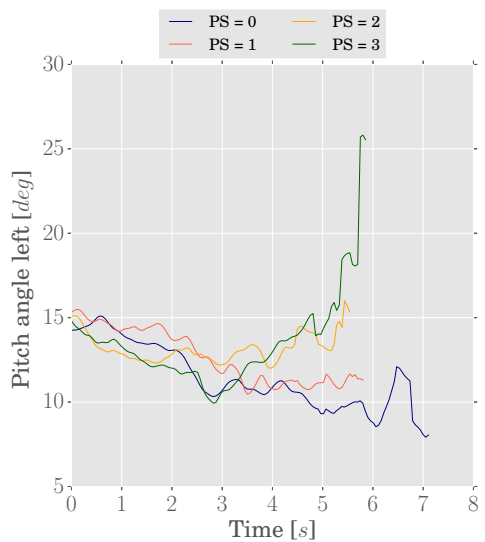
(c) Pitch angle offset at left (pilot point of view) side of the kite with a steering input where the steering bar has an 20° angle.
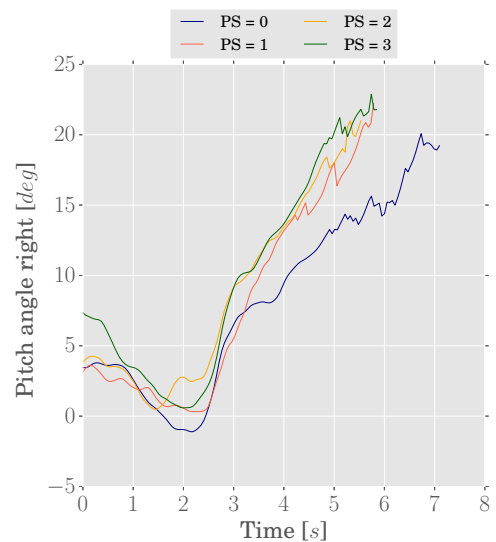
(d) Pitch angle offset at right (pilot point of view) side of the kite with a steering input where the steering bar has an 20° angle.

Figure 6.13: Average pitch values at the left and right sides during right turns that were performed with different power settings. The pitch angle at the middle is subtracted from these values to show how the edges deform with respect to the overall kite attitude. The maneuvers start at 2 seconds.

From the figures it is clear that at first a very large yaw acceleration is seen after which a less steep increase in yaw rate is seen. This additional increase in yaw rate is assumed to be the result of the increase in velocity shown in figures 6.18b and 6.18b.

Figures 6.20a and 6.20a show the moment forces needed to create the accelerations around the yaw axis as shown in figures 6.19b and 6.19b. The moment forces are small compared to the lift forces. During the
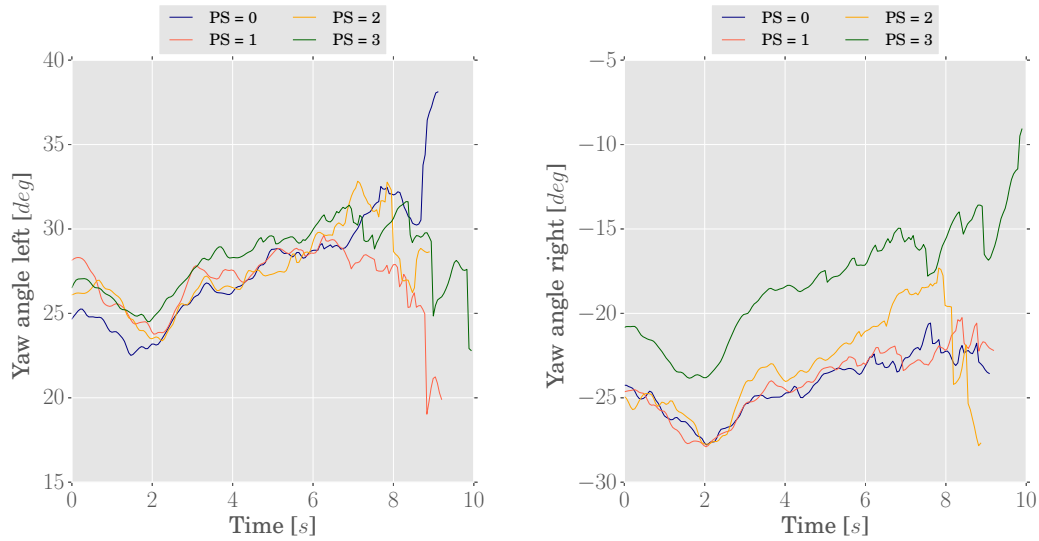
(a) Yaw angle offset at left (pilot point of view) side of the kite with a steering input where the steering bar has an 8° angle.

(b) Yaw angle offset at right (pilot point of view) side of the kite with a steering input where the steering bar has an 8° angle.
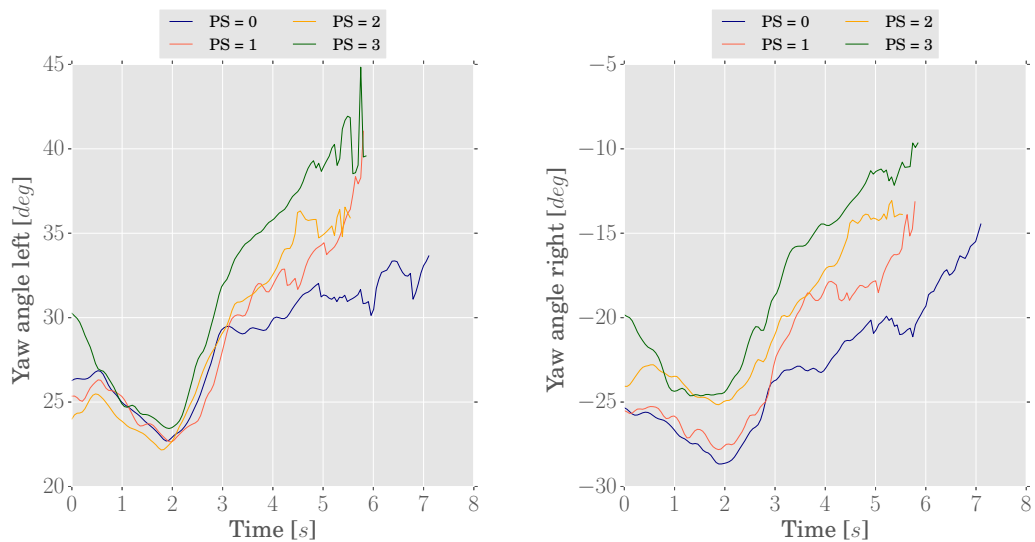
(c) Yaw angle offset at left (pilot point of view) side of the kite with a steering input where the steering bar has an 20° angle.

(d) Yaw angle offset at right (pilot point of view) side of the kite with a steering input where the steering bar has an 20° angle.

Figure 6.14: Average yaw values at the left and right sides during right turns that were performed with different power settings. The pitch angle at the middle is subtracted from these values to show how the edges deform with respect to the overall kite attitude. The maneuvers start at 2 seconds. The values for the right yaw angle are absolute values (the values measured are directly used) while the values for the left are manipulated

steady situation at zenith the forces measured by the force sensors are $\pm$ 150 N and reaches up to $\pm$ 1600 N during maneuvering into cross-wind flight paths.
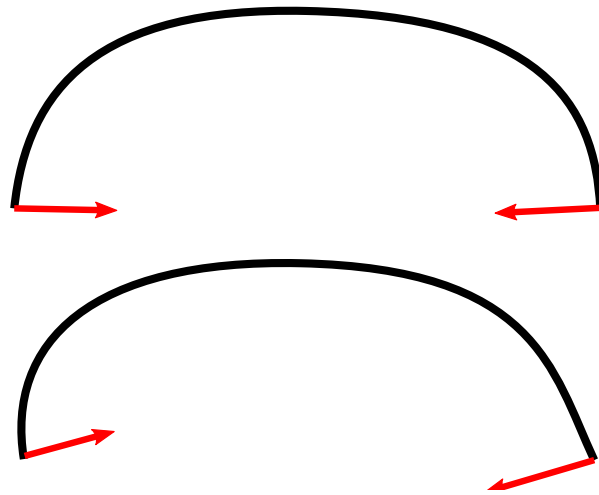
Figure 6.15: During the maneuvers the left and right side roll angle rotate into the same direction. This means that from the normal symmetric situation (upper) the right side rolls into the kite while the left side rolls outwards (lower).
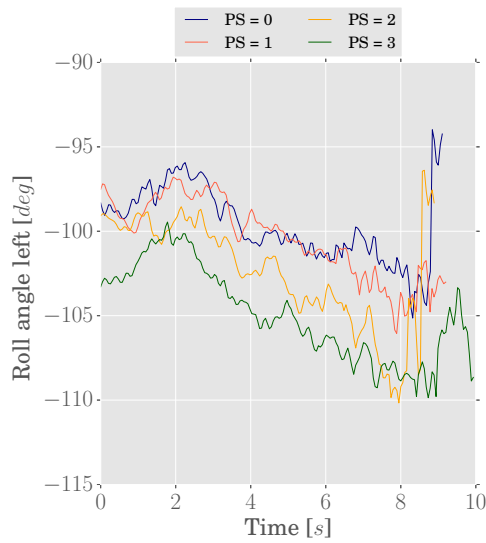
(a) Roll angle offset at left (pilot point of view) side of the kite with a steering input where the steering bar has an 8° angle.
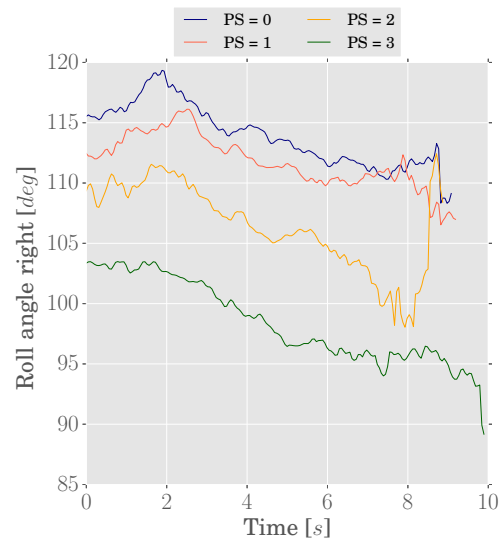
(b) Roll angle offset at right (pilot point of view) side of the kite with a steering input where the steering bar has an 8° angle.
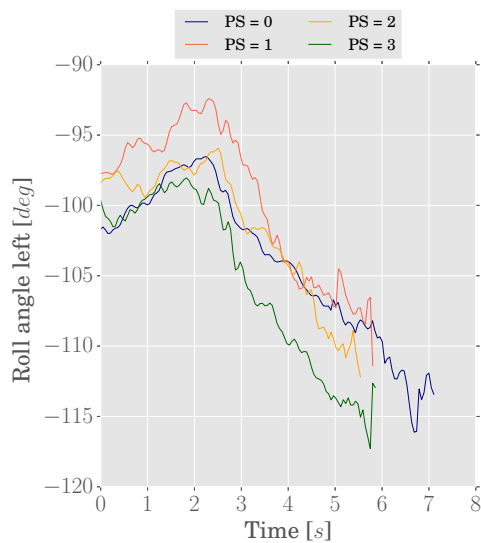
(c) Roll angle offset at left (pilot point of view) side of the kite with a steering input where the steering bar has an 20° angle.

(d) Roll angle offset at right (pilot point of view) side of the kite with a steering input where the steering bar has an 20° angle.

Figure 6.16: Average roll values at the left and right sides during right turns that were performed with different power settings. The pitch angle at the middle is subtracted from these values to show how the edges deform with respect to the overall kite attitude. The maneuvers start at 2 seconds.
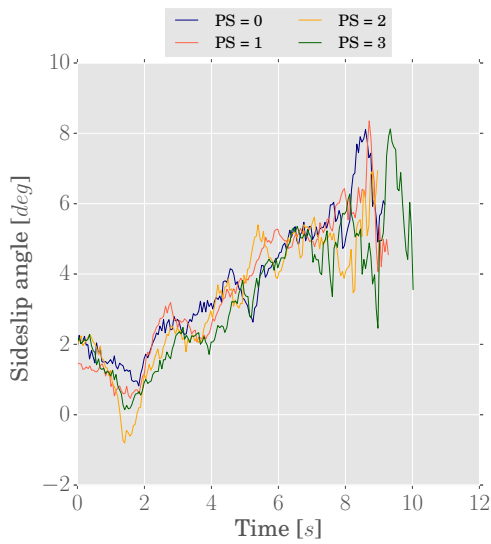
(a) Sideslip angle of the kite.
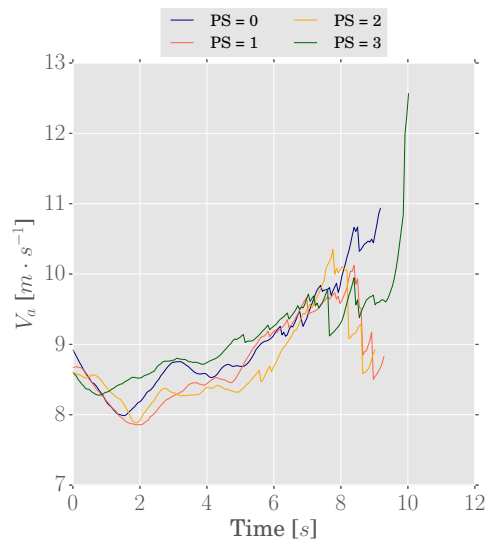
(b) v_a of the kite.

Figure 6.17: Average values during right turns that were performed with different power settings and a steering input of 8°. The sideslip angle is defined as positive when the flow vector is positive in the direction of the turn itself.
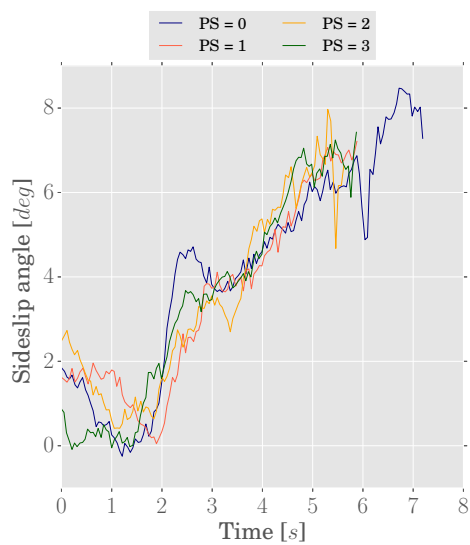
(a) Sideslip angle of the kite.
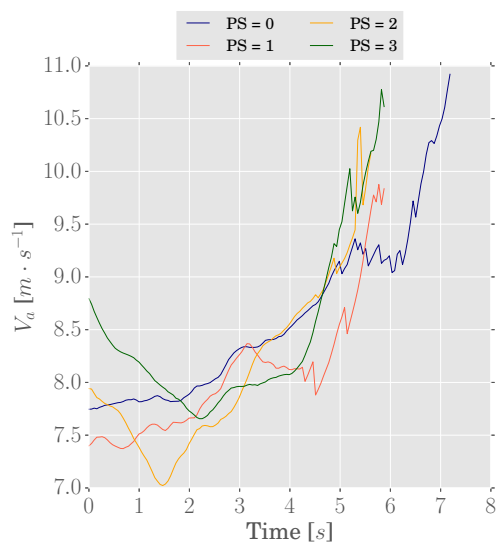
(b) v_a of the kite.

Figure 6.18: Average values during right turns that were performed with different power settings and a steering input of 20°. The sideslip angle is defined as positive when the flow vector is positive in the direction of the turn itself. The maneuvers start at 2 seconds.
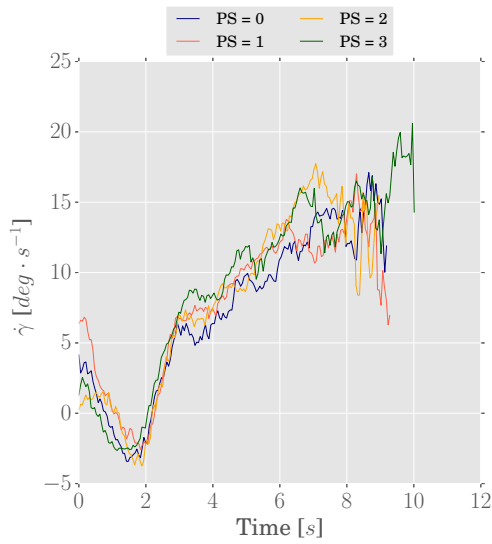
(a) Yaw rate $\dot{\gamma}$ angle of the kite.
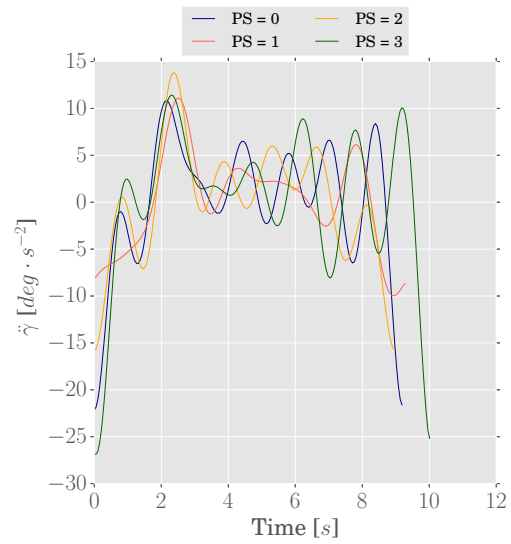
(b) Yaw acceleration $\ddot{\gamma}$ of the kite.
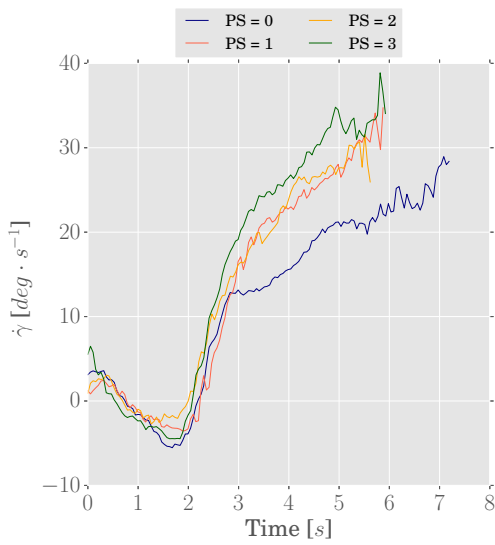
(c) Yaw rate $\dot{\gamma}$ angle of the kite.
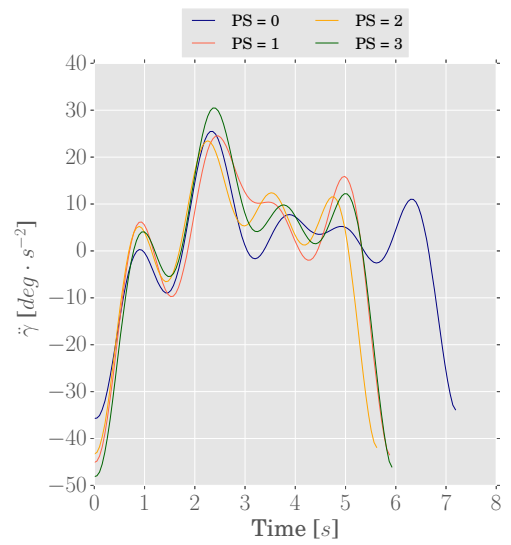
(d) Yaw acceleration $\ddot{\gamma}$ of the kite.

Figure 6.19: Average values for the yaw rate and acceleration during right turns that were performed with different power settings. The maneuvers start at 2 seconds.
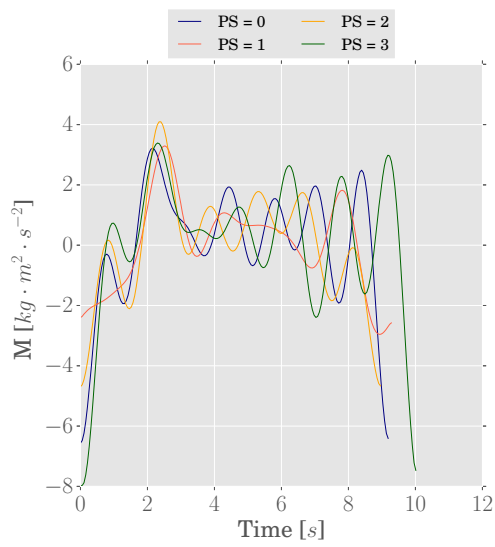
(a) Steering input of 8°
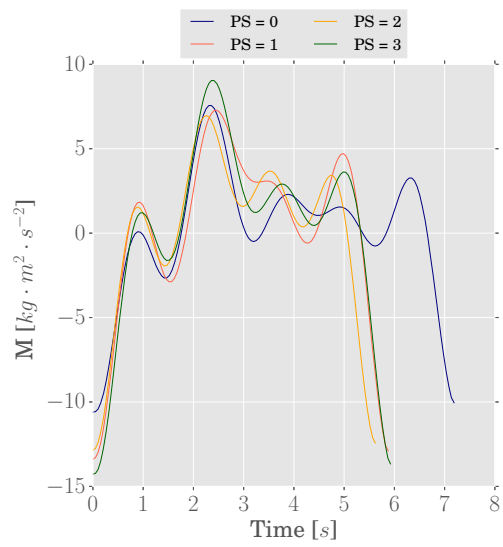
(b) Steering input of 20°

Figure 6.20: The moment forces applied on the kite for different power settings and different steering inputs. The moment force in the beginning of the maneuver (after 2 seconds) is the largest and after this the yawing of the kite creates a damping moment to slow the acceleration.

Comparison to theory

Using the data that was collected a means of steering can be determined for the Hydra. This data can now be used to compare it to the theory that was presented in chapter 2.

Warping or drag

From figures 6.13a to 6.13d it can be concluded that a warping of the kites is occuring. The right tip starts pointing upwards and the left tip is pointing downwards This is also in line with video images that were recorded on another flight test. Figure 6.21 shows two different points in time where one is in equilibruim where the kite is at zenith and the other while steering is applied.
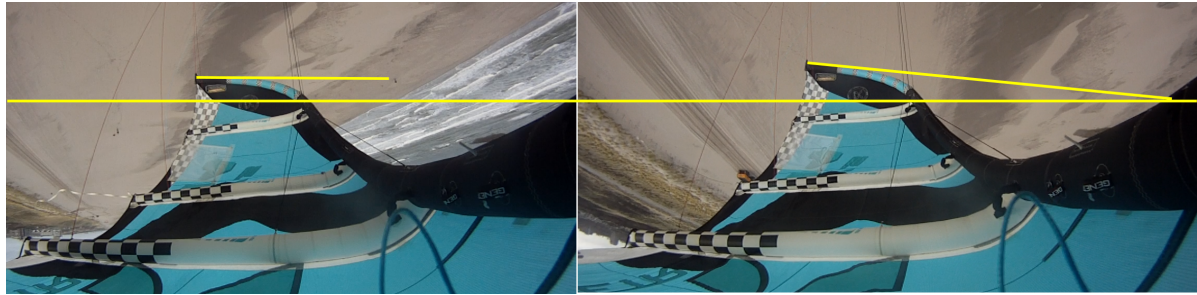
Figure 6.21: Image taken to show the tip angular change during a turn. Left: steady undeformed kite hanging still at zenith. Right: deformed turn in the direction of the video taken, the tip points upward with respect to the center of the kite where the camera is attached.

The yaw angles plotted in figures 6.14a to 6.14d show none of the behaviour that was expected to cause the drag based steering. However the author does think that the change in pitch angles as described above contribute to an increase in local angle of attack for the canopy some distance from the tip of the kite. But since no precise data is available there it seems that the yaw angles at the tips are a counteracting force to the turning of the kite. This also leads to a conclusion that for the Hydra the offset of the liftforces on both sides is not a large influence on the yawing of the kite. At the tips the largest offset is seen however here the local angle of attack is not in a state where a large lift force is expected. The areas where a lift force increase is seen however cannot have a significant change in position with respect to the center of gravity. Therefore the offset of lift forces moment term in equation 2.16 appears to be small.

The changing roll angle is in line with what is seen with the pitch angles due to a warping of the kite. This warping changes the angles of attack at the right positively and on the left negatively so the lift forces go up on the right and down on the left. this allows the kite on the left to go down and a higher lift force on the right forces that part upwards as shown in figure 6.15.

Sideslip angle

The sideslip angle is found to be positive as described in chapter 2. Therefore it can be concluded that the sideways accelerations occur before the moment forces rotate the kite in order for the kite to point directly into the apparent wind. This is another reason that leads the author to believe that the local angles of attack at the right side increase due to the change in pitch angle at the right tip. As well as the angles decrease at the left side. This creates an imbalance in the lift forces that point left and right which creates a net-force in the right direction causing an acceleration in that direction but not necessarily a rotation. It therefore seems that indeed the warping is the main phenomenon that drives the turning of the kite but it appears that an added drag force is the driver of the yaw movement instead of a lift force offset.

Kite equilibrium

From all the deformations it shows that during the turn no equilibrium is found. The pitch and yaw show a clear deformation step in the first second and a slow but steady increase in deformation afterwards. Where the roll angles at both sides show a steady change from the start to the end possibly due to secondary aerody-

namic effect instead of a steering input change (due to this steady change instead of a step in the beginning). The theory provided in chapter 2 on the other hand assumed a steady situation after the steering input deformations were applied. In this equilibrium the aerodynamic situation as a result of the new yaw rate would create a moment balance. The test setup however did not allow for a constant flow field in which the deformed kite could find a steady new situation. Figures 6.17b and 6.18b show the velocity during the turns. It is clear that the turning sends the kite into a cross wind flight path which increases the apparent wind velocity v_a. Since the flow velocity is of great importance to the aerodynamic forces it will influence the point where a balance between the deformations and the yaw rate might be found.

Validating the model

The model provided in chapter 2 that led to equation 2.16 can not be validated using the data that was extracted during the experiments. The overall picture that the deformations show corresponds to the basis for the equation. The fact however that the local behaviour of the kite shows a negative local angle of attack for the side that the kite moves towards is a problem. These phenomena are assumed to be the effect of a local deformation that has little influence on the local angles of attack of the larger steering surfaces. As was stated in chapter 3 the deformations that occur along the local airfoil are the least representable for the whole area. This means that in a next test either the Pixhawks need to be attached at a different location or that a different sensor is needed to show how the steering surface itself deforms.

7

Conclusions

The test setup proposed is able to determine the kite attitude during steady flight as well as flight maneuvers where the kite is deformed. The approach of several Inertial Measurement units provides a quantative insight in the deformations that the kite experiences during turning and shows which deformations play an important role in the steering mechanisms.

The results for the aerodynamic coefficent C_R based on the angle of attack rather than the power setting shows values that are similar to values found by Python [30]. Also the measurements by the windvane that is affected by the induced velocities of the vorticity of the kite shows promise to provide accurate angles of attack when the vorticity is taken into account. This would allow use of the system in crosswind flight conditions.

During powering up the angles at the center change less than the angles at the tips of the kite, this means that the sides of the kite are activated more heavily than the center. This can be a simple point of design focus as the center is the main supplier of lift forces as it is directed straight up and has the largest surface area. One might be able to accomplish this by using a differential application of powering up where the center is pulled down more than the sides. It is also found that the projected surface area changes during powering which creates a problem for comparing different kites as the nondimensionality based on a single projected surface area is no longer valid.

The yaw rates that are found correspond nicely with the turn rate law that was provided by literature. The yaw and pitch angles of the tips are affected by the steering input. The change in pitch angles are the main cause that the kite starts turning. The turning is set on by a warping of the kite where on one side the local angles of attack increase and on the other side they decrease. This change creates a net centripetal force moving the kite into a circular path. The added lift forces go alongside an increase in drag forces that make the kite turn into the direction of the movement. The roll angle also changes but seems to be a secondary effect due to an increase in lift forces on one side and decrease on the other side.

The setup was not able to reach an equilibrium state of turning where all deformations are stable and the kite has a constant yaw rate. The change of steady flight at zenith into a cross-wind flight path is assumed to be the cause of not finding a steady state. As the velocity kept increasing during every maneuver no balance was found. The proposed equation assuming equilibrium of the kite during a turn can therefore not be validated. The found results however do show the physical principles that lead to the equation.

The design goals for kites like the Hydra were never generating power. From the results it can be concluded that changing the power setting affects parts of the kite in different manners. So altering how much the central part changes angle of attack for example could be a simple but effective means of increasing performance. When the current setup is used a specific design that tries to increase for example the effectiveness of powering up a kite can be tested. This can speed up the process of optimizing a kite for producing wind energy and in turn allow an AWE system to become more efficient or provide more power.

8
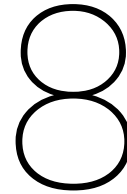
Recommendations

The recommendations can be divided into two categories. First there are some improvements that need to be made to the test setup before it can be used regularly as a means of testing different kinds of kites on a structural basis. Secondly there are different test possibilities of the setup that would be very interesting.

Test setup

The Pixhawks have shown to be valuable and relatively cheap devices to show what different parts of the kite are doing. The compass however turned out to be sensitive to the presence of the battery that powered it. The first recommendation is changing the setup so that the battery is located sufficiently far from the compass to avoid an effect on the measurements.

Also the logging of the data on the SD cards proved to be problematic. More than once there was either data missing or corrupted. The system should be adapted in a way where the measured data is directly sent to the observer in order to check if all data is being logged and makes sense. So an antenna that is hooked up to the pixhawk and sends data to a computer should solve these issues.

Test possibilities

Originally the idea was to use this test setup in cooperation with the testing facilities present at TUBerlin. The system there can inprove the setup by:

- Logging forces and angles on the ground for L/D determination.

- Steering inputs are controlled by servos and logged.

- The towing setup probably creates a significantly cleaner flow.

Besides this the setup can also prove to be valuable in field testing of the full Kitepower system. The angle of attack measured by the windvane with correction for the lift vortex induced velocity shows a great similarity to the pixhawk values. This means that in cross wind flight it should be able to produce the proper angles as well. In this case the yaw rates should show a much more stable nature as the kite remains in the same cross wind circular flight path which in turn allows for a validation of the theory that the deformation in flight remains constant during a single turn.

Bibliography

[1] The angle measurement sensor used for the wind vanes. URL `http://ams.com/eng/Products/Magnetic-Position-Sensors/Angle-Position-On-Axis/AS5043`.

[2] URL `https://www.surfertoday.com/kiteboarding/13619-everything-you-need-to-know-about-kite-control`.

[3] 2017. URL `https://pixhawk.org/`.

[4] 2018. URL `http://genetrixkites.com.ua/products/hydra-v5/`.

[5] Christina Archer. *An Introduction to eteorology for Airborne Wind Energy*, chapter 5, pages 81–92. Springer, 2013.

[6] Jeroen Breukels. *An Engineering Methodology for Kite Design*. 2011. ISBN 9789088912306. URL `http://repository.tudelft.nl/assets/uuid:cdece38a-1f13-47cc-b277-ed64fdda7cdf/Thesis{_}jeroen{_}breukels.pdf`.

[7] Antonello Cherubini. Awes taxonomy. Personal communications.

[8] Antonello Cherubini, Andrea Papini, Rocco Vertechy, and Marco Fontana. Airborne Wind Energy Systems: A review of the technologies. *Renewable and Sustainable Energy Reviews*, 51:1461–1476, 2015. ISSN 13640321. doi: 10.1016/j.rser.2015.07.053. URL `http://linkinghub.elsevier.com/retrieve/pii/S1364032115007005`.

[9] George M. Dadd. Kite dynamics for ship propulsion. page 215, 2013.

[10] Moritz Diehl. *Airborne Wind Energy: Basic Concepts and Physical Foundations*, chapter 1, pages 3–22. Springer, 2013.

[11] Michael Erhard and Hans Strauch. Control of Towing Kites for Seagoing Vessels. *IEEE Transactions on Control Systems Technology*, 21(5):1–1, 2012. ISSN 1063-6536. doi: 10.1109/TCST.2012.2221093.

[12] Michael Erhard and Hans Strauch. Sensors and navigation algorithms for flight control of tethered kites. *European Control Conference (ECC13)*, page 6, 2013. URL `http://arxiv.org/abs/1304.2233`.

[13] L. Fagiano, A.U. Zgraggen, M. Khammash, and M. Morari. Automatic control of tethered wings for airborne wind energy: Design and experimental results. *2013 European Control Conference, ECC 2013*, 22 (4):992–997, 2013. ISSN 07431619. doi: 10.1109/TCST.2013.2279592.

[14] Lorenzo Fagiano. *Control of Tethered Airfoils for High-Altitude Wind Energy Generation*. PhD thesis, Politecnico di Torino, 2009.

[15] Uwe Fechner. *A Methodology for the Design of Kite Power Control Systems*. 2014. ISBN 9789402804096. doi: 10.4233/uuid.

[16] Uwe Fechner and Roland Schmehl. Flight path control of kite power systems in a turbulent wind environment. *Proceedings of the American Control Conference*, 2016-July(July):4083–4088, 2016. ISSN 07431619. doi: 10.1109/ACC.2016.7525563.

[17] Sebastien Gros, Mario Zanon, and Moritz Diehl. A relaxation strategy for the optimization of Airborne Wind Energy systems A Relaxation Strategy for the Optimization of Airborne Wind Energy Systems. (January), 2013.

[18] R.C. Hibbeler. *Engineering mechanics Statics*. Pearson, 2010.

[19] http://www.skysails.info/english/. Skysails website, September 2017. URL `http://www.skysails.info/english/`.

[20] Jan Hummel and Doktor Der Ingenieurwissenschaften. *Automatisierte Vermessung und Charakterisierung der dynamischen Eigenschaften seilgebundener , vollflexibler Tragflächen*. PhD thesis, Technical University of Berlin, 2017.

[21] J.C. Stevenson. Traction kite testing and aerodynamics. page 286, 2003.

[22] Claudius Jehle. Automatic Flight Control of Tethered Kites for Power Generation. page 67, 2012. URL `https://mediatum.ub.tum.de/doc/1185997/1185997.pdf`.

[23] Kang-Rong Chiang John W. Then. Experimental determination of moments of inertia by the bifilar pendulum method. *American Journal of Physics*, 1970.

[24] Miles L Loyd. Crosswind Kite Power. 4(3):106–111, 1980.

[25] J.a. Mulder, W.H.J.J. van Staveren, J.C. van der Vaart, and Et Al. Flight Dynamics. 2013.

[26] Max M. Munk. The minimum induced drag of aerofoils. *National advisory committee for Aeronautics*, 19017.

[27] Johannes Oehler. Measuring apparent flow vector on a flexible wing kite. Master's thesis, Delft University of Technology, University of Stuttgart, 2017.

[28] Optitrack. General information on cyberzoo tracking system. FAQ, January 2018. URL `http://optitrack.com/support/faq/general.html`.

[29] P.R. Payne and C. McCutchen. Self-erecting windmill, October 26 1976. URL `http://www.google.com/patents/US3987987`. US Patent 3,987,987.

[30] Benoit Python. Methodology Improvement for Performance Assessment of Pumping Kite Power Wing. 2017.

[31] Radiolink. Gps sensor for pixhawk. URL `https://www.robotshop.com/en/radiolink-se100-gps-module-pixhawk.html`.

[32] Roland Schmehl. *Airborne Wind Energy 2011*. 2011. ISBN 9783642399640.

[33] Transducer Techniques. Website of transducer used for the force ssensor., January 2018. URL `https://www.transducertechniques.com/`.

Force measurement

In order to record the tension of the lines, a self designed data logger shown in figure A.1 is used. The data logger uses a micro SD card to store the data. The power supply is an external battery pack with 8 simple AA-batteries. The following sections describe briefly the main components and their technical specifications.

Figure A.1: The self made force measurement system consisting of three load cells and a blackbosx with electronic devices and microcontrollers.

Load cells

In general a load cell is a device that transduces mechanical energy into electrical signals. The output signal is proportional to the mechanical power, mostly strain or forces acting on it. Load cells based on strain gauges are mostly used in industrial application. Strain gauges change their electrical resistance during deformation, which is proportional to applied forces. Load cells usually consist of four strain gauges wired in a wheatstone bridge placed on a piece of metal or plastic. Wheatstone bridges allow most sensitive measurements and prevent errors due to temperatue fluctuations. Excitation voltage as input is in range between 5 VDC [Volts of Direct Current] to 20 VDC, outcoming signal due to strain gauge deformation in a few milivolts range. Hence voltage amplifiers are required for decent measurements. The used amplifier is described briefly in the following section. The used load cells "Mini Low Profile Load Cell" manufactured by Transducer Techniques are small scaled and allow stable measurements for in line application in tension and compression[33]. To measure the tension of the lines three load cells are required. One connected to the power lines and two connected to the right and left steering lines. Compared to the steering lines the tension of the power line can be greater up to one order of magnitude. In order to account for this difference the steering line sensors are attached to MLP-300 which can be loaded up to 300 pounds (136 kg) whereas the power line measurement uses a MLP-1000 that can be loaded up to 1000 pounds (454 kg). The three load cells are wired up with the amplifier boards in the data logger box as shown in figure A.1.

Amplifier boards

Since the load celss in general deliver output voltages in a range of a few millivolts these signals need to be amplified. This is done be menas of an amplifier board or conditioner module [33]. The used amplifier TMO-1 manufactured by Transducer Techniques is shown in figure A.2. All three amplifiers are powered from one 12 VDC power supply as input source. The units provide one balance potentiometer and one gatin potentiometer to adjust the output signal in a range the following module can work with. Ful scale analog output is set at ± 8 VDC. The following ADC included in the microcontroller described in section A.3 requires positive input voltages ranging from 0 to 3.3 VDC. An offset of 100 mV protects the circuit from negative voltages whereas the gain potentiometer limits the output signal to 3.3 V max at full load capacity of connected load cells. The factory set band-width is 220 H which means that ata logging up to every 4.5 ms is feasible. The floating shunt circuit allows calibration at the transducer board to eliminate measurement error due to wire length.
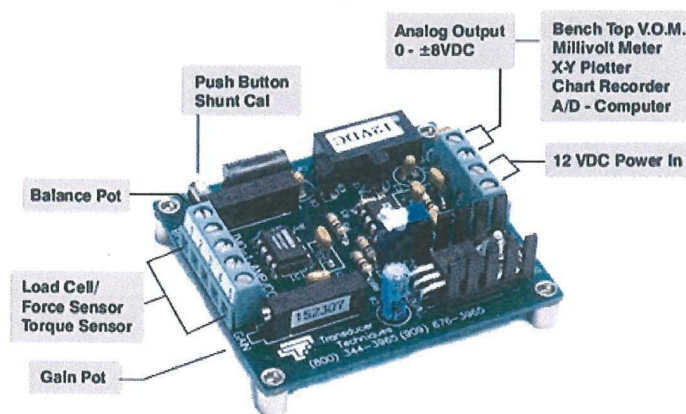
Figure A.2: Amplifier module TMO-1 from Transducer Techniques

STM32 Nucleo board

The ST<32 F303RE is a 32-bet microcontroller manufactured by STMicroelectronics. Microcontrollers in general are small chip based computeres used in automatically controlled devices. In a simplified way, a microcontroller contains internal memory, processor cores and several programmable input and output peripherals. In this case the STM32 provides different functions required to log data in relation to time on external memoy storage (micro SD). Three ADC's convert the analog output signal of 3.3 V maximum of each amplifier

board into a digital 12-bit resolution. The relation between pulling force acting on the lines and the logged value is give in equations A.1 and A.2

$$Q = \frac{E_{\text{FSR}}}{2^M} \tag{A.1}$$

With Q the digital resolution of the measurement, E_{FSR} is the voltage range, and M the bit resolution.

$$G = \frac{V_{\text{output}} - V_{\text{offset}}}{C} \tag{A.2}$$

Where G represents the relation between load and output voltage, V_{output} is the output voltage, V_{offset} is the offset voltage, and C is the capacity. Then the value Q devided by the sensitivy G provides the linearity between the digital value and the load on the load cell.
Figure A.3 shows the schematic of the circuit board connections.
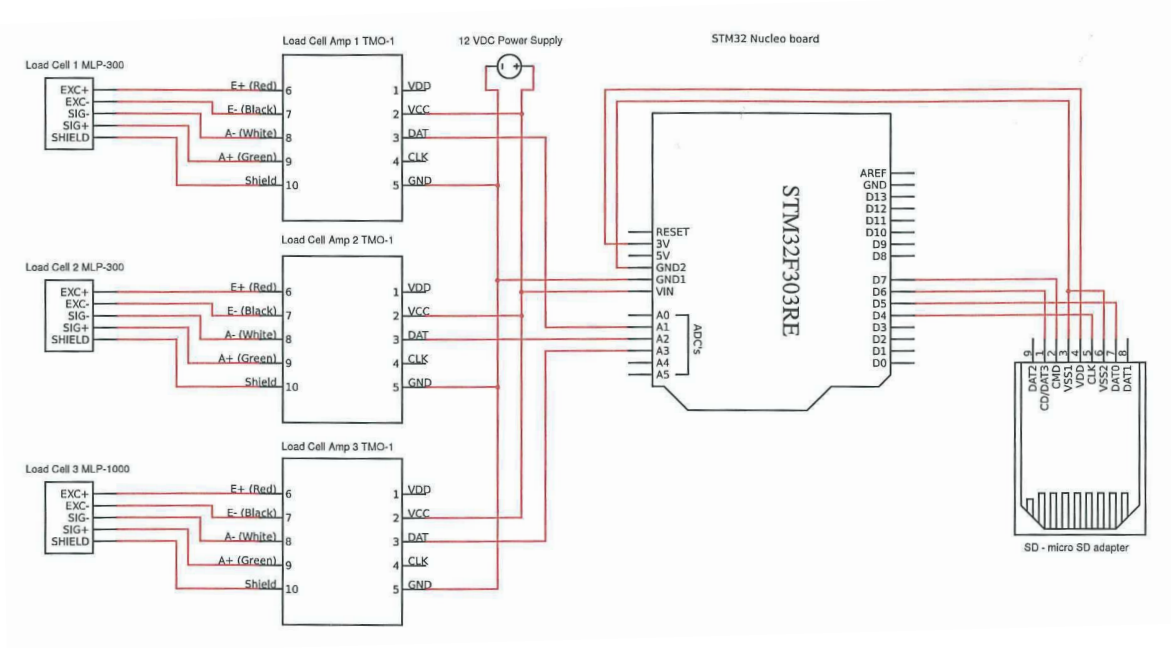
Figure A.3: The schematic of the circuit board connections

The board starts logging the minute the power supply is connected. Since gusts can change the flow velocity within tenths of a second the sampling rate is set to 50 Hz, thus every 20 ms a value is logged for all three line forces.
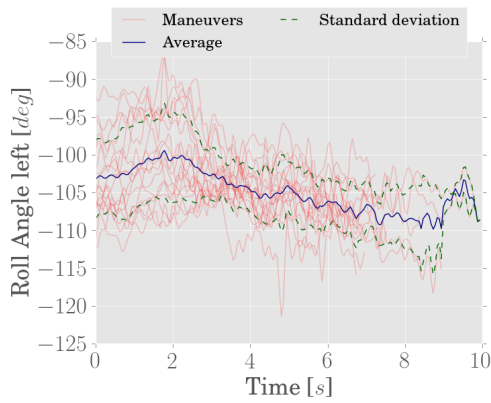
B

Deformation results
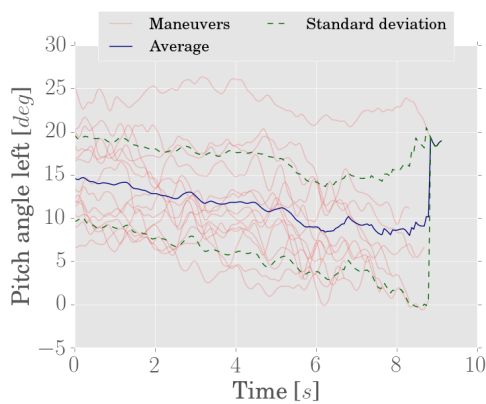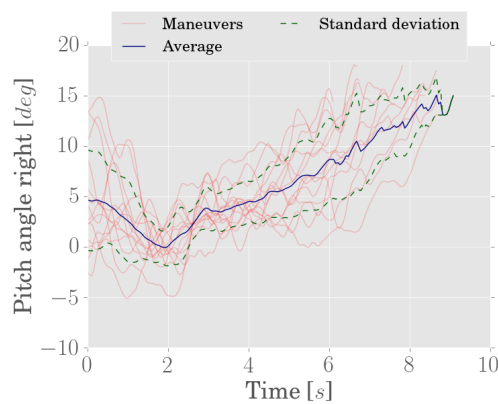
(a) Left (pilot point of view) side of the kite.   (b) Right (pilot point of view) side of the kite.

Figure B.1: Pitch values during right turns that were performed with the 0th power setting and a steering input of 8 ^{o}. The pitch angle at the middle is subtracted from these values to show how the edges deform with respect to the overall kite.
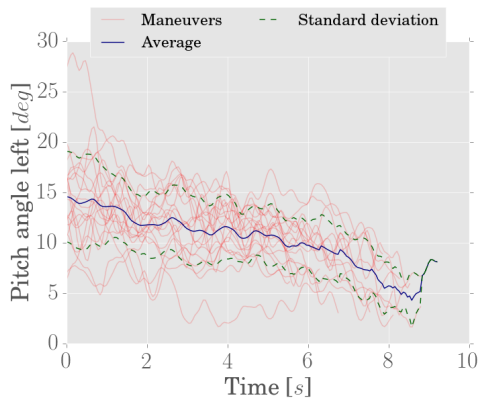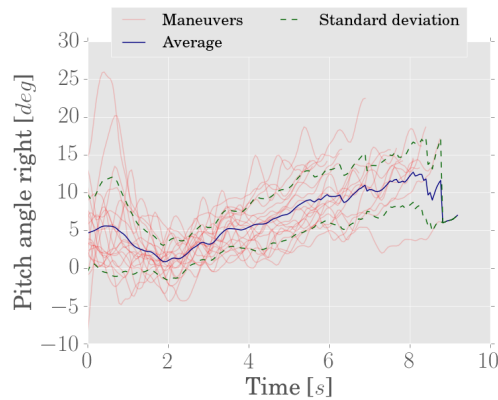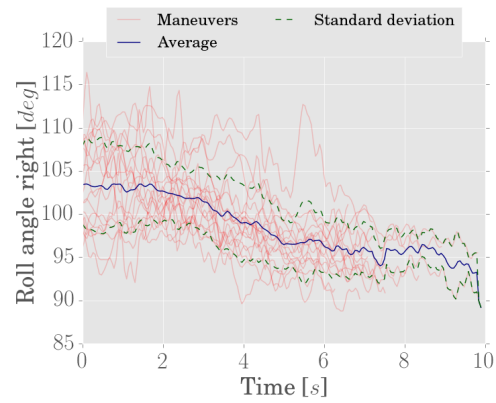

(a) Left (pilot point of view) side of the kite.   (b) Right (pilot point of view) side of the kite.

Figure B.2: Pitch values during right turns that were performed with the 1st power setting and a steering of 8 ^{o}. The pitch angle at the middle is subtracted from these values to show how the edges deform with respect to the overall kite.
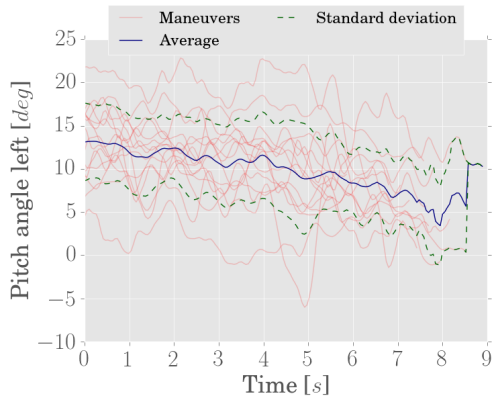
(a) Left (pilot point of view) side of the kite.
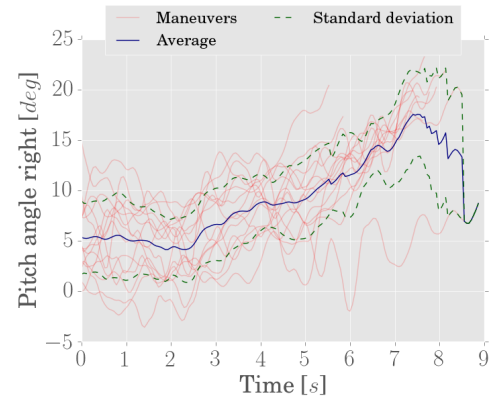
(b) Right (pilot point of view) side of the kite.

Figure B.3: Pitch values during right turns that were performed with the 2nd power setting and a steering input of 8 ^{o}. The pitch angle at the middle is subtracted from these values to show how the edges deform with respect to the overall kite.
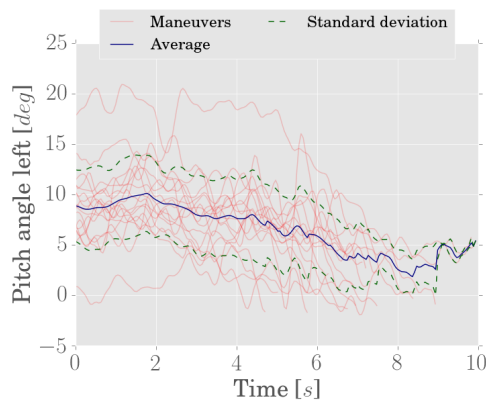
(a) Left (pilot point of view) side of the kite.
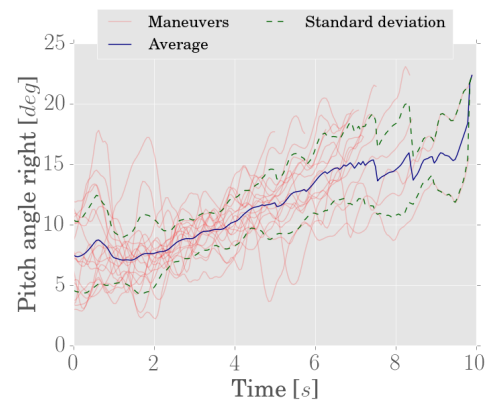
(b) Right (pilot point of view) side of the kite.

Figure B.4: Pitch values during left turns that were performed with the 3rd power setting and a steering input of 8 ^{o}. The pitch angle at the middle is subtracted from these values to show how the edges deform with respect to the overall kite.
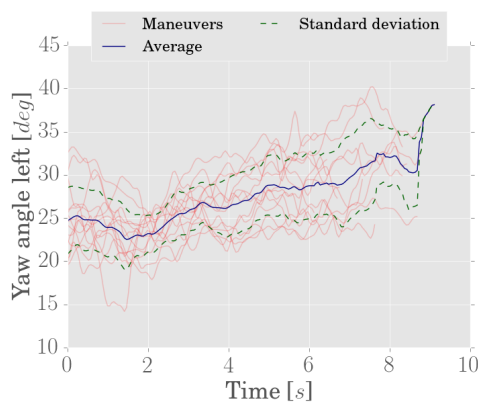
(a) Left (pilot point of view) side of the kite.
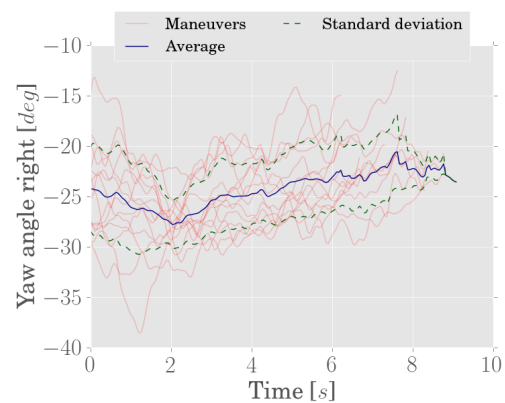
(b) Right (pilot point of view) side of the kite.

Figure B.5: Yaw values during right turns that were performed with the 0th power setting and a steering input of 8 ^{o}. The yaw angle at the middle is subtracted from these values to show how the edges deform with respect to the overall kite.
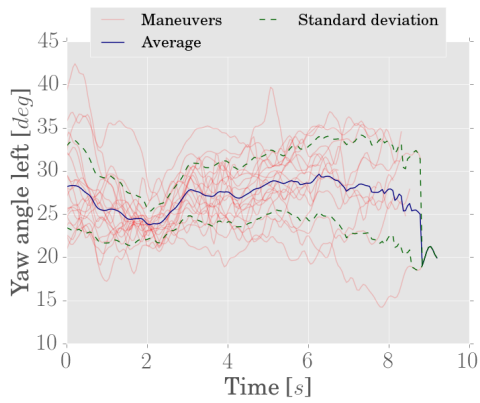
(a) Left (pilot point of view) side of the kite.
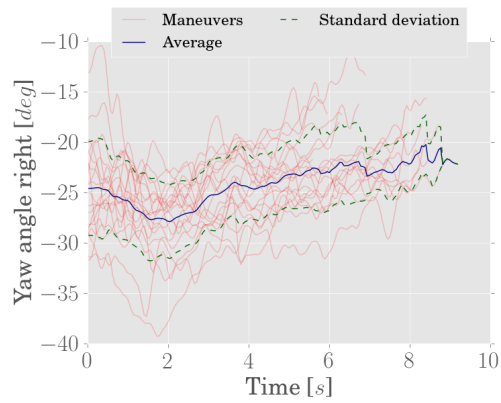
(b) Right (pilot point of view) side of the kite.

Figure B.6: Yaw values during right turns that were performed with the 1st power setting and a steering input of 8 ^{o}. The yaw angle at the middle is subtracted from these values to show how the edges deform with respect to the overall kite.
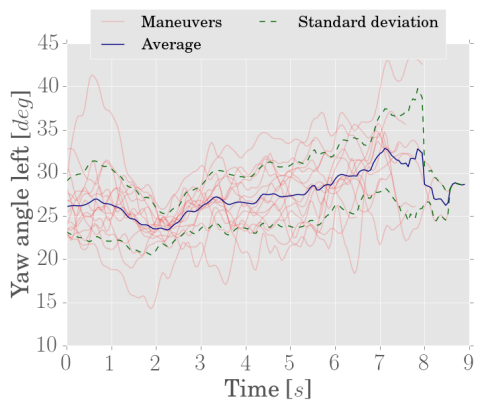
(a) Left (pilot point of view) side of the kite.
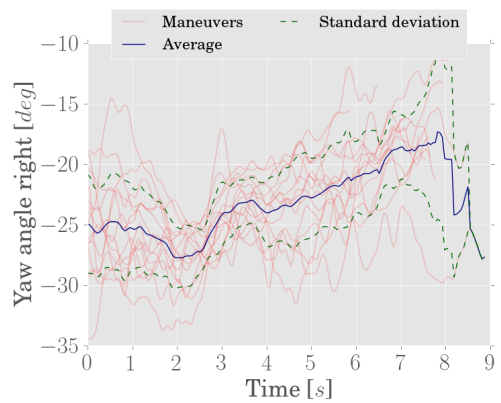
(b) Right (pilot point of view) side of the kite.

Figure B.7: Yaw values during right turns that were performed with the 2nd power setting and a steering input of 8 ^{o}. The yaw angle at the middle is subtracted from these values to show how the edges deform with respect to the overall kite.
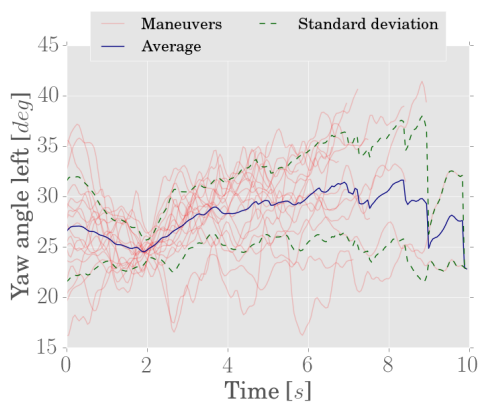
(a) Left (pilot point of view) side of the kite.
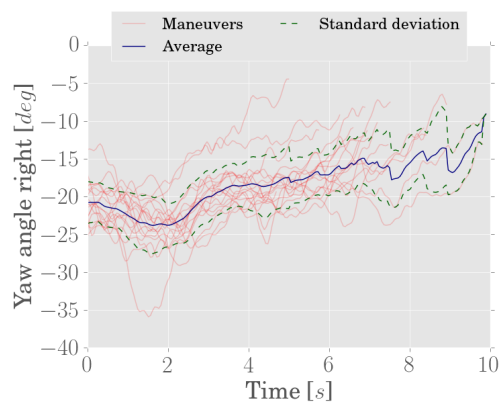
(b) Right (pilot point of view) side of the kite.

Figure B.8: Yaw values during left turns that were performed with the 3rd power setting and a steering input of 8 ^{o}. The yaw angle at the middle is subtracted from these values to show how the edges deform with respect to the overall kite.
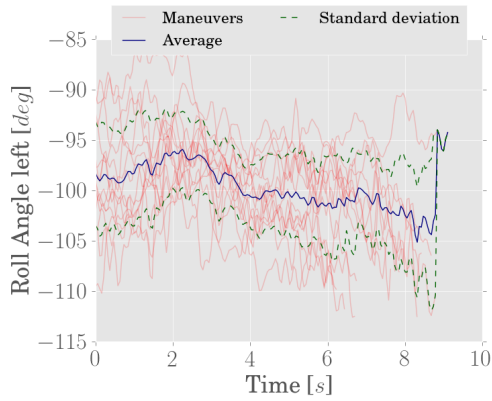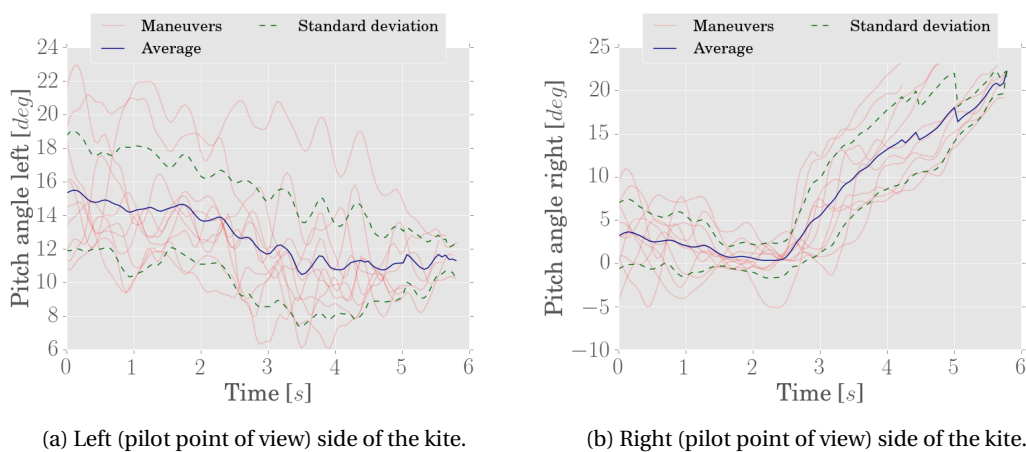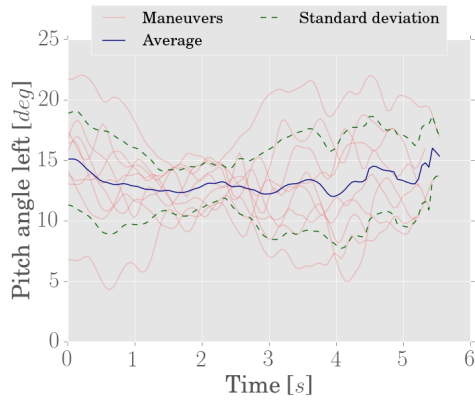
(a) Left (pilot point of view) side of the kite.
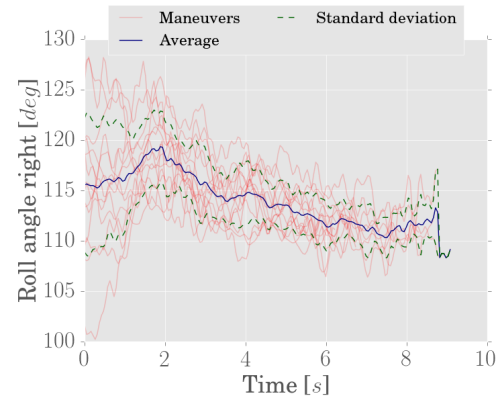
(b) Right (pilot point of view) side of the kite.

Figure B.9: Roll values during right turns that were performed with the 0th power setting and a steering input of 8 ^{o}. The roll angle at the middle is subtracted from these values to show how the edges deform with respect to the overall kite.
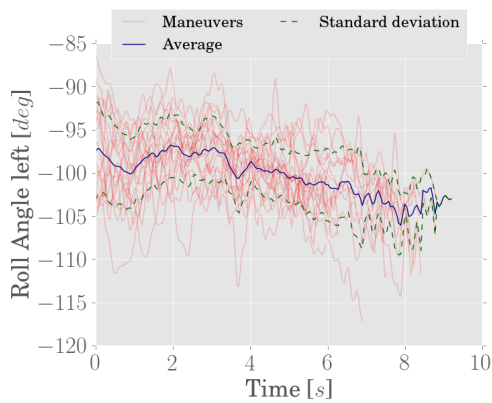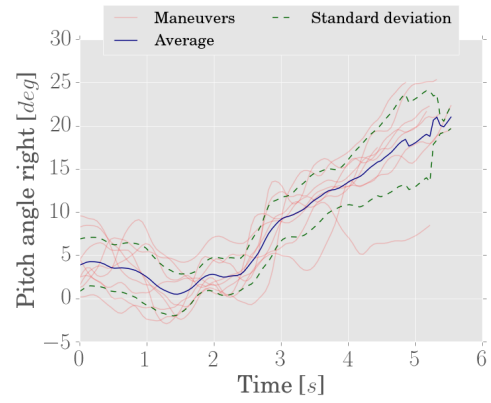

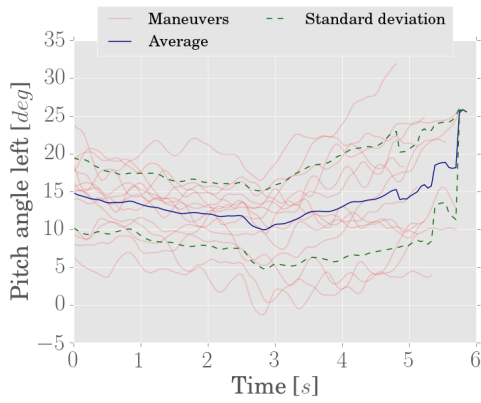(a) Left (pilot point of view) side of the kite.
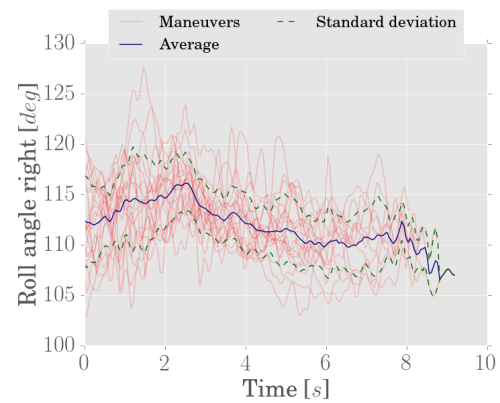
(b) Right (pilot point of view) side of the kite.

Figure B.10: Roll values during right turns that were performed with the 1st power setting and a steering input of 8 ^{o}. The roll angle at the middle is subtracted from these values to show how the edges deform with respect to the overall kite.
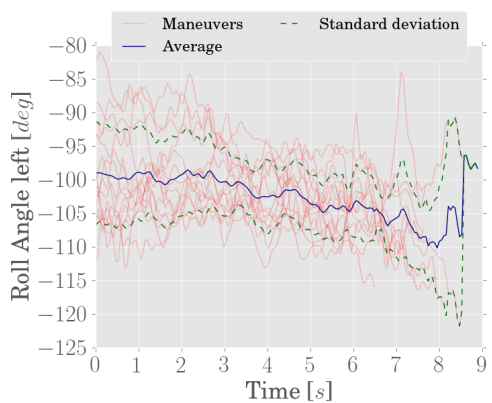
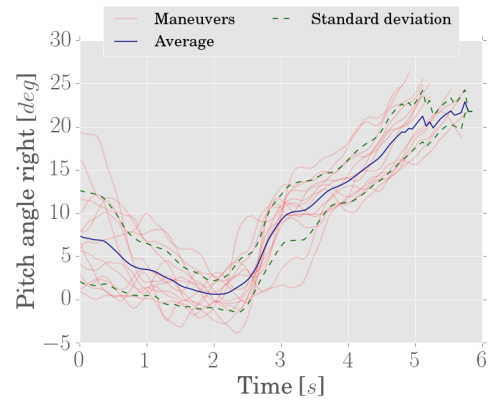(a) Left (pilot point of view) side of the kite.
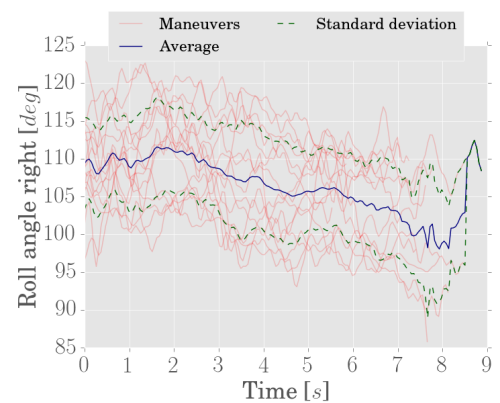
(b) Right (pilot point of view) side of the kite.

Figure B.11: Roll values during right turns that were performed with the 2nd power setting and a steering input of 8 ^{o}. The roll angle at the middle is subtracted from these values to show how the edges deform with respect to the overall kite.
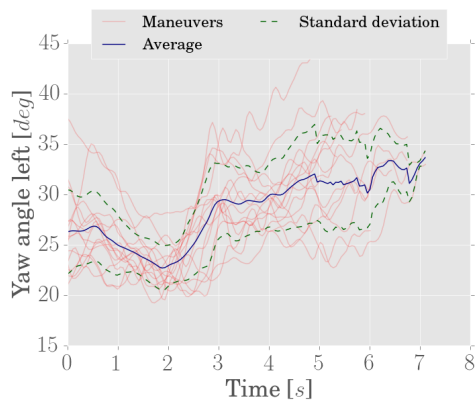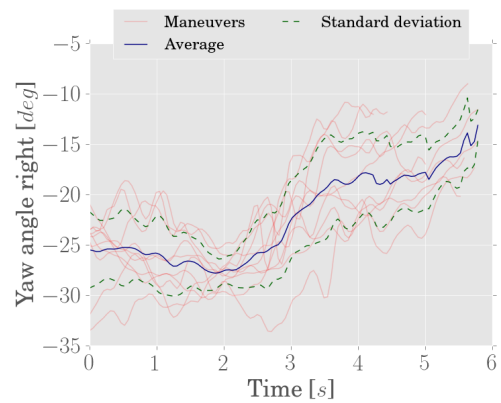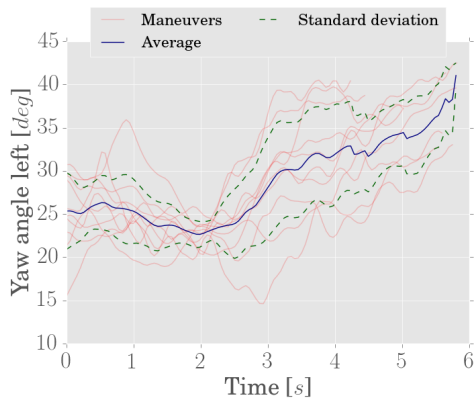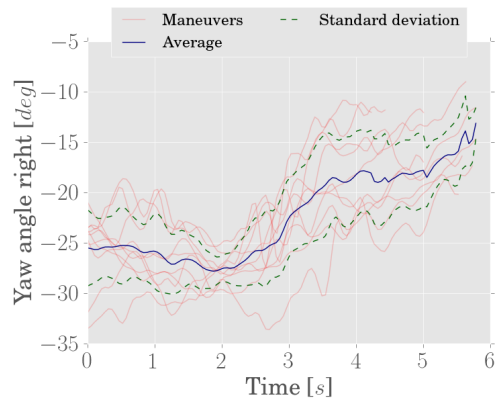
(a) Left (pilot point of view) side of the kite.

(b) Right (pilot point of view) side of the kite.

Figure B.12: Roll values during left turns that were performed with the 3rd power setting and a steering input of 8 ^{o}. The roll angle at the middle is subtracted from these values to show how the edges deform with respect to the overall kite.
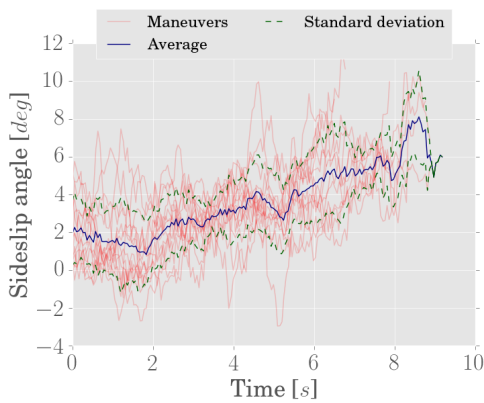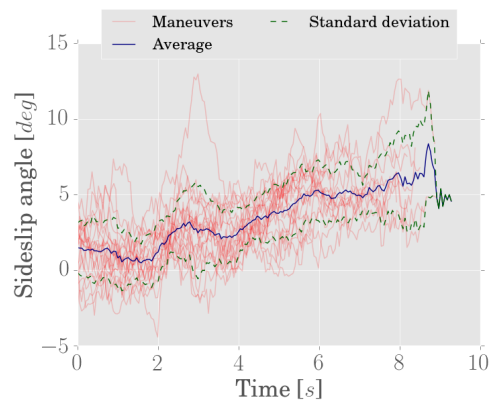
(a) Power setting 0

(b) Power setting 1

Figure B.13: Sideslip values for right turns measured by the β_s windvane and corrected for the yaw induced velocities. These values are found using the steering input of 8 ^{o}.
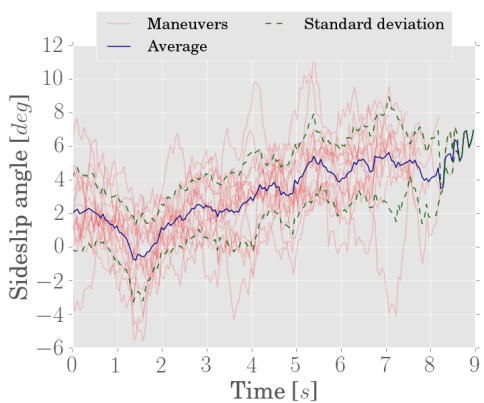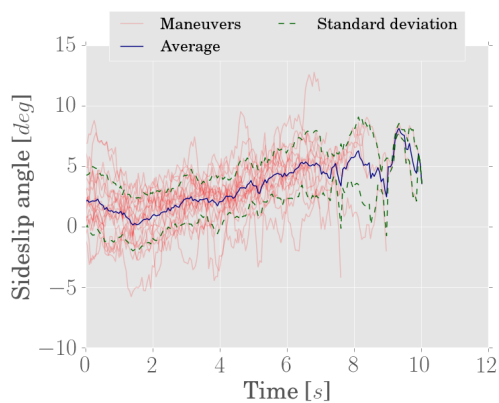
(a) Power setting 2

(b) Power setting 3

Figure B.14: Sideslip values for right turns measured by the β_s windvane and corrected for the yaw induced velocities. These values are found using the steering input of 8 ^{o}.

(a) Power setting 0   (b) Power setting 1
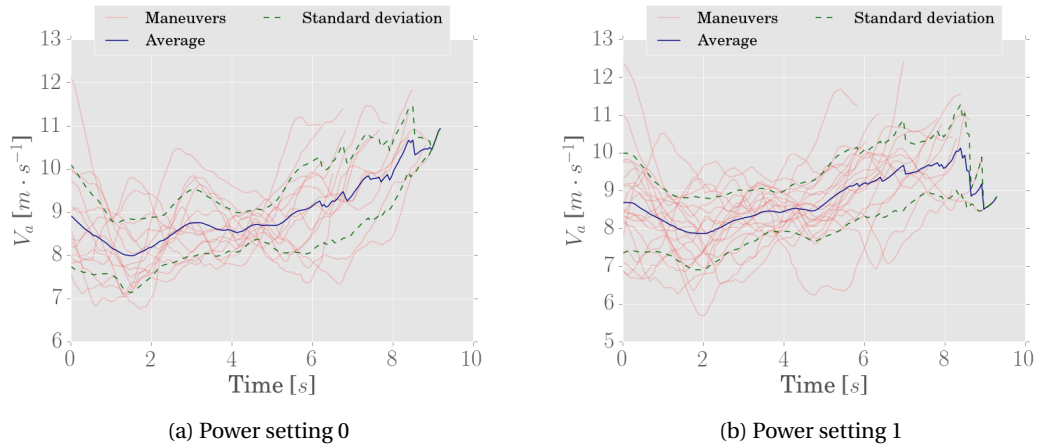
Figure B.15: The velocity v_a measured by the pitot tube on the front of the measuring boom. These values are found using the steering input of 8 ^{o}.

(a) Power setting 2   (b) Power setting 3
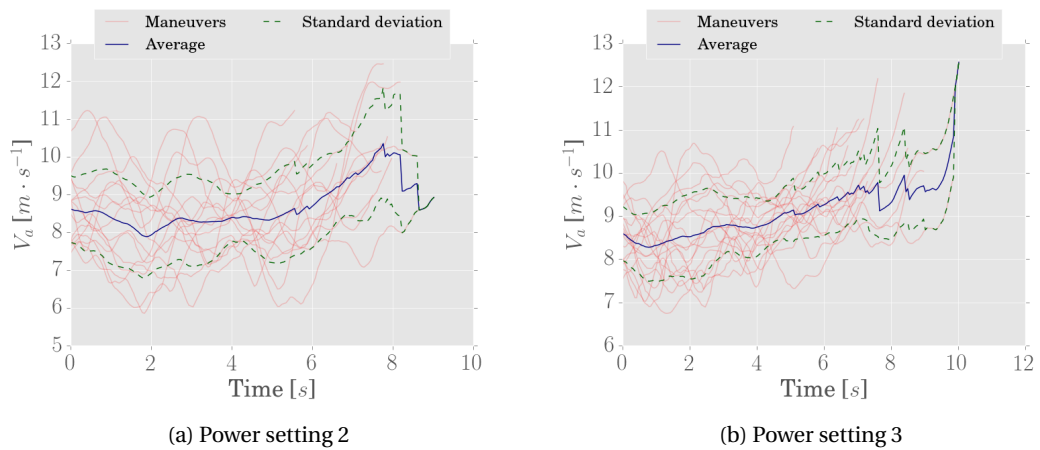
Figure B.16: The velocity v_a measured by the pitot tube on the front of the measuring boom. These values are found using the steering input of 8 ^{o}.

(a) Power setting 0   (b) Power setting 1
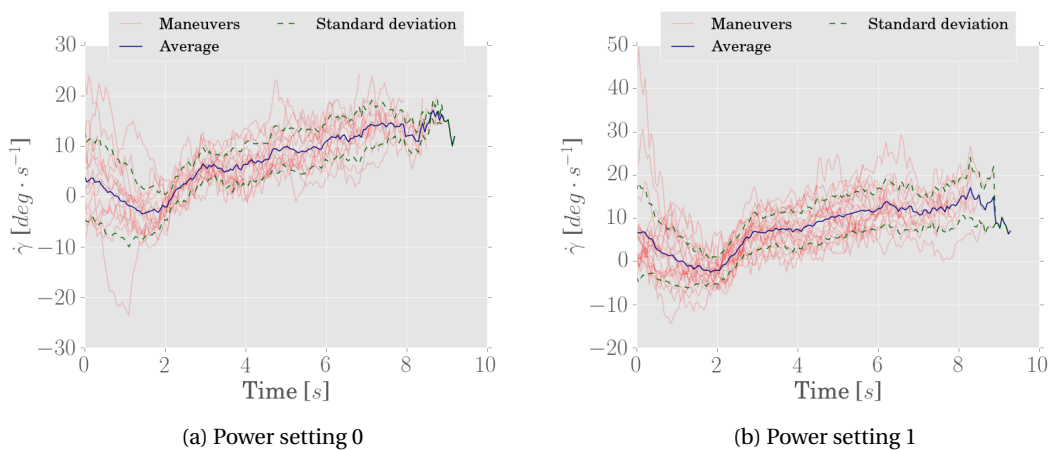
Figure B.17: The yaw rate $\dot{\gamma}$ measured by the pitot tube on the front of the measuring boom. These values are found using the steering input of 8 ^{o}.

(a) Power setting 2
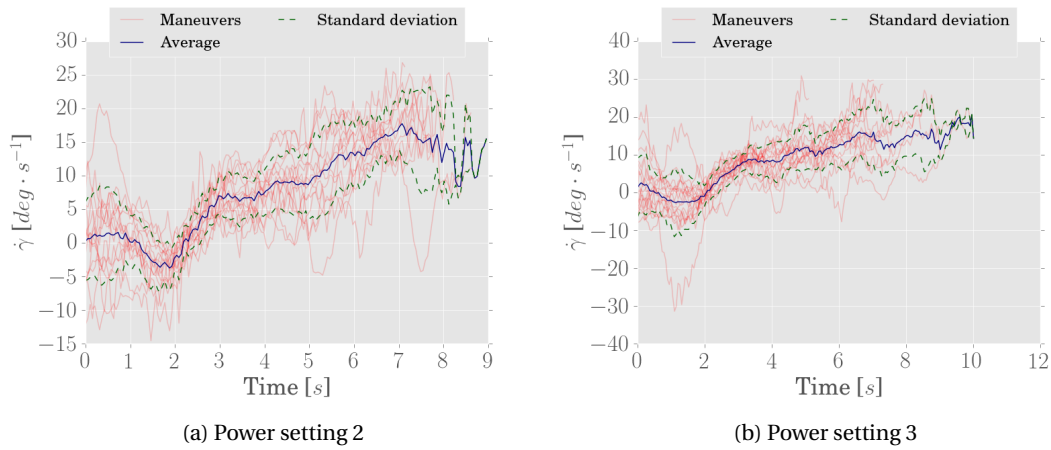
(b) Power setting 3

Figure B.18: The yaw rate $\dot{\gamma}$ measured by the pitot tube on the front of the measuring boom. These values are found using the steering input of 8 ^{o}.
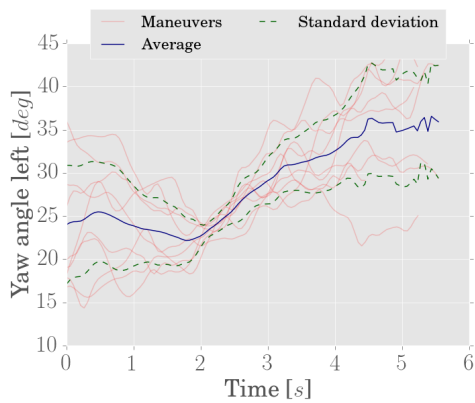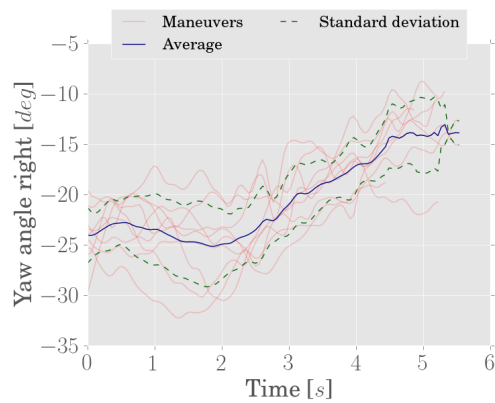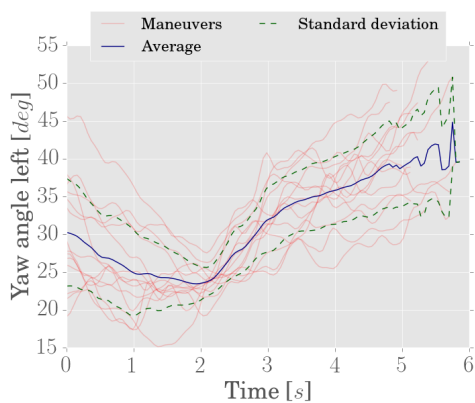

(a) Left (pilot point of view) side of the kite.

(b) Right (pilot point of view) side of the kite.
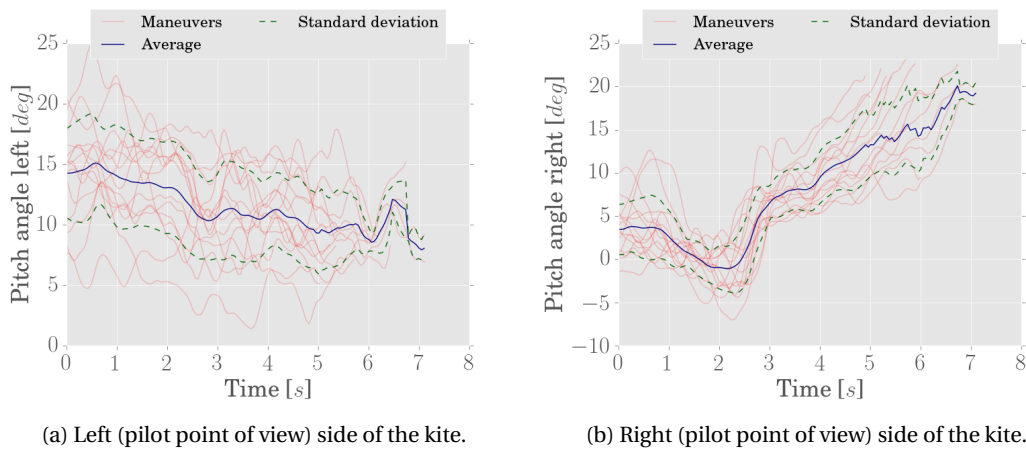
Figure B.19: Pitch values during right turns that were performed with the 0th power setting. The pitch angle at the middle is subtracted from these values to show how the edges deform with respect to the overall kite.

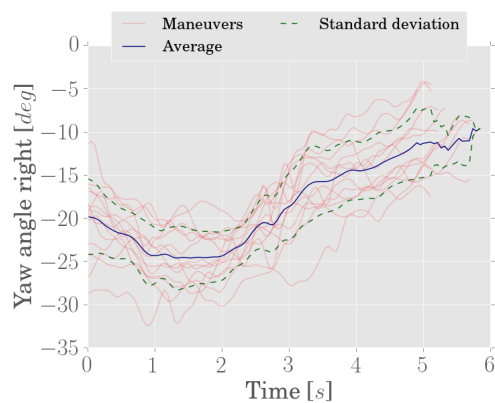(a) Left (pilot point of view) side of the kite.

(b) Right (pilot point of view) side of the kite.

Figure B.20: Pitch values during right turns that were performed with the 1st power setting. The pitch angle at the middle is subtracted from these values to show how the edges deform with respect to the overall kite.
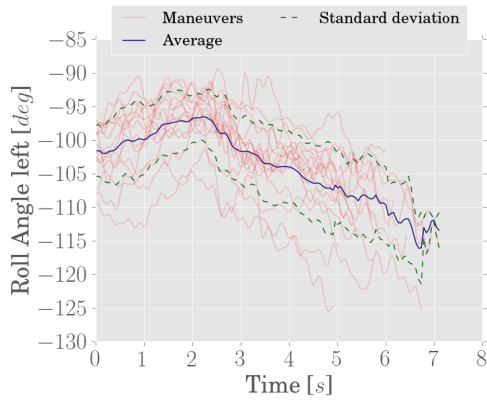
(a) Left (pilot point of view) side of the kite.

(b) Right (pilot point of view) side of the kite.

Figure B.21: Pitch values during right turns that were performed with the 2nd power setting. The pitch angle at the middle is subtracted from these values to show how the edges deform with respect to the overall kite.
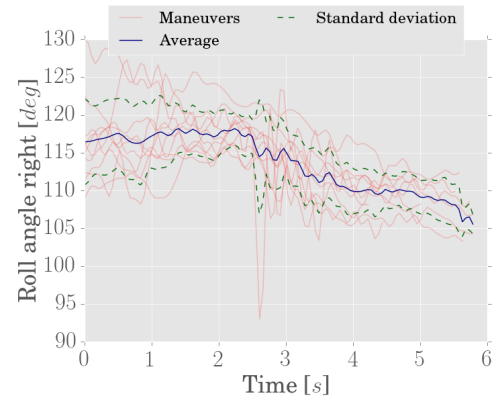

(a) Left (pilot point of view) side of the kite.

(b) Right (pilot point of view) side of the kite.

Figure B.22: Pitch values during left turns that were performed with the 3rd power setting. The pitch angle at the middle is subtracted from these values to show how the edges deform with respect to the overall kite.
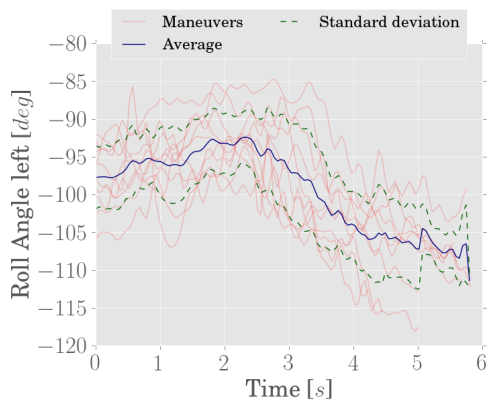

(a) Left (pilot point of view) side of the kite.

(b) Right (pilot point of view) side of the kite.

Figure B.23: Yaw values during right turns that were performed with the 0th power setting. The yaw angle at the middle is subtracted from these values to show how the edges deform with respect to the overall kite.
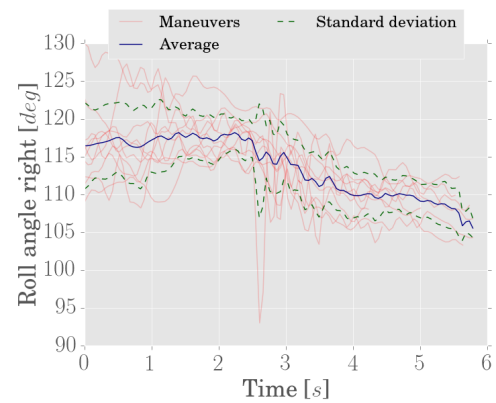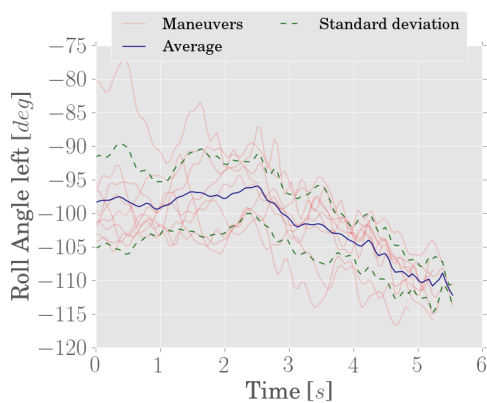
(a) Left (pilot point of view) side of the kite.　　　　(b) Right (pilot point of view) side of the kite.

Figure B.24: Yaw values during right turns that were performed with the 1st power setting. The yaw angle at the middle is subtracted from these values to show how the edges deform with respect to the overall kite.

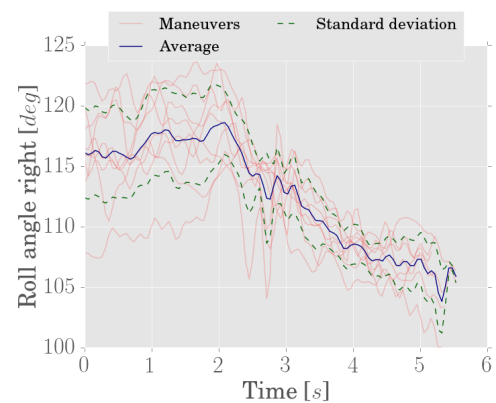(a) Left (pilot point of view) side of the kite.　　　　(b) Right (pilot point of view) side of the kite.

Figure B.25: Yaw values during right turns that were performed with the 2nd power setting. The yaw angle at the middle is subtracted from these values to show how the edges deform with respect to the overall kite.

(a) Left (pilot point of view) side of the kite.]　　　　(b) Right (pilot point of view) side of the kite.

Figure B.26: Yaw values during left turns that were performed with the 3rd power setting. The yaw angle at the middle is subtracted from these values to show how the edges deform with respect to the overall kite.
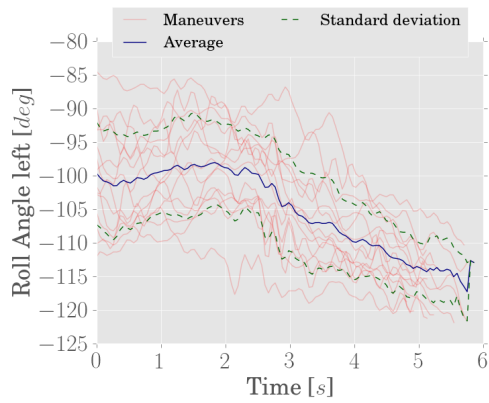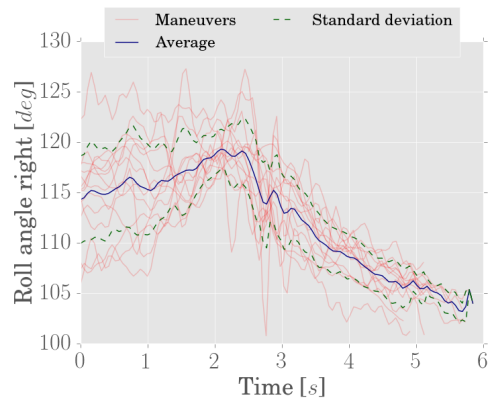
(a) Left (pilot point of view) side of the kite.

(b) Right (pilot point of view) side of the kite.

Figure B.27: Roll values during right turns that were performed with the 0th power setting. The roll angle at the middle is subtracted from these values to show how the edges deform with respect to the overall kite.


(a) Left (pilot point of view) side of the kite.

(b) Right (pilot point of view) side of the kite.

Figure B.28: Roll values during right turns that were performed with the 1st power setting. The roll angle at the middle is subtracted from these values to show how the edges deform with respect to the overall kite.

(a) Left (pilot point of view) side of the kite.

(b) Right (pilot point of view) side of the kite.

Figure B.29: Roll values during right turns that were performed with the 2nd power setting. The roll angle at the middle is subtracted from these values to show how the edges deform with respect to the overall kite.
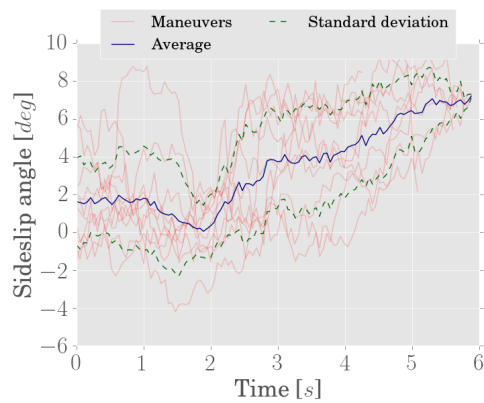
(a) Left (pilot point of view) side of the kite.

(b) Right (pilot point of view) side of the kite.

Figure B.30: Roll values during left turns that were performed with the 3rd power setting. The roll angle at the middle is subtracted from these values to show how the edges deform with respect to the overall kite.
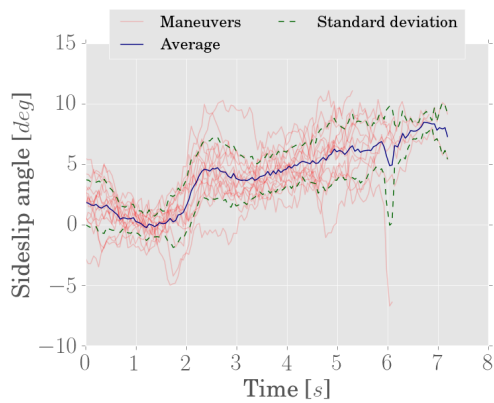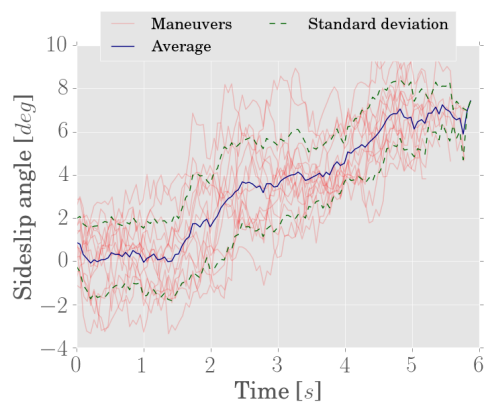

(a) Power setting 0

(b) Power setting 1

Figure B.31: Sideslip values for right turns measured by the β_s windvane and corrected for the yaw induced velocities. These values are found using the steering input of 20 ^{o}.
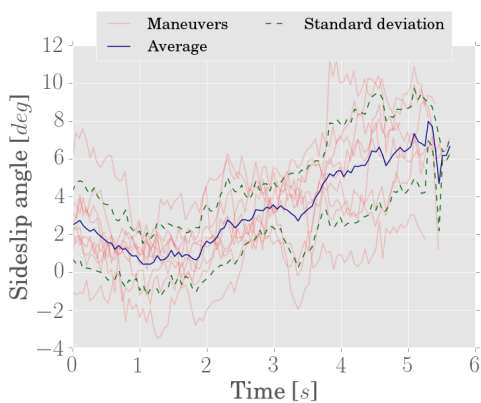
(a) Power setting 2

(b) Power setting 3

Figure B.32: Sideslip values for right turns measured by the β_s windvane and corrected for the yaw induced velocities. These values are found using the steering input of 20 ^{o}.
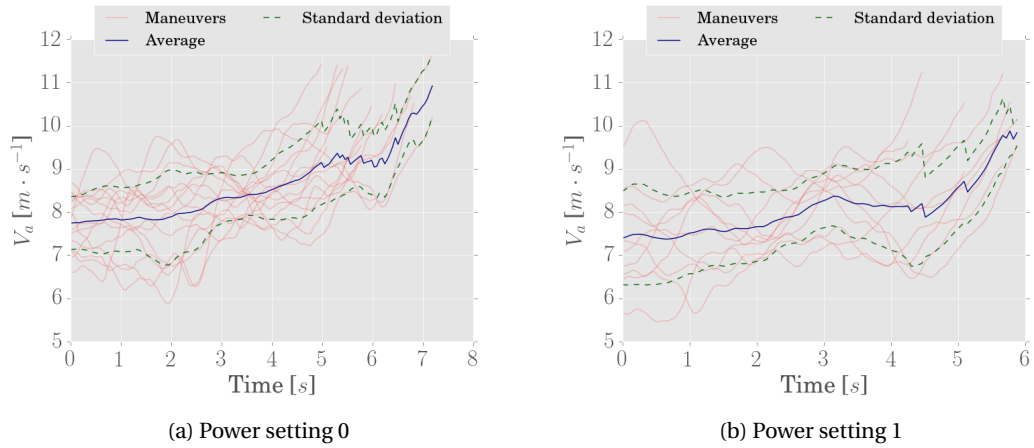
(a) Power setting 0

(b) Power setting 1

Figure B.33: The velocity v_a measured by the pitot tube on the front of the measuring boom. These values are found using the steering input of 20 ^{o}.
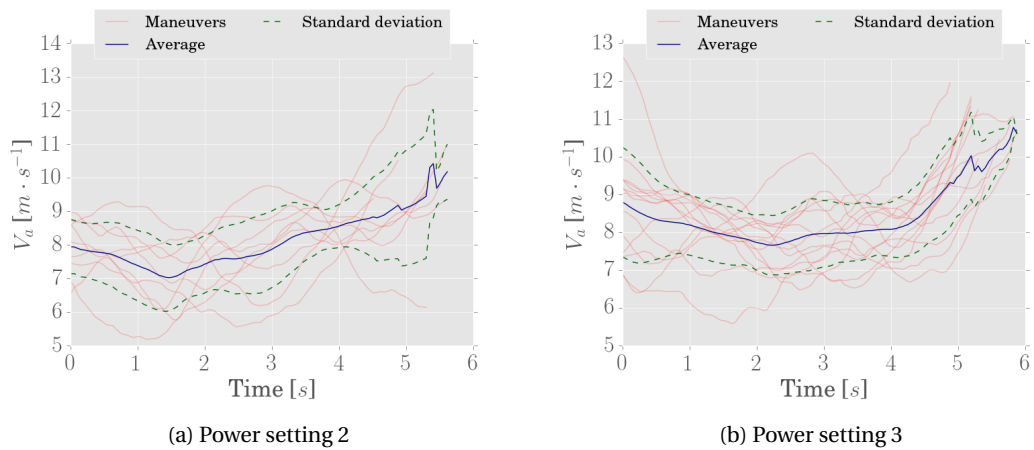

(a) Power setting 2

(b) Power setting 3

Figure B.34: The velocity v_a measured by the pitot tube on the front of the measuring boom. These values are found using the steering input of 20 ^{o}.

(a) Power setting 0
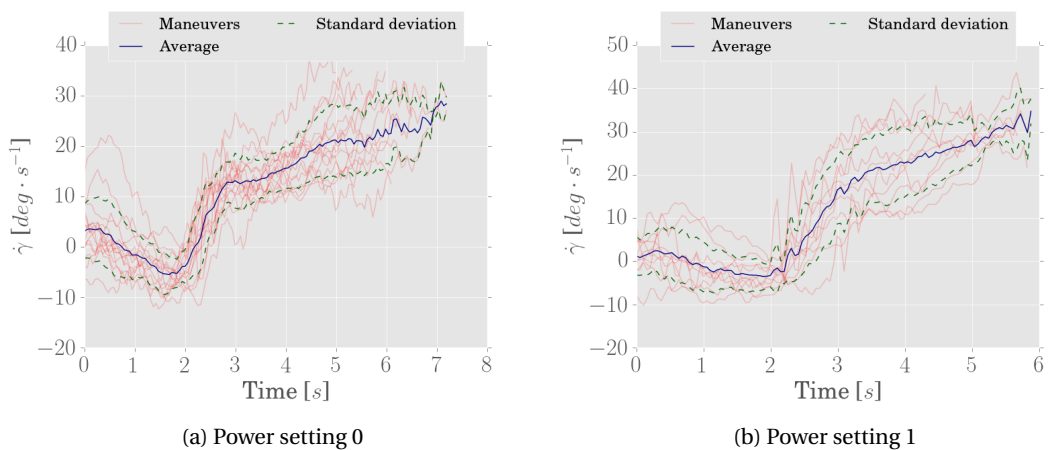
(b) Power setting 1

Figure B.35: The yaw rate $\dot{\gamma}$ measured by the pitot tube on the front of the measuring boom. These values are found using the steering input of 20 ^{o}.

(a) Power setting 2   (b) Power setting 3
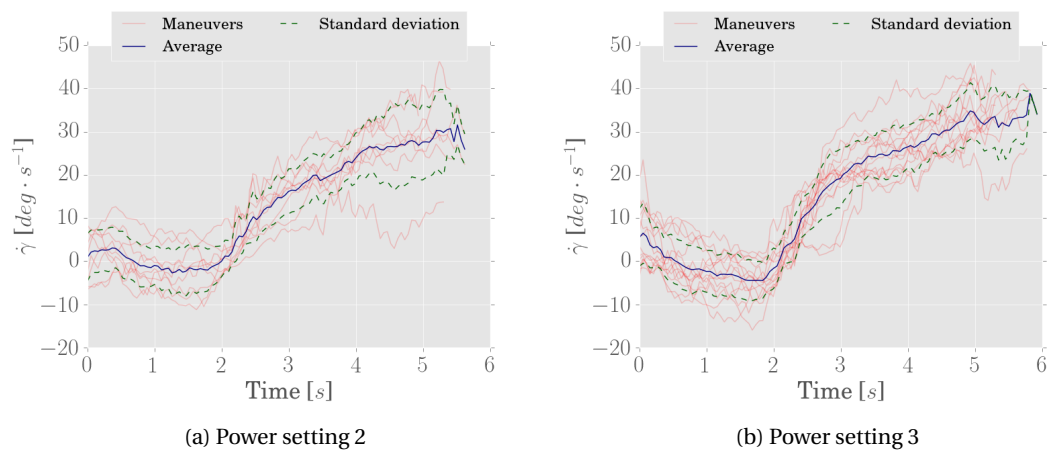
Figure B.36: The yaw rate $\dot{\gamma}$ measured by the pitot tube on the front of the measuring boom. These values are found using the steering input of 20 ^{o}.